First Principles Studies of Water and Ice on Oxide Surfaces

Xiaoliang Hu

Department of Chemistry

University College London

Thesis submitted for the degree of Doctor of Philosophy

January 2010

I, Xiaoliang Hu, confirm that the work presented in this thesis is my own. Where information has been derived from other sources, I confirm that this has been indicated in the thesis.

Abstract

The interaction of water (and ice) with oxide surfaces has been studied with first principles density functional theory. To begin, an extensive series of studies on the clay mineral kaolinite ($Al_2Si_2O_5(OH)_4$) are reported with a view to understanding the efficacy of kaolinite as a heterogeneous ice nucleating agent. The main conclusions are: (i) water clustering is disfavoured on the kaolinite surface; (ii) a stable two dimensional ice-like water overlayer can form; (iii) water covered kaolinite is itself "hydrophobic" compared to the bare "hydrophilic" kaolinite surface; and (iv) it is shown that amphoterism (the ability to accept and donate H bonds) of the hydroxylated kaolinite surface is key to its many properties with regard to water adsorption and ice nucleation. Following the water adsorption study, the perfect basal surface of kaolinite was investigated and it (and in general the entire class of so-called 1:1 clay surfaces) is shown to be polar. Extending the water adsorption studies beyond kaolinite the interaction of water with a range of rocksalt (alkaline earth metal) oxide surfaces was examined with a view to better understanding the fundamental properties of water adsorption, dissociation, and proton transfer on oxide surfaces. These studies reveal that the water adsorption energy and the tendency to dissociate both increase as one moves down the alkaline earth series of oxides. Finally, it is observed that water on MgO(001) undergoes rapid proton transfer within clusters of just two water molecules, made possible by facile dissociation and recombination of the water molecules within the dimers. Overall, it is hoped that these studies shed new light on several fundamental aspects of the interaction of water with oxide surfaces at the molecular level.

Contents

List of Figures

List of Tables

Chapter 1

Introduction

Theoretical chemistry and physics based on quantum mechanical electronic structure theories have become an important and powerful complement to experiment in the atomic scale study of materials. Such simulations have extended and broadened our understanding in a wide variety of areas and are considered by many as virtual experiments. These computational experiments have been incredibly useful, for example, helping to understand important aspects of high pressure and high temperature physics of the earth's core where conditions are so extreme that they can not readily be explored in experiments (e.g. [1]). Or, in surface science, the chemical reactivity of catalyst surfaces has been unravelled (e.g. [2, 3]). There are many other examples in other fields too.

In the electronic structure theories which underpin theoretical chemistry and physics, the central task is to solve the Schrödinger or Schrödinger-like equation. There are many approaches to do this. Density functional theory (DFT) [4, 5] can often be a good option, because it has proven capable of computing a host of properties of condensed matter, their surfaces, and the interactions between surfaces and adsorbates to a reasonable accuracy with an acceptable computational cost. DFT combined with other practical computational techniques is the main approach used in this thesis to investigate water-oxide interfaces.

Water is one of the most common and important substances on earth. The many fascinating molecular properties of water and its almost ubiquitous appearance on solid surfaces, in particular oxide surfaces, makes it a topic of central importance to a surprisingly wide variety of scientific disciplines, including atmospheric chemistry, heterogeneous catalysis and photocatalysis, chemical sensing, corrosion science, environmental chemistry and geochemistry, soil science, semiconductor manufacturing and cleaning, and biology, to name but a few [6, 7]. In this thesis, several key aspects of water at oxide surfaces will be examined with the aid of DFT simulations. Specifically, this involves a treatment of water adsorption and ice nucleation on a layered oxide surface, the examination of proton transfer dynamics in adsorbed water clusters, and a systematic study aimed at understanding adsorption trends and the fundamental factors that decide the adsorption structure and state (intact or dissociated) of water on a range of simple rocksalt oxide surfaces.

The interest in water adsorption on layered oxide surfaces, specifically layered aluminosilicate clays[1], stems from the fact that the adsorption of water on clay mineral surfaces is often the first step in heterogeneous ice nucleation[2], and subsequently cloud formation and precipitation [8]. This happens in the atmosphere on clay aerosol particles, with the aerosol particles being the ice forming nuclei. Chemical analysis of particles found at the center of snow crystals reveals that clay minerals as well as microorganisms, combustion products, and some other natural and anthropogenic products commonly act as sources of ice forming nuclei. Clay mineral dust particles, as typical ice forming nuclei, normally enter the upper atmosphere through dust storms and occur in great abundance in the atmosphere as small nano- to micro-meter sized particles. Of the many varieties of microscopic clay mineral dust particle effective in encouraging

[1]Clay minerals are layered silicate minerals that occur in soils, sediments, sedimentary rocks, and weathered or altered rocks. The commonly used classification to describe structures divides clay minerals into 1:1 structures constructed of repeating tetrahedral-octahedral layers with interlayer spacing of $\sim$7 Å, and 2:1 structures constructed of repeating tetrahedral-octahedral-tetrahedral layers with interlayer spacing of either $\sim$10 or $\sim$14 Å.

[2]Heterogeneous nucleation is the process of nucleation at an interface, typically at a solid surface of a foreign substance. Homogeneous nucleation, on the other hand, occurs when only water is present.

the freezing of water, kaolinite ($Al_2Si_2O_5(OH)_4$) plays a prominent role being a common ice nucleating agent identified by chemical analysis in field studies of naturally formed snow crystals [8]. In addition, in laboratory experiments, kaolinite exhibits good nucleation ability, having a threshold temperature[3] for ice nucleation in the deposition mode[4] of around -9 to -11 °C [8]. This is warmer than the typical threshold temperature range between -10 and -20 °C for silicate soil particles. A very simple text book explanation was suggested to explain the efficacy of kaolinite as an ice nucleating agent by simply noting that the pseudohexagonal arrangement of the hydroxyl groups at the surface of kaolinite is close to the hexagonal arrangement at the basal plane of ice [8]. One of the main aims of this thesis is to test this assumption and understand how exactly water adsorbs and ice nucleates on kaolinite.

In the last decade, great progress has been made to understand water adsorption and ice nucleation on model substrates, in particular on close packed transition metal surfaces (e.g. Ni, Cu, Rh, Ru, Pd, Pt, and Ag). Mainly this is thanks to the application of ultra high vacuum (UHV) surface science techniques such as scanning tunneling microscopy (STM), and also DFT [6, 7, 9–11]. This work has lead to the characterisation of various interface water system, including small clusters, two dimensional (2D) overlayers, and even a one dimensional ice structure built from pentagons [12]. The kaolinite surface structure is more complex than those of metal surfaces, and surface-science style UHV studies of water on kaolinite have not yet been performed. However, DFT can still be used in the hope of predicting relevant structures that may form and providing molecular level insight and understanding. Specifically, the molecular level DFT study of water-kaolinite here will mainly consider the structural and energetic characterization of interfacial water and ice. It includes the investigation of structures and stabilities of water monomers and clusters adsorbed on the cleavage surface of

[3]The threshold temperature is conventionally taken as the temperature at which 1 particle in 10^4 produces an ice crystal.

[4]In the deposition mode, water at temperatures below 0°C is adsorbed directly from the vapor phase onto the surface of the ice forming nuclei, and at sufficiently low temperatures, water is transformed into ice on the surface.

kaolinite, the subsequent ice-like monolayer and multilayer structures, and their stabilities are compared with those on other surfaces. Other aspects related to the ice nucleation are discussed as well and they are the lattice match role between kaolinite surfaces and ice basal planes, the amphoteric role of surface hydroxyl groups, and the surface structure of the kaolinite basal plane.

Questions about how stable water is and which state (intact or dissociated) water is in on different surfaces are simple, but fundamental and important to understand the water-oxide interaction and many other related chemical processes at interfaces. Water adsorption and dissociation can affect the surface properties of materials, for example, surface hydroxylation can render a surface with different reactivity to that of a surface covered in molecular water, leading to significant implications to other surface chemical or catalytic processes. Many experimental and theoretical studies have focused on water adsorption and dissociation on various oxide surfaces (See reviews in [6, 7]). For example, experimental and theoretical evidence indicates water is dissociated on the Al-terminated clean surface of α-Al_2O_3 [13, 14]. However, different conclusions from experimental and theoretical studies can often be arrived at. TiO_2 and MgO are famous examples, in which the computational set-up or the presence of defects at the surface can lead to the question of water dissociation being controversially discussed [6, 7]. Overall this indicates that many factors can affect the tendency of water to dissociate. They may include the chemical nature of the substrate, the surface structure, surface defects, the nature and strength of water-surface interaction, and the corresponding water-water interaction. Information on the geometric and electronic structures of water at oxide surfaces can be obtained from DFT calculations, so in this thesis, special attention will focus on trying to understand the nature and strength of interactions at water-oxide interfaces. Specifically, a series of simple model oxide surfaces (the rocksalt alkaline earth metal oxide (001) surfaces) will be chosen and water monomer adsorption calculations on them will be performed and compared. Trends in water adsorption and dissociation are sought so as to better understand the fundamental nature of water-oxide interfaces.

Related to the question of water adsorption and dissociation on surfaces, the dynamical properties of these systems are also of interest. In particular, proton transfer processes are fundamental processes in chemistry, biology, and physics, and important at surfaces with connection to e.g. electrochemistry [15]. In liquid water, proton transfer or diffusion is realized by the Grotthuss mechanism and some basic descriptions about this process have been proposed [16, 17]. In contrast, understanding of proton transfer processes at water-oxide interfaces lags far behind. Here, proton transfer between water and a substrate and between water is studied within the smallest water cluster, a water dimer, on the simple rocksalt MgO(001) surface.

The rest of this thesis will be presented as follows: In the next two chapters I briefly introduce water-oxide interactions and the theoretical methods that have been used. Following this, I present results mainly from water adsorption studies on a variety of solid surfaces. In Chapter 4, this involves water adsorption and ice nucleation on the aluminosilicate clay kaolinite. In Chapter 5, I focus on the bare kaolinite surface, revealing that its structure is likely to be more complex than previously anticipated. In Chapter 6, a systematic trend study of water on a variety of simple oxide surfaces is presented. In Chapter 7, water dimers on MgO are examined and shown to exhibit interesting proton transfer dynamics. Finally, in Chapter 8, I summarise the results and briefly discuss some perspectives for future research.

Chapter 2

A brief introduction to water-oxide interactions

For the past few decades interest in water-solid interfaces and chemical reactions at aqueous-solid interfaces, in particular mineral surfaces and oxide surfaces, has increased significantly. This is mainly due to the central importance of such interfaces to a variety of scientific fields, including atmospheric chemistry, heterogeneous catalysis and photocatalysis, chemical sensing, corrosion science, environmental chemistry and geochemistry, metallurgy and ore beneficiation, metal oxide crystal growth, soil science, earth science, semiconductor manufacturing and cleaning, and tribology, to name but a few [6, 7, 18–22]. Because water-solid (oxide) interfaces and chemical interactions at aqueous-solid (oxide) interfaces are often extremely complicated, a full understanding on the molecular and atomic level has not been achieved yet. In practice, many different experimental and computational techniques have been used to study the key features of such interfaces under both UHV and ambient conditions (around 298 K and 1 atm). The thickness of the water layer on solid (oxide) surfaces can range from a macroscopic liquid water layer ($>$1 mm thick) to a thin water film (a few nm thick), to less than a single monolayer of molecules depending on the substrate and the relative humidity. Across these different water coverage regimes, much of the physics and chemistry of these interfaces has begun to be understood. This involves, for example, the structure, bonding, composition of water-solid (oxide) interfaces and the effect of

chemical reactions on the electronic and geometric structure of the solid (oxide) surface.

Modern experimental surface science methods under UHV conditions (combined with quantum mechanical computational techniques, e.g. DFT) are one of the main branches to understand water-solid (oxide) interfaces. These surface-sensitive experimental techniques exploit electron, ion, atom, and X-ray spectroscopies and scattering information obtained in high vacuum. Although most of them were developed originally for metals and semiconductors, they have also recently been applied successfully to oxides and other ionic compounds [18, 22, 23]. These experimental techniques include, for example, low-energy electron diffraction (LEED), ion-scattering spectroscopy (ISS), photoelectron (UPS, XPS, etc.) and inverse photoelectron (IPS) spectroscopies, electron energy loss (ELS and HREELS), Auger spectroscopies, temperature programmed desorption (TPD) and reaction (TPR) spectroscopies, and the scanning probe microscopies (STM, AFM, etc.). Studying the interaction of water with well prepared solid (oxide) surfaces, these experimental techniques are extremely powerful. Detailed information about water-solid interfaces on the molecular and atomic level has been obtained on a large number of solid (oxide) surfaces, for example, water vapour adsorption on α-Al_2O_3, MgO, ZnO, TiO_2, α-Fe_2O_3, CeO_2, CuO, α-Cr_2O_3, etc. [7, 18].

As with all scientific methods and techniques, modern surface science methods under UHV conditions (combined with computational techniques) can not cover all surface and interface questions. They are applied mainly to the low coverage (water cluster or monolayer) regime and to well prepared single crystal substrates. However, polycrystalline or particulate samples or the interfaces between macroscopic water layers and solid (oxide) surfaces are often encountered in more practical situations. Similarly, the pressure difference between vacuum measurements and real ambient atmospheric pressure is another issue to be noted. Despite these limitations, a great deal of important information has been, and will continue to be, obtained by modern surface science techniques under vacuum condition (combined with computational techniques).

Beyond the study of water clusters or water monolayers on well prepared solid (oxide) surfaces under UHV conditions, there have also been many studies focusing on water thin films under ambient conditions [21, 22]. Thin film water coats insulators, metals, semiconductors, and even ice under ambient conditions and it has important effects on the physical and chemical properties of the substrates it covers. Normally ambient thin film water involves two interfaces: the one with the underlying solid surface and the one with air. The thickness of the water film is determined by the nature of the substrate, the air relative humidity, and the temperature. Many interesting fundamental questions are related to the the nature of the ambient thin water film, for example, water wetting, ice nucleation, and the growth of multilayer films on solid (oxide) surfaces. Although some experimental techniques that depend on the low background pressure of the UHV conditions can not be used directly for ambient water thin film studies, there are some other approaches that have been applied to such systems: intermolecular force measurements, optical interrogations, both linear (ellipsometry and infrared spectroscopy) and nolinear (second harmonic and sum frequency generation), and molecular simulations. With these techniques, water films on MgO(001), α-Al_2O_3(0001), and muscovite mica(001) along with many other non-oxide surfaces, have all been studied [21].

Another main branch of water-solid (oxide) interfaces is the study of macroscopic liquid overlayers. The underlying solid (oxide) and liquid water far from the interfaces retain the structures they adopt in bulk. The key unknown issues still related to the immediate interface region. In contrast to the water clusters and water thin films on solid (oxide) surfaces, the nature of aqueous-solid (oxide) interfaces is perturbed not only by interfacial interactions but by bulk water and ions on solution. The molecular structure of aqueous-solid interfaces is very likely to be different from that under UHV conditions or in the thin water film systems. The hydroxylation of metal oxides is a good example. Many metal oxides exposed to liquid water at room temperature are converted to fully hydroxylated bulk materials, e.g., MgO tends to be converted to

the hydroxylated mineral brucite, $Mg(OH)_2$. In contrast, many experimental studies performed under UHV with low water coverages show little or no indication of surface hydroxylation [18, 23].

In practice, many experimental techniques have been developed to determine the properties of solid (oxide) surfaces in contact with aqueous solution. For example, the application of scanning probe microscopies (STM and AFM) and high-resolution surface X-ray scattering techniques under ambient conditions has provided substantial new insights into aqueous-solid (oxide) interfaces along with the conventional techniques (NMR and EPR). A few aqueous-solid (oxide) interfaces and chemical reactions at these interfaces, including MgO, SiO_2, RuO_2, TiO_2, $CaCO_3$ and muscovite mica, have been studied [18, 20]. Based on a considerable amount of experimental data, a family of thermodynamic and electrostatic models of the electrical double layer models[1] have been proposed to explain and describe the aqueous-solid interfacial properties at a qualitative level.

As mentioned above, there are many different experimental techniques to deal with the different experimental conditions encountered at water-solid (oxide) interfaces. Meanwhile, theoretical approaches (or computational techniques)[2] are important and widely used complements to experiment. They are powerful and useful particularly to understand water structures on the underlying substrates, the bonding nature of water adsorption (or dissociation), solid (oxide) surface reactivity, etc. Theoretical studies involve different scales of methods, from quantum mechanics to classical mechanics. A large number of successful studies of water-solid (oxide) interactions can be found in the

[1]The electrical double layer describes the structure that appears on the surface of a charged object when it is placed into a liquid. Specifically, it describes the surface charge of the solid, the decay of the electrical potential away from the surface, and the concentration and distribution of cations and anions in both the compact and diffuse layers needed to neutralize the surface charge as a function of pH and ion concentration.

[2]In this thesis, all water-oxide studies were performed with computational techniques, specifically DFT. The theoretical background of these computational techniques will be introduced in the next chapter.

literature, with theoretical methods (*ab initio* electronic structure methods, molecular dynamics and Monte Carlo simulations, empirical potentials, etc.) or the combinations of theoretical and experimental techniques [7, 22, 24–33].

The application of experimental and theoretical methods to aqueous water-solid (oxide) interfaces has been proven to be effective in many circumstances. However, there are still lots of challenges to be overcome. They include, for example, the connection between the electrical double layer models and theoretical simulations, the direct comparison of experimental macroscopic observable properties (X-ray diffraction or photoemission spectroscopies) with theoretical results, and the presence of complicated real macroscopic surfaces in simulations. These challenges are important and exciting, but they are not ones that have been addressed in this thesis, which instead concentrates on obtaining molecular level insight for low coverages of water at a variety of oxide surfaces.

Chapter 3

Theoretical background

First principles total energy calculations are the main tools used in this thesis. In this chapter, some relevant theories for solving many-body electronic structures and the other practicalities involved in performing total energy calculations are described. These include density functional theory, supercells and periodicity, basis sets, pseudopotential theory, and molecular dynamics. These techniques and their combination are now very popular for the treatment of electronic structures of condensed phases, and more detailed accounts can be found in, e.g., refs [34–41].

3.1 Electronic structure theory

3.1.1 Born-Oppenheimer approximation

For many-body systems, any problem or property related to the non-relativistic electronic structures is covered by Schrödinger's equation. The time-independent Schrödinger equation for a many-body system has the following well-known form:

$$H\Psi(r, R) = E\Psi(r, R), \tag{3.1}$$

where H is the Hamiltonian operator, and E is the total energy of the system (or the eigenvalue of the operator). Ψ is the corresponding wave function, which depends on the Cartesian and spin coordinates of the electrons (r) and nuclei (R) in the system.

If one assumes the nuclei and electrons in the system to be point masses and neglect spin-orbit and other relativistic interactions, then the Hamiltonian operator in atomic units[1] for a system including N electrons and M nuclei is

$$\begin{aligned} H &= T_n + V_{nn} + T_e + V_{ne} + V_{ee} \\ &= -\sum_{A=1}^{M} \frac{1}{2m_A} \nabla_A^2 + \sum_{A=1}^{M} \sum_{B>A}^{M} \frac{Z_A Z_B}{R_{AB}} \\ &\quad -\sum_{i=1}^{N} \frac{1}{2} \nabla_i^2 - \sum_{i=1}^{N} \sum_{A=1}^{M} \frac{Z_A}{r_{iA}} + \sum_{i=1}^{N} \sum_{j>i}^{N} \frac{1}{r_{ij}}, \end{aligned} \tag{3.2}$$

where A and B refer to nuclei, i and j refer to electrons, and the operator ∇^2 is the Laplacian operator,

$$\nabla^2 = \frac{\partial^2}{\partial x^2} + \frac{\partial^2}{\partial y^2} + \frac{\partial^2}{\partial z^2}. \tag{3.3}$$

In Eq. (3.2), the first term on the right hand side (T_n) describes the kinetic energy for the M nuclei with individual mass of m_A; the second term (V_{nn}) is the Coulomb potential energy of the internuclear repulsions, R_{AB} being the distance between nuclei A and B with atomic numbers Z_A and Z_B; the third term (T_e) describes the kinetic energy for the N electrons; the fourth term (V_{ne}) is the Coulomb potential energy for attractions between the electrons and the nucleus, r_{iA} being the distance between electron i and nucleus A. The last term (V_{ee}) shows the Coulomb potential energy of the electron-electron repulsions, r_{ij} being the distance between electrons i and j.

Because the nuclei are much heavier than the electrons[2], in or close to equilibrium the electrons move much faster than the nuclei and respond essentially instantaneously to the motion of the nuclei. Thus the nuclei can be treated adiabatically, leading to a separation of electronic and nuclear coordinates in the many-body wave function. This is known as the Born-Oppenheimer approximation [42]. Under this approxima-

[1] Atomic units is a set of units defined as follows: the unit of mass is the electron's mass m_e; the unit of charge is the proton's charge e; the unit of angular momentum is $\hbar$; the atomic unit of length is the $Bohr$ and the unit of energy is the $Hartree$. m_e, e, and $\hbar$ each have a value of 1 in atomic units.

[2] Even in the most unfavorable case of a proton, its mass is still $\sim$1800 times larger than that of an electron.

tion, the many-body problem is reduced to the solution of the dynamics of electrons in some fixed configuration of the nuclei. Specifically, the wave function in Eq. (3.1) is split into two parts:

$$\Psi(r, R) = \Psi_{e,R}(r)\Psi_n(R), \tag{3.4}$$

where $\Psi_{e,R}(r)$ is the wave function of electrons with fixed configuration (R) of the nuclei and $\Psi_n(R)$ is the wave function of the nuclei. Correspondingly, the kinetic energy term of the nuclei (T_n) is neglected and the repulsion energy term between nuclei (V_{nn}) is treated as a constant. Thus, one arrives at the electronic Schrödinger equation,

$$H_{e,R}\Psi_{e,R}(r) = E_{e,R}\Psi_{e,R}(r), \tag{3.5}$$

where $H_{e,R}$ and $E_{e,R}$ are the electronic Hamiltonian and the electronic energy for the fixed configuration of nuclei, respectively. Here

$$H_{e,R} = -\sum_{i=1}^{N}\frac{1}{2}\nabla_i^2 - \sum_{i=1}^{N}\sum_{A=1}^{M}\frac{Z_A}{r_{iA}} + \sum_{i=1}^{N}\sum_{j>i}^{N}\frac{1}{r_{ij}}. \tag{3.6}$$

and the total energy (E_{tot}) of the system with the fixed configuration of nuclei is then

$$E_{tot} = E_{e,R} + \sum_{A=1}^{M}\sum_{B>A}^{M}\frac{Z_A Z_B}{R_{AB}}. \tag{3.7}$$

E_{tot} of a given system at its ground state is a highly sought after quantity. Many, if not most, physical properties of solids can be related to total energies or to differences in total energies.

The Born-Oppenheimer approximation clearly simplifies the Schrödinger equation (3.1). However, it is still impossible to solve exactly for anything but the simplest model systems with one or two electrons, or an infinite "jellium" system. The root of the problem is the quantity V_{ee}, the electron-electron interaction, which contains all the many-body physics of the electronic structure problem and at least $3N$ spatial coordinates are all coupled by the operator V_{ee}. Since most practical systems contain lots ($\gg 10^{23}$) of electrons and the potential due to the nuclei is far from the constant of jellium, it is a major challenge for us. Thus further approximations are required to solve the electronic Schrödinger equation (3.5) accurately and efficiently.

One fundamental approach to solve the electronic Schrödinger equation numerically is the Hartree-Fock (HF) approximation, which transforms the many-body problem into a single particle problem through approximating the electronic wave function $\Psi_{e,R}(r)$ by a Slater-determinant of single particle wave functions. This ensures the antisymmetry of the wave function under exchange of any two electrons, required to fulfill the Pauli principle, and thereby accounts for a quantum mechanical contribution to the potential by increasing the spatial separation between electrons of like spin, termed the exchange potential (V_x). On the other hand, this approximation does not account for the quantum mechanical interaction between electrons of unlike spin or the instantaneous interactions between electrons. It allows two electrons with opposite spin to approach each other closer than in reality. Compared to the full electron-electron interaction potential (V_{ee}), the Hartree-Fock potential thus includes the classical Coulomb potential (V_{ee}^c) and the exchange potential (V_x), but misses a part termed the correlation potential (V_c). Although this term is smaller than the other two terms, it is often significant for obtaining accurate results. In order to improve the original HF approximation, there are thus further advanced approaches to account for the correlation energy, for example, Møller-Plesset perturbation theory and the coupled cluster approaches [41]. These methods can be very accurate, but are computationally very expensive. Alternatively, DFT is a remarkable theory that replaces the complicated N-electron wave function and the associated Schrödinger equation by a formulation based on the simpler electron density (ρ).

3.1.2 Density functional theory

Density functional theory (DFT) is currently the most popular and robust theoretical approach available for solving the electronic structures of practical systems [39, 40], especially for solids and their surfaces. Although far from a panacea for all physical problems in this domain, no other theoretical approach has provided as much basic understanding of the electronic structures of solid surfaces. DFT has also proven capable

of computing a host of properties of condensed matter and their surfaces to reasonable accuracy.

The original DFT of quantum systems is the model of Thomas and Fermi proposed in 1927 [43, 44]. However, modern DFT was established by Hohenberg and Kohn in 1964 [4], providing some hope of a simple method for describing the effects of exchange and correlation in an electron gas. There are two key theorems given and proven in their landmark paper: (i) for any system of interacting particles in an external potential ($V_{ext}(r)$), $V_{ext}(r)$ is determined uniquely, except for a constant, by the ground state particle density $\rho_0(r)$; and (ii) a universal functional $F_{HK}[\rho(r)]$ for the energy $E[\rho(r)]$ in terms of the density $\rho(r)$ can be defined, valid for any $V_{ext}(r)$. For any particular $V_{ext}(r)$, the exact ground state energy $E_0[\rho_0(r)]$ of the system is the global minimum value of this functional, and $\rho(r)$ that minimizes the functional is the exact ground state density $\rho_0(r)$. Accordingly, the total energy of a configuration at an external potential $V_{ext}(r)$ can be written as

$$\begin{aligned} E[\rho(r)] &= T[\rho(r)] + V_{ee}[\rho(r)] + V_{ne}[\rho(r)] \\ &= F_{HK}[\rho(r)] + \int \rho(r) V_{ext}(r) dr \\ &\geqslant E_0[\rho_0(r)], \end{aligned} \tag{3.8}$$

where

$$F_{HK}[\rho(r)] = T[\rho(r)] + V_{ee}[\rho(r)], \tag{3.9}$$

$$V_{ne}[\rho(r)] = \int \rho(r) V_{ext}(r) dr, \tag{3.10}$$

with the constraint of

$$\int \rho(r) dr = N. \tag{3.11}$$

The Hohenberg-Kohn theorems proved that in principle, if one knows the exact $F_{HK}[\rho]$, the exact total energy and the ground state properties can be obtained from the ground state electron density by the variational principle. However, still an efficient scheme to obtain the ground state density and energy was missing. Based on this, Kohn and

Sham in 1965 [5] defined the universal functional $F_{HK}[\rho]$ by using the one electron orbitals and approximating the kinetic energy of the system by the kinetic energy of non-interacting electrons. This leads to the one-electron Schrödinger-like equation, the Kohn-Sham equation, expressed as,

$$(-\frac{1}{2}\nabla^2 + V_{ext}(r) + V_H(r) + V_{xc}(r))\psi_i(r) = \varepsilon_i\psi_i(r), \tag{3.12}$$

where ψ_i is the wave function of electronic state i and ε_i is the Kohn-Sham eigenvalue. The other terms on the left hand side are the kinetic energy of the non-interacting electrons, the external potential, the Hartree potential, and the exchange-correlation potential, respectively. The Hartree potential and the exchange-correlation potential are given formally by

$$V_H(r) = \int \frac{\rho(r')}{|r-r'|}dr', \tag{3.13}$$

$$V_{xc}(r) = \frac{\delta E_{xc}[\rho(r)]}{\delta\rho(r)}, \tag{3.14}$$

and then the electron density of the system constructed from the Kohn-Sham wave function is expressed by

$$\rho(r) = \sum_i^N |\psi_i(r)|^2. \tag{3.15}$$

Correspondingly, the Kohn-Sham total energy for a set of occupied electronic states (N) can be written as,

$$\begin{aligned} E[\rho(r)] &= \sum_i^N -\frac{1}{2}\int \psi_i^*(r)\nabla^2\psi_i(r)dr + \int V_{ext}(r)\rho(r)dr \\ &\quad +\frac{1}{2}\int\int \frac{\rho(r)\rho(r')}{|r-r'|}drdr' + E_{xc}[\rho(r)] \\ &= \sum_i^N \varepsilon_i - \frac{1}{2}\int\int \frac{\rho(r)\rho(r')}{|r-r'|}drdr' \\ &\quad +E_{xc}[\rho(r)] - \int V_{xc}\rho(r)dr. \end{aligned} \tag{3.16}$$

So far, within the Born-Oppenheimer approximation, the theory is exact. If each term in the Kohn-Sham equation and energy functional is known, one would be able to obtain the exact ground state density and total energy. Unfortunately, there is one unknown term, the exchange-correlation energy term ($E_{xc}[\rho(r)]$), which includes

the non-classical aspects (electron exchange and electron correlation) of the electron-electron interaction along with the component of the kinetic energy of the real system different from the fictitious non-interacting system. This term is incredibly difficult to describe. Indeed it is unclear if this functional can be given in a simple closed form at all. And so to get something useful out of DFT in practice one needs to approximate $E_{xc}[\rho(r)]$. The central goal of modern DFT is therefore to find accurate approximations to the exchange-correlation terms. In addition, it can be seen from Eq. (3.16) that the electronic total energy is not simply the sum of the Kohn-Sham eigenvalues. Those equations (3.12-3.16) are nonlinear and must be solved iteratively. The general procedure is to begin with an initial guess of the electron density, construct the potentials in Eq. (3.12), then obtain the Kohn-Sham wave functions, and a new density and a total energy are obtained. This process will be repeated until convergence to some predefined criteria is obtained.

3.1.3 Exchange-correlation functionals

The Hohenberg-Kohn theorems and the Kohn-Sham equations provide some motivation for using approximated methods to describe the universal functional and the exchange-correlation energy as a function of the electron density. The simplest method of describing the exchange-correlation energy of an electronic system is the local density approximation (LDA) introduced by Kohn and Sham [5]. In LDA the exchange-correlation energy of an electronic system is constructed by assuming that the exchange-correlation energy per electron at point r in the real system, $\varepsilon_{xc}(r)$, is equal to the exchange-correlation energy per electron in a uniform electron gas that has the same density as the electron gas at point r. The basic assumption is that the exchange-correlation functional depends only on the local value of the density. Thus,

$$E_{xc}^{LDA}[\rho(r)] = \int \varepsilon_{xc}(r)\rho(r)dr, \tag{3.17}$$

with

$$\varepsilon_{xc}(r) = \varepsilon_{xc}^{unif}[\rho(r)]. \tag{3.18}$$

The corresponding exchange-correlation potential becomes

$$V_{xc}^{LDA}(r) = \frac{\delta E_{xc}^{LDA}[\rho(r)]}{\delta\rho(r)} = \varepsilon_{xc}^{unif}[\rho(r)] + \rho(r)\frac{\partial\varepsilon_{xc}^{unif}[\rho(r)]}{\partial\rho(r)}. \tag{3.19}$$

The function $\varepsilon_{xc}^{unif}(\rho)$ of the exchange-correlation energy per electron in the uniform electron gas can be divided further into exchange and correlation parts. The exchange energy part is known exactly and the correlation energy is obtained by fitting to highly accurate quantum Monte Carlo calculations of the free electron gas [45, 46]. Modern LDA functionals tend to be exceedingly similar, differing only in how their correlation contributions have been fitted to the free electron gas data. The Perdew-Zunger (PZ) [47], Perdew-Wang (PW) [48], and Vosko-Wilk-Nusair (VWN) [49] functionals are all common LDA functionals.

Strictly, LDA is valid only for slowly varying densities. Although LDA has already given surprisingly good results for a wide range of realistic systems, it typically overestimates binding energies and underestimates bond lengths. For systems with less homogeneous electron densities the results using LDA are often disappointing. There is a straightforward correction to the the local density approximation and it can be achieved by including the gradient of the density , $\nabla\rho(r)$, as well as the density itself to the exchange-correlation functionals. Those functionals beyond the local density approximation are the generalized gradient approximation (GGA) functionals with the form of

$$E_{xc}^{GGA}[\rho(r)] = \int \rho(r)\varepsilon_{xc}^{GGA}[\rho(r), \nabla\rho(r)]dr. \tag{3.20}$$

GGAs are "semi-local" functionals and for many properties, for example, geometries and ground state energies of molecules, GGAs can yield better results than the LDA. As in the LDA, the GGA exchange-correlation energy is also divided into two parts: E_x^{GGA} and E_c^{GGA}. There are many different versions of GGAs based on different constructions of exchange-correlation functionals. The most widely used GGA in this thesis, as in many surface physics studies, is the Perdew, Burke, and Ernzerhof (PBE) [50, 51] exchange-correlation functional. Several off-spring of PBE (RPBE [52] and PBE-WC [53]) and its close relative PW91 [54] are also occasionally used here.

It is expected that the exact exchange obtained from HF theory can play a role in "better" exchange-correlation functionals [55, 56]. Thus DFT exchange-correlation functionals are nowadays sometimes mixed with a fraction of HF exchange. This class of functionals are known as "hybrid functionals". Indeed, many hybrid functionals, for example, B3LYP [57, 58] and PBE0 [56, 59], have been shown to offer noticeably improved performance over LDA and GGA functionals for the calculation of gas phase properties of molecules and band gaps in solids. A class of hybrid exchange-correlation functionals with only one mixing parameter fixed at the value of 1/4 (based on perturbation theory rather on modeling the integral in coupling constant) has been suggested [60]:

$$E_{xc}^{hybrid} = E_{xc}^{GGA} + \frac{1}{4}(E_x^{HF} - E_x^{GGA}). \tag{3.21}$$

If PBE is the GGA used in Eq. (3.21) one arrives at the hybrid PBE0 functional. PBE0 calculations are also reported in this thesis.

Actually, there is an essentially endless list of different exchange-correlation functionals available nowadays. It is worth mentioning that functionals which account for van der Waals forces [61] are now available, although they are not used in this thesis. The van der Waals functionals account for non-local correlations and thanks to the development of improved exchange functionals can offer very high precision for dispersion and hydrogen bond systems [62].

3.2 Periodicity

3.2.1 Bloch's theorem

Crystalline solids can be described in real space in terms of the primitive lattice vectors and the position of atoms inside the primitive unit cell. In this case the potential has the translational periodicity of the unit cell,

$$V(r) = V(r + L), \tag{3.22}$$

where L is a translation vector in real space. The foundation for describing the behaviour of electrons in solids is the reciprocal lattice, which is the correpsonding lattice in reciprocal space. The reciprocal primitive lattice vectors, b_j, $j \in \{1,2,3\}$, are related to the real space primitive lattice vectors a_i, $i \in \{1,2,3\}$, by

$$a_i \cdot b_j = 2\pi\delta_{ij}, \tag{3.23}$$

where δ_{ij} denotes the Kronecker δ.

Bloch's theorem [63–65] states that the eigenfunctions ($\psi_{\boldsymbol{k}}(r)$) of the wave equation for a periodic potential ($V(r)$) are the product of a plane wave ($e^{i\boldsymbol{k}\cdot r}$) and a function ($u_{\boldsymbol{k}}(r)$) with the periodicity of the crystal lattice,

$$\psi_{\boldsymbol{k}}(r) = u_{\boldsymbol{k}}(r)e^{i\boldsymbol{k}\cdot r}, \tag{3.24}$$

where

$$u_{\boldsymbol{k}}(r) = u_{\boldsymbol{k}}(r + L). \tag{3.25}$$

In addition the combination of Eqs. (3.24) and (3.25) implies that

$$\psi_{\boldsymbol{k}}(r + L) = \psi_{\boldsymbol{k}}(r)e^{i\boldsymbol{k}\cdot L}. \tag{3.26}$$

The index $\boldsymbol{k}$ appearing in Bloch's theorem is a wave vector in reciprocal space and can always be confined to the first Brillouin zone[3] (BZ) (or to any other convenient primitive cell of the reciprocal lattice).

3.2.2 Brillouin zone sampling

When the periodic boundary conditions are applied to the solid system,

$$\psi_{\boldsymbol{k}}(r) = \psi_{\boldsymbol{k}}(r + L), \tag{3.27}$$

the electronic states ($\psi_{\boldsymbol{k}}(r)$) are allowed only at a set of $\boldsymbol{k}$ values. However, the number of allowed $\boldsymbol{k}$ values is proportional to the volume of the solid. In the limit of a large

[3]The first Brillouin zone comprises all points in reciprocal space that are closer to the origin (denoted as the Γ point) than to any other reciprocal lattice point.

macroscopic crystal which contains (at least) a total number of primitive unit cells on the order of Avogadro's number, the spacing of the $\boldsymbol{k}$ points goes to zero and $\boldsymbol{k}$ can be considered a continuous variable. Of course, for each fixed wave vector $\boldsymbol{k}$, the eigenvalues of the Hamiltonian are discrete values on general grounds in one primitive cell of the reciprocal lattice and this set of discrete eigenvalues can be labeled by an index i. The electronic states and the corresponding eigenvalues are thus identified as $\psi_{i,\boldsymbol{k}}(r)$ and $\varepsilon_{i,\boldsymbol{k}}$, respectively, and this leads to bands of eigenvalues and an energy gap where there can be no eigenstates for any $\boldsymbol{k}$.

So far the infinite number of electrons in the solid are accounted for by an infinite number of $\boldsymbol{k}$ points, and only a finite number of electronic states are occupied at each $\boldsymbol{k}$ point. The occupied states at each $\boldsymbol{k}$ point contribute to physical quantities such as the electronic potential, electron density, and total energy of the solid so that, in principle, an infinite number of calculations are needed to compute them by performing integration in reciprocal space. However, the electronic wave functions at $\boldsymbol{k}$ points that are very close together will be almost identical. Hence it is possible to represent them over a region of $\boldsymbol{k}$ space only by that at a single $\boldsymbol{k}$ point. Consequently, the integral over the Brillouin zone in reciprocal space required to calculate the electronic potential and hence determine the total energy of the solid is then transformed into a sum over only a finite number of $\boldsymbol{k}$ points, called the $\boldsymbol{k}$ point mesh,

$$\int_{BZ} \frac{1}{\Omega_{BZ}} d\boldsymbol{k} \rightarrow \sum_{\boldsymbol{k}} \omega_{\boldsymbol{k}}, \tag{3.28}$$

where $\omega_{\boldsymbol{k}}$ is the weight of each special $\boldsymbol{k}$ point in the chosen mesh of the Brillouin zone. Different methods to choose the $\boldsymbol{k}$ point mesh have been devised for obtaining very accurate approximations to the electronic potential and the total energy. In this thesis, the method proposed by Monkhorst and Pack [66] has been used, in which a uniform mesh of $\boldsymbol{k}$ points is generated along the three lattice vectors in reciprocal space. The magnitude of any error in the total energy or the total energy difference due to inadequacy of the $\boldsymbol{k}$ point sampling can always be reduced to zero by using a denser set of $\boldsymbol{k}$ points. Therefore, it is crucial to test the convergence of the results with respect to the number of $\boldsymbol{k}$ points in general. For insulators and semiconductors, only a very

small number of $\boldsymbol{k}$ points are needed to obtain an accurate electronic potential and total energy. In contrast, metals require a dense $\boldsymbol{k}$ point mesh to define the Fermi surface and the total energy precisely.

3.2.3 Plane wave basis sets

In practice DFT calculations require the use of a set of basis functions with which to expand the Kohn-Sham wave functions $\psi_{i,\boldsymbol{k}}(r)$. This choice of basis set is of critical importance to the accuracy of an electronic structure calculation. Basis sets can be constructed from either atom-centered functions or from non-atom-centered functions or a combination of both. For solid simulations non-atom-centered plane wave basis sets are a straightforward and common choice. All the calculations reported in this thesis used a plane wave basis set and so plane wave basis sets are now briefly discussed.

Due to the periodicity of a crystal, the function $u_{i,\boldsymbol{k}}(r)$ in Bloch's theorem can be expanded using a discrete set of plane waves whose wave vectors are in the reciprocal space of the crystal,

$$u_{i,\boldsymbol{k}}(r) = \sum_{G} c_{i,G} e^{iG\cdot r}. \tag{3.29}$$

The reciprocal lattice vectors G are defined by

$$G \cdot L = 2\pi m, \tag{3.30}$$

where L is a lattice vector of the crystal in the real space as defined before and m is an integer. By combining Eqs. (3.24) and (3.29) the wave functions $\psi_{i,\boldsymbol{k}}(r)$ are rewritten as,

$$\psi_{i,\boldsymbol{k}}(r) = \sum_{G} c_{i,(\boldsymbol{k}+G)} e^{[i(\boldsymbol{k}+G)\cdot r]}. \tag{3.31}$$

If the Kohn-Sham wave functions in terms of sum of plane waves are substituted into the Kohn-Sham equation (3.12), one obtains that

$$\sum_{G'} [\frac{1}{2}|\boldsymbol{k}+G|^2 \delta_{GG'} + V_{ext}(G-G') + V_H(G-G') + V_{xc}(G-G')] c_{i,(\boldsymbol{k}+G')} = \varepsilon_i c_{i,(\boldsymbol{k}+G)}, \tag{3.32}$$

where $\delta_{GG'}$ is the Kronecker δ, indicating the orthogonality of the plane waves basis set. In principle, an infinite number of plane waves is needed to expand the wave function. However, the coefficient $c_{i,k+G}$ for the plane waves with small kinetic energy are more important than those with large kinetic energy. Thus the plane wave basis set can be truncated to include only plane waves that have kinetic energies less than a particular energy cutoff E_{cut},

$$\frac{1}{2}|\boldsymbol{k}+G|^2 \leqslant E_{cut}. \tag{3.33}$$

Employing a finite basis set introduces a new source of inaccuracy, which can be reduced by increasing the number of plane waves or E_{cut}. Therefore, appropriate convergence tests have to be performed in order to find an E_{cut} that is sufficiently converged to compute the property of interest with the required accuracy.

3.2.4 Supercells

The periodic structures of bulk crystalline solids in real space introduces important elements of simplicity. Correspondingly, the electronic structures of infinite bulk solids can be solved in periodic three dimensional (3D) simulation cells when Bloch's theorem is applied. However, Bloch's theorem can not be used with a plane wave basis set directly to a system containing surfaces, specifically in the direction perpendicular to a solid surface, because a continuous or infinite number of plane wave basis set would be required for surface calculations. Fortunately, this problem can be avoided by the supercell approximation where surfaces, although only periodic parallel to the surface, can nonetheless be computed within periodic 3D simulation cells by introducing a vacuum region into the simulation cell, a so called "supercell". In particular the introduction of a vacuum region along just the direction perpendicular to a surface, for example as shown in Fig. 3.1, partitions the simulation cell into regions of slab (or solid) and vacuum. The periodic boundary conditions ensure that the slab extension is infinite in the two dimensions of the surface plane, and also along the direction perpendicular to the surface plane the vacuum stack extends infinitely. Slabs consist of

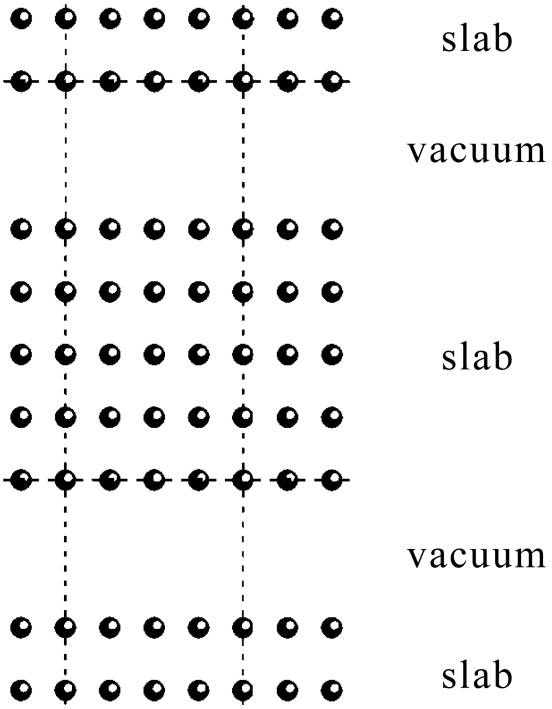

Figure 3.1: Schematic illustration of a supercell (in two dimensions) with solid slab and vacuum

several layers of atoms and the supercell approach leads to two surfaces on both sides of a slab. Thus one has to ensure that the slab is thick enough to avoid interactions between these surfaces. Ideally, the atoms in the middle of the slab should have the physical properties of bulk atoms and the interaction between different slabs should be minimised by a large vacuum region.

3.3 Pseudopotentials

The electrons in a solid (or atom or molecule) can be treated as core electrons and valence electrons. Core electrons are localized and tightly bound to the nuclei, while valence electrons are more extended. Most physical properties of materials depend on the valence electrons and much less so on the core electrons. Since the valence electronic wave functions have to maintain orthogonality with the core electronic wave

functions, the oscillation of the valence electronic wave function is rapid in the core region, the region near nuclei. When a plane wave basis set is chosen to expand the Kohn-Sham wave functions of all the electrons, an extremely large number of plane waves is required to accurately describe the deep potential near the nuclei and the rapid oscillations of the valence electronic wave functions in the core region. In practical calculations the pseudopotential approximation is used to avoid the direct consideration of the less important core electrons in the bonding process and the rapid oscillation of the valence wave functions in the core region. Specifically, in the pseudopotential scheme, core electrons are considered together with nuclei to form a new ionic potential and the strong ionic potential in the core region is replaced by a weaker screened pseudopotential that acts on a set of pseudo wave functions rather than the true valence wave functions. The use of the effective new pseudopotential to describe the electron-ion interaction leads to a reduction of the number of electrons that need to be described. Moreover many fewer plane waves are necessary to describe the much softer and smoother (nodeless) pseudo valence wave functions. Thus faster calculations can be performed or the treatment of bigger systems is possible under the pseudopotential approximation. The true ionic potential, true valence wave function and the corresponding new pseudopotential and pseudo wave function are illustrated schematically in Fig. 3.2. It can be seen from Fig. 3.2 that the pseudopotential is much weaker than the true potential and the pseudo wave function has no radial node inside the core region r_c. One factor in deciding how the core region radius r_c is chosen is that the core regions of neighboring atoms do not overlap and in general the smaller the core radius is, the more accurate and reliable the pseudopotential is expected to be.

The pseudopotential is in general constructed from an all electron DFT calculation for a reference configuration of a free atom or ion. When the all electron potential V_{ae} and the valence states $u_l^{ae}(r)$ for each angular momentum l are obtained, the pseudo wave functions $u_l^{ps}(r)$ are derived in such ways that:
(i) $u_l^{ps}(r)$ and $u_l^{ae}(r)$ correspond to the same eigenvalue,

$$\varepsilon_l^{ps} = \varepsilon_l^{ae}; \tag{3.34}$$

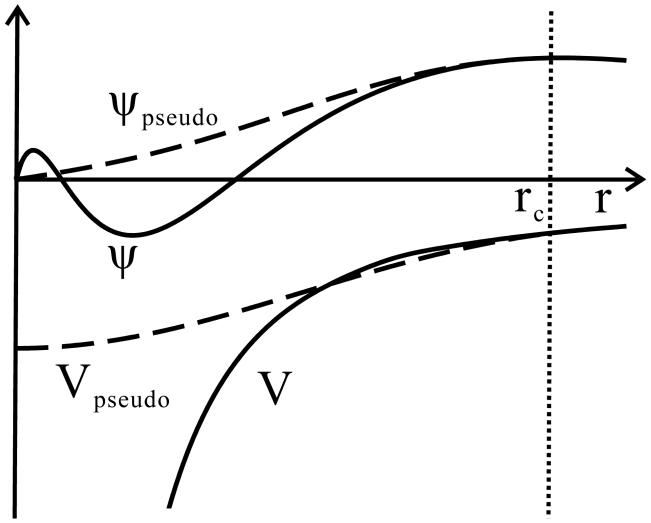

Figure 3.2: Schematic illustration of all electron (solid lines) and pseudoelectron (dashed lines) potentials and their corresponding wave functions. The radius at which the all electron and pseudoelectron values match is designated r_c.

(ii) as shown in Fig. 3.2, $u_l^{ps}(r)$ and $u_l^{ae}(r)$ have the same amplitude beyond a chosen core region radius r_c

$$u_l^{ps}(\varepsilon_l^{ps}, r) \rightarrow u_l^{ae}(\varepsilon_l^{ae}, r), \text{ for } r > r_c, \tag{3.35}$$

and their respective potentials are also identical beyond r_c,

$$V_{ps} \rightarrow V_{ae}, \text{ for } r > r_c; \tag{3.36}$$

(iii) The pseudo wave function is normalized,

$$\int_0^\infty |u_l^{ps}(\varepsilon_l^{ps}, r)|^2 dr = \int_0^\infty |u_l^{ae}(\varepsilon_l^{ae}, r)|^2 dr = 1. \tag{3.37}$$

This implies the norm-conservation constraint,

$$\int_0^{r'} |u_l^{ps}(\varepsilon_l^{ps}, r)|^2 dr = \int_0^{r'} |u_l^{ae}(\varepsilon_l^{ae}, r)|^2 dr = 1, \text{ for } r' \geqslant r_c, \tag{3.38}$$

or in other words, the charge within the core region is the same for the pseudo and the true all electron wave functions.

Satisfied with the above conditions, the general form of a pseudopotential is

$$\begin{aligned} V_{ps} &= \sum_{l=0}^{\infty} \sum_{m=-l}^{l} V_l(r) P_{lm} \\ &= V_{loc} + \sum_{l,m} (V_l - V_{loc}) P_{lm}, \end{aligned} \tag{3.39}$$

where P_{lm} is a projector on angular momentum functions and V_{loc} is the local part of the pseudopotential. A good approximation for V_{loc} can be

$$V_l(r) = V_{loc}(r), \text{ for } l > l_{max}. \tag{3.40}$$

The norm-conservation condition of pseudopotentials requires a relatively large number of plane waves (or large energy cutoff) for "semilocal" oribtals of elements because of their substantial fraction inside the core region and their importance to the bonding. Aimed at performing accurate and reliable calculations with as low a plane wave energy cutoff as possible, a so called "ultrasoft pseudopotential" has been proposed by Vanderbilt [67]. In Vanderbilt's ultrasoft pseudopotential scheme, the norm-conservation condition is relaxed, leading to a new psedo wave function that can be expanded with a much smaller plane wave basis set. The charge deficit due to the relaxation of the norm-conservation conditions are compensated by the introduction of atom-centered augmentation charges to ensure the proper density and potential. These augmentation charges are defined as the charge difference between the all electron and pseudo wave functions, and for convenience they can be treated in a regular grid (not necessarily the same as that used for pseudo wave functions).

Another closely related approach to Vanderbilt's pseudopotential scheme is the projector augmented wave (PAW) method introduced by Blöchl [68, 69]. In the PAW method, a linear transformation is defined to connect the all electron wave functions and pseudo wave functions and the total energy is derived in a consistent way by applying this transformation to the Kohn-Sham equations. In contrast to the pseudopotential method, the PAW method retains the all electron wave functions and potentials, avoids the introduction of a pseudopotential, and retains all the information on the core states.

In practical calculations, it is implemented by the use of an extra radial support grid to construct the partial core correction along with the regular grids used in the ultrasoft pseudopotential scheme. Ultrasoft pseudopotentials and PAW potentials are all used in this thesis.

3.4 Molecular dynamics

Molecular dynamics (MD) is a powerful technique to investigate equilibrium, transport, diffusion, and many other properties of many-particle systems. It uses the classical equations of motion (Newton's equation) to describe the movement of a set of particles (nuclei) in the system. When such information is generated at the microscopic level (positions, momenta etc.), the macroscopic terms (pressure, temperatures etc.) can be obtained from them. In this thesis, first principles (or *ab initio*) MD calculations, in particular so-called Born-Oppenheimer MD[4], are reported. The basic underlying idea of such simulations is very simple. The potentials derived from first principles electronic structure calculations, for example DFT, are included and these electronic structure calculations are performed "on-the-fly" as the MD trajectory is generated [70–72].

3.4.1 Equation of motion

In a system, the microscopic state can be described in terms of the positions R and momenta P of a constituent set of M particles (M atoms or ions here). The M particles in the system move and interact via a potential $V(R)$ and the potential $V(R)$ is assumed to be only a function of the positions. Then, the Hamiltonian H of this system as a

[4]Born-Oppenheimer MD means that the electronic structure is optimized to the ground state at each MD timestep.

function of R and P of all particles is

$$H(R,P) = \sum_{A=1}^{M} \frac{P_A^2}{2m_A} + V(R), \tag{3.41}$$

where the first term on the right hand side is the kinetic energy of all particles and m_A is the mass of individual particles as defined before. The movement of each particle in the system obeys Newton's second law,

$$m_A \ddot{R} = F_A(R), \tag{3.42}$$

where the force applied on each particle is derived from the potential,

$$F_A(R) = -\frac{\partial V(R)}{\partial R_A}. \tag{3.43}$$

In practical simulations, the Hamiltonian and the potential are not continuous functions of particle positions and the positions and velocities can not be obtained continuously with time. Therefore, numerical integration techniques are required to make sure that the particle positions vary smoothly with time. Specifically, these techniques to generate trajectories are based on a discrete timestep and a repeated calculation of forces on the particles. They have special properties of long time energy conservation and short time reversibility. Long time energy conservation ensures that the system stays on (or in fact close to) the constant potential energy surface and the short time reversibility means the time reversible symmetry of the original equation of motion is maintained. One choice of numerical integration technique is the velocity Verlet algorithm [70–72], which uses the position and velocity of each particle at the same instant time t as basic variables. The velocity Verlet algorithm has a Taylor expansion-like form for predicting the new position $R(t+\Delta t)$ and the new velocity $V(t+\Delta t)$ after suitable timestep Δt starting from the old position $R(t)$ and the old velocity $V(t)$ at time t:

$$R(t+\Delta t) = R(t) + V(t)\Delta t + \frac{F(t)}{2m}\Delta t^2, \tag{3.44}$$

$$V(t+\Delta t) = V(t) + \frac{F(t+\Delta t) + F(t)}{2m}\Delta t, \tag{3.45}$$

where $F(t)$ and $F(t+\Delta t)$ indicate the old force at time t and the new force after time step Δt.

3.4.2 Ensemble

In MD calculations, the desired properties of a many-particle system can normally be obtained through computing numerically the time evolution of the system over a sufficiently long time and then averaging the quantities of interest. In addition, the simulations are performed under specific statistical ensembles with fixed values of macroscopic thermodynamic variables such as temperature, pressure, volume, or number of particles. These thermodynamic variables characterizing an ensemble can be regarded as controlled experimental conditions under which an experiment is performed.

The microcanonical ensemble (NVE) is one of the most fundamental and simple ensembles and is characterized by constant number of particles in the simulation cell, constant volume of the cell, and constant total energy. In Born-Oppenheimer MD, the conserved total energy includes the contributions of electrons and nuclei. The electronic energy has the same physical meaning as the DFT energy within the Born-Oppenheimer approximation, i.e., the ground state energy obtained in Eq. (3.16) depends only on the nuclear positions and it defines the potential surface for the nuclear movement. Therefore, the conserved total energy E_{NVE} for the microcanonical ensemble has the form of

$$E_{NVE} = E_e + \sum_{A=1}^{M} \sum_{B>A}^{M} \frac{Z_A Z_B}{R_{AB}} + \sum_{A=1}^{M} \frac{P_A^2}{2m_A}, \tag{3.46}$$

where the three terms on the right hand side are the DFT electronic contribution, the internuclear Coulomb contribution, and the kinetic energy of the nuclei, respectively. The energy conservation condition imposes a restriction on the classical microscopic states accessible to the system and defines a constant potential energy surface in the phase space. The assumption that a system, given an infinite amount of time, will cover the entire constant potential energy surface is known as the ergodic hypothesis. Under the ergodic hypothesis, averages over a trajectory of a system can be treated as averages over the corresponding microcanonical ensemble.

The standard microcanonical ensemble can be extended to include other controlled

thermodynamic variables. For example, the possibility to control the average temperature (as obtained from the average kinetic energy of the nuclei) is welcome for physical reasons. This can be achieved by establishing a thermodynamic coupling between the original system and an appropriate infinitely large bath or reservoir of heat, i.e., additional degrees of freedom that control the quantity under consideration are added to the original system and the MD simulation is then performed in the extended microcanonical ensemble with a modified conserved total energy. The extended ensemble including constant temperature is called the canonical ensemble (NVT). In the implementation of the canonical ensemble, the Nosé-Hoover chain [73] thermostat is one practical option to control temperature [70–72]. The Nosé-Hoover chain thermostat uses a chain of thermostats to impose the desired temperature and assures ergodic sampling of the entire phase space. In Born-Oppenheimer MD, the conserved total energy E_{NVT} (or Hamiltonian) for the entire extended system including the thermostat has the form:

$$\begin{aligned} E_{NVT} &= E_e + \sum_{A=1}^{M}\sum_{B>A}^{M}\frac{Z_A Z_B}{R_{AB}} + \sum_{A=1}^{M}\frac{P_A^2}{2m_A} \\ &\quad + \sum_{i=1}^{M'}\frac{p_{\xi_i}^2}{2Q_i} + N_f kT\xi_1 + kT\sum_{i=2}^{M'}\xi_i, \end{aligned} \tag{3.47}$$

where the fist three terms on the right hand side are exactly the same as defined in Eq. (3.46) and the remaining terms are contributions of the thermostat chain. N_f is the particle degrees of freedom, ξ_i is the thermostat degrees of freedom, and p_{ξ_i} is the momentum of ξ_i. In addition, Q_i are the thermostat fictitious masses assigned automatically from the specified particle relaxation time,

$$Q_1 = \frac{N_f kT}{\omega^2}, \tag{3.48}$$

$$Q_i = \frac{kT}{\omega^2}, \tag{3.49}$$

where the ω is in general the maximal phonon or vibrational frequency of the many-particle system.

Similar to temperature, pressure, chemical potential, and many other quantities can be coupled into the extended ensemble to simulate the experimental conditions. Those

ensembles are the isothermal-isobaric ensemble (NPT), the grand canonical ensemble (μVT) etc, which have not been used in the thesis.

Chapter 4

Water and ice on kaolinite

In order to understand the role played by kaolinite in heterogeneous ice nucleation, an extensive DFT study has been performed for water on its (001) basal plane. Water monomers at low coverage, water clusters, water bilayers and water multilayers have all been examined. The most important and interesting results from this study are: (i) water monomers bind strongly to kaolinite compared to many other substrates. In the preferred adsorption structure water accepts two H bonds from and donates one H bond to the substrate, revealing that kaolinite, like water, is amphoteric with the ability to accept and donate H bonds; (ii) clustering of adsorbed water molecules is not significantly favored. All water clusters (dimers, tetramers, and hexamers) examined are, at best, equally stable to water monomers; (iii) a 2D ice-like bilayer, with a stability matching that of ice Ih has been identified implying that water can wet kaolinite; (iv) multilayer ice growth is not favored, being considerably unstable compared to bulk ice, indicating that the water covered kaolinite surface is itself "hydrophobic". Overall it is seen that amphoterism of the hydroxylated surface is key to many of the interesting properties of kaolinite with regard to water adsorption and ice nucleation, revealing that the behavior of water on kaolinite is more complex and interesting than previously thought to be and highlighting the need for further theoretical and experimental work.

4.1 Introduction

The nucleation of water into ice is a familiar everyday process and one of central importance to a wide variety of disciplines such as environmental chemistry, astrophysics, and biology. However, despite being studied since antiquity, our understanding of ice nucleation is far from complete at the molecular scale. This is particularly true for so-called heterogeneously catalyzed nucleation, in which water is encouraged to nucleate through the presence of an "ice nucleating agent". Mainly this is because of the complexity of the problem: interactions between water molecules in the nascent clusters are altered by the substrate, leading to the formation of new water structures not observed in the gas phase, altered H bond strengths, dynamics and stabilities.

Great strides have been made in recent years to understand water adsorption and ice nucleation on model substrates such as metals and metal oxides. Often studied under well-defined UHV conditions some of these systems are rather well characterized: water-ice adlayers on Ru, Pt, and TiO_2 surfaces have, for example, been interrogated with almost every conceivable surface science probe [6, 7, 9, 10, 21, 22, 74]. Clay mineral surfaces have also been widely examined [21, 22, 75–77], however, less is known at the molecular level about the adsorption of water and the nucleation of ice on clay mineral surfaces. Clay minerals are important since small clay particles are one of the key types of material that encourage the nucleation of ice in the upper atmosphere [8]. A better understanding of ice nucleation on such particles is greatly needed for developing and improving models of cloud formation and precipitation, and prerequisites to narrowing existing uncertainties in climate change scenarios.

Of the many clay minerals known to be effective ice nucleating agents, the mineral kaolinite ($Al_2Si_2O_5(OH)_4$) features prominently. Field studies reveal that kaolinite is often an abundant foreign material at the central nucleus of snow crystals [8]. Partly this is down to the great abundance of kaolinite in the upper atmosphere. As one of the most common minerals, produced by the chemical weathering of aluminum silicate minerals like feldspar, there is simply a lot of the stuff up there, existing as small nano-

to micro-meter sized dust particles. And, partly this is down to a particular efficiency as an ice nucleating agent. The threshold temperature for ice nucleation - one criterion by which the ice nucleating ability of a material is judged - is rather high on kaolinite, at around -9 to -11 °C in the deposition mode [8].

The standard explanation for why kaolinite is an effective ice nucleating agent relates to its crystal structure, which is now well characterized [78–82]. As a layered aluminosilicate it is thought[1] to offer perfect cleavage along its (001) basal plane exposing on each side of a finite crystal an hydroxylated and a siloxane (001) surface. The hydroxylated (001) surface is said to be hydrophilic whereas the siloxane (001) surface is said to be hydrophobic [83]. The hydrophilic hydroxylated (001) surface is further thought to be a good surface for ice nucleation since it presents a quasi-hexagonal arrangement of hydroxyl groups with O-O separations rather close to the O-O distances in the basal plane of ice Ih [8] (Fig. 4.1). Thus kaolinite is believed to provide a suitable template for ice nucleation in the same spirit as the anthropogenic ice nucleating agent, AgI.

Although kaolinite and water on kaolinite has been widely studied [83–87], many questions relating to the molecular level details of water adsorption and ice-like overlayer growth on kaolinite remain unanswered. Here, I make a start at addressing these issues through an extensive series of DFT calculations for water adsorption on the (001) basal plane of kaolinite. Adsorption on the hydroxylated (001) surface alone was considered with the coverage of adsorbed water ranging from monomers at low coverage to ice-like multilayers. The most important and interesting results from this study are: (i) water monomers bind strongly to kaolinite compared to many other substrates. In the preferred adsorption structure water accepts two H bonds from and donates one H bond to the substrate, revealing that kaolinite, like water, is amphoteric with the ability to accept and donate H bonds; (ii) clustering of adsorbed water molecules is not significantly favored. All water clusters (dimers, tetramers, and hexamers) examined are equally stable to or less stable than isolated monomers; (iii) a 2D ice-like bilayer,

[1] Chapter 5 focusses on testing this widely held assumption.

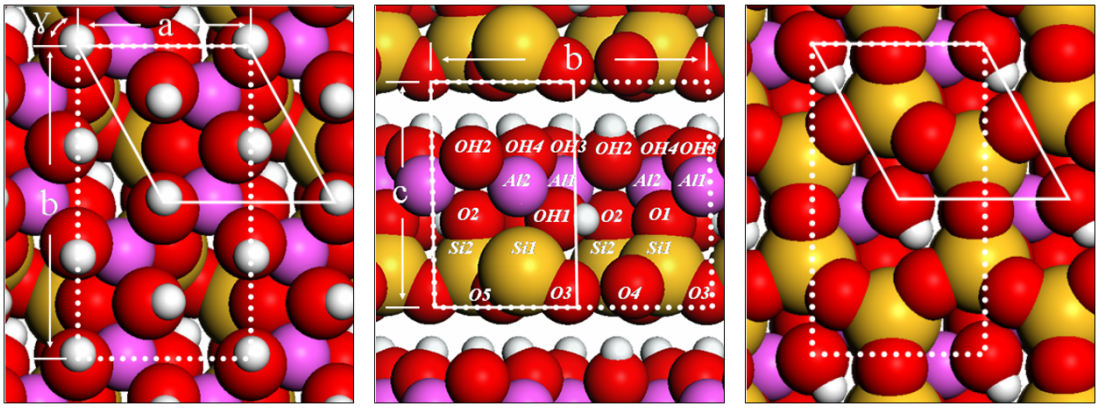

Figure 4.1: Bulk kaolinite crystal structure seen from the hydroxylated (001) face (left), the side (middle), and the siloxane (001) face (right). White spheres, red spheres, purple spheres, and dark yellow spheres represent hydrogen, oxygen, aluminium and silicon, respectively. The dotted lines indicate the conventional unit cell of bulk kaolinite and the solid lines the primitive unit cell. The labels for the lattice parameters reported in Table 4.1 and atoms listed in Table 4.2 are also indicated.

with a stability matching that of ice Ih, has been identified, implying that water can wet kaolinite; (iv) multilayer ice growth is not favored, being considerably unstable compared to bulk ice, indicating that the water covered kaolinite surface is itself hydrophobic. A key conclusion to come from this work is that I call into question the suggestion that kaolinite is a good ice nucleating agent because it provides a close lattice match to the basal plane of ice. Instead I suggest that the amphoterism of the hydroxylated substrate is key to many of the interesting properties of kaolinite with regard to water adsorption and ice nucleation.

This chapter is a comprehensive account of water adsorption studies on the hydroxylated (001) kaolinite surface and the plan for the remainder is the following. In the next section I discuss the computational set-up employed. Following this in Section 4.3 I discuss some aspects of bulk kaolinite and in Section 4.4 the structure of the clean (001) surface of an isolated layer of kaolinite is addressed. The main body of the results, which comprise an extensive series of calculations of water adsorption on the hydroxylated (001) surface of an isolated layer of kaolinite, are presented in Section

4.5 along with a discussion and some conclusions in Section 4.6.

4.2 Computational details

DFT calculations within the plane-wave pseudopotential approach, as implemented in the CASTEP code [35, 36], have been performed. Vanderbilt ultrasoft pseudopotentials [67] generated by the CASTEP code have been used throughout. With these pseudopotentials I have chosen to use a plane wave cutoff of 700 eV, which ensures that the total energy of each isolated atom (Si, O, Al and H) is converged to within 10 meV/atom of "absolute" convergence achieved at 1500 eV. Relative energy differences, such as cohesive energies and adsorption energies reported here are thus expected to be fully converged with respect to plane wave cutoff. Extensive tests on the performance of the pseudopotentials for computing the atomization energies and structures of small molecules as well as bulk silicon and aluminium have been performed. These calculations, some of which are reported in Appendix A, give confidence that the chosen pseudopotentials (and cutoff) are sufficiently reliable and transferable to treat the system at hand. The GGA-PBE [50, 51] exchange-correlation functional has been used throughout. Recent benchmark studies on the performance of DFT-PBE for the calculation of hydrogen bond strengths and lengths for a variety of typical hydrogen-bonded system show that PBE routinely predicts hydrogen bond strengths to within an accuracy of 0.04 eV/H bond (1 kcal/mol) or better compared to the results obtained from high level quantum chemistry methods with large basis sets [88, 89]. In addition, PBE yields a cohesive energy for a commonly examined model of ice Ih of -0.66 eV/H_2O [90, 91], which agrees reasonably well with the experimental value of -0.61 eV/H_2O[2].

[2]Using the Bernal-Fowler ice Ih model of Ref. [90], the PBE exchange-correlation functional, a 4×4×4 Monkhorst-Pack $\boldsymbol{k}$ point mesh, ultrasoft pseudopotentials, and a plane wave cutoff of 700 eV, a cohesive energy of -0.66 eV/H_2O is obtained. The corresponding experimental value, with contributions from zero point energy removed, is -0.61 eV/H_2O (Ref. [92]). Further, it is noted that the calculated zero point energy of this ice Ih model is at 0.13 eV/H_2O consistent with the experimental zero point

And, as one will see below, it reproduces the lattice constants and layer separation of kaolinite bulk to within, at worst, 1.4% of the experimental values.

A variety of unit cells have been used to examine bulk kaolinite and water adsorption on its (001) surface. For bulk kaolinite the conventional unit cell, $Al_4Si_4O_{10}(OH)_8$, has been employed for structure optimizations along with a $3\times2\times2$ Monkhorst-Pack $\boldsymbol{k}$ point mesh [66]. In these structure optimizations the unit cell and all atoms within it were fully allowed to relax. Test calculations with a denser $6\times4\times4$ $\boldsymbol{k}$ point mesh yield a total energy and structure identical to those with the $3\times2\times2$ $\boldsymbol{k}$ point mesh, i.e., they both have the same total energy and the volumes of the two optimized cells differ by $<0.04\%$. Water adsorption was examined on a single layer of kaolinite in surface unit cells ranging from p(1×1) to p(3×3) and with a vacuum region between slabs of more than 10 Å. In these calculations Monkhorst-Pack $\boldsymbol{k}$ point meshes equivalent to at least $4\times4\times1$ sampling within a 1×1 unit cell were used. During structure optimizations all atoms are fully relaxed until all forces are reduced below 2×10^{-2} eV/Å.

4.3 Bulk kaolinite

I now address several aspects of bulk kaolinite in order to further evaluate the accuracy of the computational set-up used and to illustrate this somewhat complex layered aluminosilicate. Specifically, I discuss the crystal structure and electronic structure of bulk kaolinite.

4.3.1 Crystal structure

As shown in Fig. 4.1, kaolinite is a layered aluminosilicate. Each layer is comprised of an aluminate octahedrally coordinated sublayer connected to a silicate tetrahedrally

energy (0.12 eV/H_2O).

coordinated sublayer. The oxygen atoms connected exclusively to aluminium atoms exist as hydroxyl groups. Most of the hydroxyl groups are located on the (001) surface of each layer and hold adjacent layers together through hydrogen bonds. Each hydroxyl group on the basal plane is surrounded by a hexagonal arrangement of six other hydroxyl groups, which, as I will discuss below, is the textbook explanation for why kaolinite is thought to be a good material at nucleating ice [8].

The bulk crystal structure of kaolinite is reasonably well characterized thanks to X-ray [80, 82] and neutron diffraction [78, 79, 81] experiments as well as DFT [85, 86, 93, 94] calculations. There is, however, a minor disagreement concerning the space group: most experiments [78, 80–82] report C1 (centered symmetry), but one [79] reports P1 (asymmetry). In order to address this issue of the space group I performed a series of DFT structure optimizations starting from each of the slightly different experimental crystal structures. The lowest total energy structure obtained from these calculations was that which started from the experimental structures reported by Neder et al. [82] and by Bish [81], i.e., both initial structures yield essentially identical final structures with the same total energy, the same internal bond lengths, and unit cell volumes that differ by only 0.025%. In agreement with most experimental results the structure has indeed a C1 space group.

In Tables 4.1 and 4.2 the optimized lattice constants and internal bond lengths obtained here are reported and compared to experimental results. As can be seen from Table 4.1 the calculated lattice constants agree well with those determined from experiment, yielding a cell volume that is only 3% larger than experiment. In particular it is noted that the c height of the unit cell, which is largely determined by interlayer hydrogen bonding, is within 1.4% of the experimental value, indicating that the chosen computational set-up (exchange-correlation functional, $\boldsymbol{k}$ point mesh, pseudopotentials and cutoff energy) is suitable for describing this weak interlayer interaction. Likewise it can be seen from Table 4.2 that the various internal bond lengths determined here generally agree with the experimental values. It is noted that of the two sets of experi-

Table 4.1: Comparison between computed and experimental lattice parameters for the conventional unit cell of bulk kaolinte. See Fig. 4.1 for a definition of some of the lattice parameters.

	This work	Exp.[a]	Exp.[b]	Exp.[c]
Length (Å)				
a	5.196	5.154	5.1535	5.1490
b	9.021	8.942	8.9419	8.9335
c	7.485	7.401	7.3906	7.3844
Angle (°)				
α	91.70	91.69	91.926	91.930
β	104.72	104.61	105.046	105.042
γ	89.78	89.82	89.797	89.791
Cell volume (Å^3)	339.17	328.70	329.91	327.84

[a] Ref. [82] (X-ray single crystal diffraction experiments).

[b] Ref. [81] (low temperature (1.5 K) neutron powder diffraction experiments).

[c] Ref. [79] (neutron powder diffraction experiments).

mental data given in Table 4.2 I find better agreement, in terms of Al-O and Si-O bond lengths, with the X-ray diffraction data of Neder et al. [82] rather than the neutron diffraction data reported by Bish [81]. For the O-H distances, however, the calculations agree with the more reasonable values of $\sim$1 Å to come from neutron diffraction as opposed to the unrealistically short values of $\sim$0.75 Å reported from X-ray diffraction.

4.3.2 Electronic structure

The electronic structure of bulk kaolinite is now briefly discussed. In Fig. 4.2a the density of states (DOS) of kaolinite is displayed. It can be seen from this plot that kaolinite is an insulator with a DFT-PBE Kohn-Sham band gap of $\sim$5.6 eV. I am not aware of any experimental reports for the (optical) band gap of kaolinite. However, it is safe to assume that the experimental band gap will be larger than the $\sim$5.6 eV Kohn-Sham band gap determined here. For example, the computed DFT-PBE Kohn-Sham band gaps of α-quartz (SiO_2), which resembles the silicate sublayer of kaolinite, and corundum (Al_2O_3), which resembles the aluminate sublayer of kaolinite are at $\sim$6.0 eV and $\sim$6.4 eV, respectively, significantly smaller (by $\sim$30%) than the corresponding experimental (optical) band gaps. Analysis of the projected density of states (PDOS) of bulk kaolinite over the s and p orbitals of each element, as shown in Fig. 4.2b-e, reveals that the valence band of kaolinite is mainly comprised of oxygen p states: a filled set of p orbitals characteristic of many oxides. The band below the valence band is mostly of oxygen s character. The nature of the conduction band is less clear with s and p contributions from each of the elements and in particular significant silicon and aluminium p character.

Table 4.2: Comparison between the computed and experimental internal bond lengths of bulk kaolinite. The labels given for each element are indicated in Fig. 4.1.

Bond	Distance (Å)		
	This work	Exp.[a]	Exp.[b]
Si(1)-O(1)	1.612	1.614	1.618
Si(1)-O(3)	1.634	1.620	1.611
Si(1)-O(4)	1.630	1.618	1.620
Si(1)-O(5)	1.637	1.628	1.619
Si(2)-O(2)	1.610	1.605	1.612
Si(2)-O(3)	1.636	1.622	1.617
Si(2)-O(4)	1.629	1.616	1.616
Si(2)-O(5)	1.633	1.615	1.608
Al(1)-O(1)	1.961	1.948	1.927
Al(1)-O(2)	2.038	2.001	1.930
Al(1)-OH(1)	1.931	1.921	1.913
Al(1)-OH(2)	1.864	1.853	1.890
Al(1)-OH(3)	1.857	1.849	1.865
Al(1)-OH(4)	1.860	1.862	1.915
Al(2)-O(1)	2.029	1.990	1.931
Al(2)-O(2)	1.950	1.946	1.919
Al(2)-OH(1)	1.929	1.921	1.912
Al(2)-OH(2)	1.863	1.867	1.896
Al(2)-OH(3)	1.862	1.858	1.886
Al(2)-OH(4)	1.863	1.853	1.910
O-H(1)	0.974	0.75	0.975
O-H(2)	0.969	0.76	0.982
O-H(3)	0.970	0.77	0.976
O-H(4)	0.969	0.88	0.975

[a] Ref. [82] (X-ray single crystal diffraction experiments).

[b] Ref. [81] (low temperature (1.5 K) neutron powder diffraction experiments).

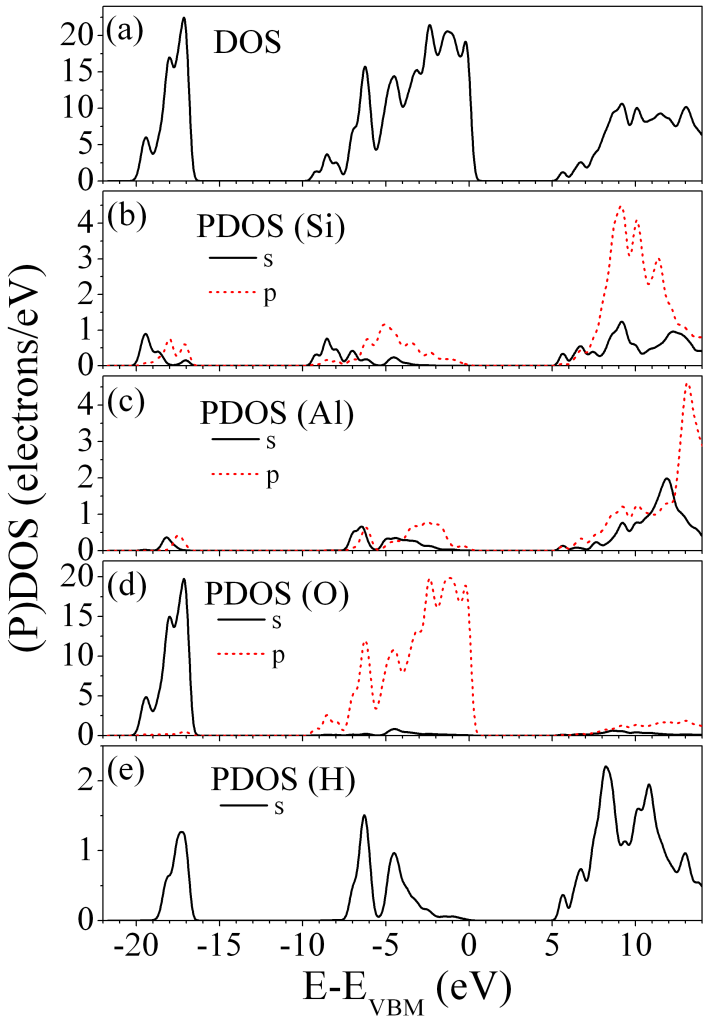

Figure 4.2: DOS of bulk kaolinite (a) and PDOS of the s and p orbitals of all the Si (b), Al (c), O (d), and H (e) atoms in bulk kaolinite. The energy zero is E_{VBM}, the energy of the valence band maximum. A Gaussian broadening of 0.2 eV has been applied to all densities of states. Note that the range of the y-axis differs in each plot.

4.4 Single layer of kaolinite

The (001) surface of kaolinite is the basal plane and the plane which kaolinite crystals predominately expose [95–97]. Thus the (001) surface and in particular the hydroxylated (001) surface is the surface of primary interest in adsorption studies. After optimizing the bulk structure, the bulk was simply cleaved along the c-axis through the interlayer hydrogen bonds to form a single layer of kaolinite and its (001) surface. The structure of the single isolated layer resembles that of a layer in bulk kaolinite rather closely. All Si-O and Al-O distances, for example, are within 0.1 Å of their bulk values. Likewise the hydroxyl bond lengths remain essentially unchanged (within 0.005 Å) after cleavage along the (001) surface. The only notable difference between a layer in bulk and a layer in vacuum is that 1/3 of the surface hydroxyl groups of the isolated kaolinite layer tilt and become almost parallel to the surface. This can be seen by comparing the structure of the hydroxylated (001) surface in bulk (Fig. 4.1) and for an isolated surface layer (Fig. 4.3a). It will shown below that this orientational flexibility of the OH groups at the kaolinite surface is crucial to the ability of kaolinite to support a stable water overlayer. In addition, the single layer of kaolinite is only a simple model used in this chapter, and more details of the (001) surface of kaolinite will be discussed in next chapter.

The cleavage energy, E_{cleave}, of this layer of kaolinite can be obtained from the following relation:

$$E_{cleave} = (E_{slab} - E_{bulk})/(2 \cdot A), \tag{4.1}$$

where E_{slab} is the total energy of a single isolated layer of kaolinite and E_{bulk} is the total energy of a single kaolinite layer in bulk. The factor 2 in the denominator accounts for the fact that two (001) surfaces, the hydroxylated and the siloxane surfaces, are created. The area of the 2D surface supercell is A. The cleavage energy obtained is 8 meV/Å^2. This corresponds to a layer-layer interaction in bulk kaolinite of $\sim$0.36 eV/primitive cell. Since there are three interlayer hydrogen bonds in bulk kaolinite per primitive cell, this corresponds to an average interlayer hydrogen bond strength of $\sim$0.12 eV/H bond.

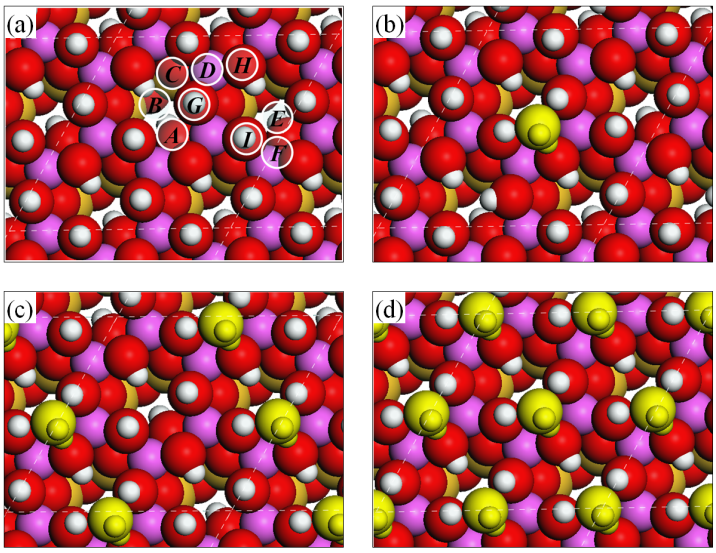

Figure 4.3: (a) Top view of the clean hydroxylated (001) surface of a single layer of kaolinite with nine possible adsorption sites for water monomers indicated (A-I). (b)-(d) The most stable water monomer adsorption structures identified at 1/12, 1/6, and 1/3 ML. Here and in subsequent figures in this chapter adsorbed water molecules are colored yellow for clarity. In (a)-(d) the thin dashed lines indicate the p(2×2) unit cell.

It was sought to consider the effect of temperature on the energetic cost to cleave a single layer of kaolinite by computing the phonon (and zero point) contribution to the cleavage free energy, $F_{cleave}(T)$. This is obtained from the relation:

$$F_{cleave}(T) = E_{cleave} + \Delta F^{vib}(T,\omega)/(2 \cdot A), \tag{4.2}$$

where $\Delta F^{vib}(T,\omega)$ is the temperature dependent vibrational free energy contribution to $F_{cleave}(T)$, given by

$$\begin{aligned} \Delta F^{vib}(T,\omega) \;=\; & (\sum(1/2)\hbar\omega_{slab} - \sum(1/2)\hbar\omega_{bulk}) \\ & +(\sum kTln(1-exp(-\beta\hbar\omega_{slab})) \\ & -\sum kTln(1-exp(-\beta\hbar\omega_{bulk}))). \end{aligned} \tag{4.3}$$

The first two terms on the right hand side of Eq. (4.3) give the difference in zero point energies between an isolated kaolinite layer and a layer in bulk. The phonon frequencies, ω, which enter Eq. (4.3), were obtained in the harmonic approximation at

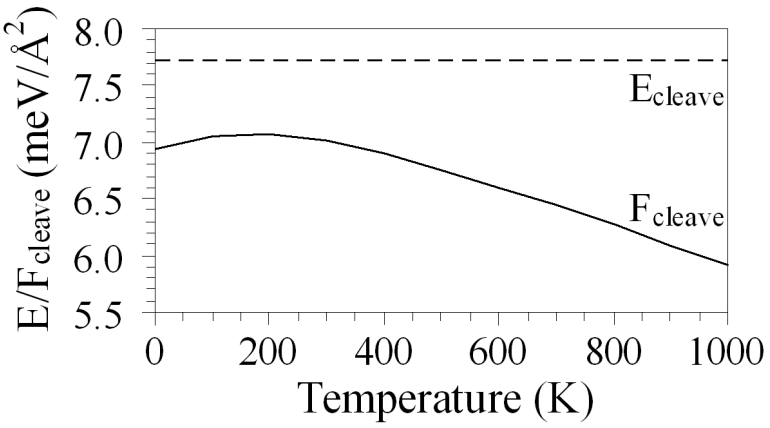

Figure 4.4: The cleavage energy, E_{cleave} (Eq. (4.1)), of a single layer of kaolinite (dashed line) and the cleavage free energy, E_{cleave} (Eq. (4.2)) (solid line). At T = 0 K the two quantities differ by the differenc in zero point energy between bulk kaolinite and a single layer of kaolinite in vacuum, which is $\sim$0.8 meV/Å^2.

the Γ point of the vibrational Brillouin zone through the finite displacements method. The zero point energy difference obtained with this procedure turns out to be only -40 meV/primitive cell, which corresponds to a change in the cleavage free energy of -0.8 meV/Å^2. It is noted that this result is a reduction in the cleavage free energy, since as one would expect, an isolated kaolinite layer has less zero point energy than a layer held in bulk. The second two terms on the right hand side give the finite temperature phonon contribution to the cleavage free energy. From Fig. 4.4 it can be seen that this too makes a rather small contribution, reducing the cleavage free energy by $\leqslant$1 meV/Å^2 at all temperatures up to 1000 K. Thus, overall, it is seen that the energetic cost to cleave a layer of kaolinite from bulk is reasonably independent of temperature and in the range of $\sim$8 to $\sim$6 meV/Å^2.

The electronic structure of the clean single layer of kaolinite was examined. The DOS and projected DOS (not shown) were similar to those observed for bulk kaolinite. Small changes in the peak heights and widths were apparent with the center or, more precisely, the first moment of the valence band about 0.2 eV closer to the valence band maximum compared to the bulk. In addition the computed band gap is $\sim$1 eV smaller than that computed for the bulk.

4.5 Water and ice adsorption

Water adsorption has been examined at a range of coverages and in a variety of structures on a single layer of kaolinite. Since previous studies [83, 95] have shown that water adsorbs more weakly on the "hydrophobic" siloxane surface than it does on the "hydrophilic" hydroxylated surface, here only the hydroxylated (001) surface is examined. Adsorption energies, E_{ads}, per water are defined as

$$E_{ads} = (E_{nH_2O/slab} - E_{slab} - n \cdot E_{H_2O})/n, \tag{4.4}$$

where $E_{nH_2O/slab}$ and E_{slab} are the total energies of an *n* water adsorption system and the clean surface, respectively. E_{nH_2O} is the total energy of an isolated water molecule[3]. Within this definition a negative adsorption energy thus corresponds to an exothermic adsorption process. In order to interpret the adsorption cases explicitly and conveniently, a monolayer (ML) is defined as one water molecule for every surface hydroxyl group. Thus in the most commonly employed surface supercell (Fig. 4.3a) one adsorbed water molecule corresponds to a coverage of 1/12 ML.

4.5.1 Monomer adsorption

Fig. 4.3a displays the hydroxylated (001) surface with the sites considered for water monomer adsorption indicated by the labels A-I. With regard to the surface hydroxyl groups I can classify four of these as threefold "hollow" sites (A-D), two as twofold "bridge" sites (E and F), and three as onefold "top" sites (G-I). All of these sites were investigated for water monomer adsorption at a coverage of 1/12 ML. During the structure optimizations the water molecules and kaolinite were fully allowed to relax and

[3]The energy of the isolated water molecule was obtained from a calculation of water in a cube of length 20 Å using only the Γ point of the Brillouin zone.

it turned out that upon optimization all the initial structures with water molecules adsorbed at top sites and one at a bridge site moved to the threefold hollow sites, which prove to be most stable sites for water monomer adsorption on this surface. At the hollow sites several similar adsorption structures, with adsorption energies all within $\sim$0.1 eV of each other, have been identified. The most stable of these is adsorption at hollow site A (Fig. 4.3b). At this site the monomer sits upright, in the plane of the surface normal, donating one hydrogen bond to and accepting two hydrogen bonds from the substrate. Thus kaolinite, like water, is amphoteric and able to accept and donate hydrogen bonds. The hydrogen bond the adsorbed water molecule donates is, at 1.73 Å, considerably shorter than the two hydrogen bonds it accepts, which are both $\sim$2 Å (2.00 Åand 2.03 Å). The adsorption energy of the water molecule at this site is -0.58 eV/H_2O. This adsorption energy agrees reasonably well with a previous DFT study [83] in which a binding energy of -0.64 eV was reported for hollow site adsorption.

The coverage dependence of the monomer adsorption energy was then investigated by increasing the number of water monomers in the cell to two (1/6 ML) and subsequently to four (1/3 ML). At each coverage several combinations of monomer adsorption site were considered. The most stable structures identified at 1/6 ML and 1/3 ML are shown in Fig. 4.3c and d, respectively. In each structure all water molecules reside at the stable hollow sites A and the adsorption energies of these overlayers are both -0.57 eV/H_2O, i.e., essentially identical to the adsorption energy at 1/12 ML. Thus, the amount of water monomers on the surface has only a small effect on the adsorption energy in this coverage regime, indicating that the interaction between adjacent water molecules is weak. It is noted, however, that once reaching 1/3 ML all the non-connected threefold sites have been filled and there is not enough space for the adsorbed water molecules to remain isolated. At this coverage one may thus expect water cluster or extended overlayer formation. Adsorption of water clusters will be discussed in the next subsection.

It is interesting to ask to what extent zero point vibrations affect the adsorption en-

ergy of water on this surface. To this end, vibrational frequency calculations were performed for the adsorbed water monomer at 1/3 ML. The zero point energy contribution to the adsorption energy, obtained by taking the difference in the zero point energy of the adsorption system, the isolated water molecule and the clean surface, is 0.13 eV/H_2O[4]. Specifically, there is 0.13 eV/H_2O more zero point energy in the adsorption system compared to the isolated fragments, which reduces the water monomer adsorption energy from $\sim$-0.58 eV/H_2O to $\sim$-0.45 eV/H_2O.

4.5.2 Cluster and 1D chain adsorption

Since clustering tends to be facile for gas phase water molecules and water adsorbed on many types of materials, such as oxide, salt, and metal surfaces [22, 98–102], the possibility of water cluster formation has been examined. Specifically, water dimer, tetramer, and hexamer adsorption were considered.

Upon moving beyond the monomer, the number of possible adsorption structures rapidly increases with cluster size and comprehensive searches of configuration space become challenging. Taking the adsorbed dimer, for example, the two water molecules in the dimer can act either as hydrogen bond donors and/or as hydrogen bond acceptors to the surface, and each water molecule may be located at hollow, bridge or top adsorption sites. Of these many possibilities I have tested fifteen different dimer structures and of those considered the most stable one identified upon optimization is the one shown in Fig. 4.5a. In this structure the donor water molecule in the dimer accepts two hydrogen bonds from the substrate and the other water donates one hydrogen bond to the surface. However, the adsorption energy of this structure is only -0.55 eV/H_2O, which is slightly less than the adsorption energy of a water monomer (-0.58 eV/H_2O).

[4]Upon analysis of the vibrational modes present in the adsorption system, it is found that the additional zero point energy comes from the new hindered rotations, translations, and vibrations present in the adsorption system. It is interesting to note, however, that these new modes are enough to compensate, in terms of zero point energy, for a significant softening of one of the OH stretch frequencies in the adsorbed water molecule.

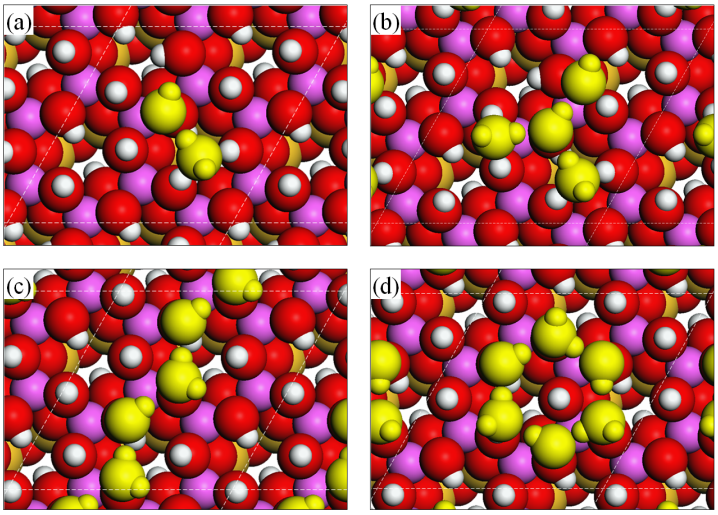

Figure 4.5: Top views of the most stable structures identified for an adsorbed dimer (a), an adsorbed tetramer (b), an adsorbed 1D chain (c), and an adsorbed hexamer (d) on the hydroxylated (001) surface of a single layer of kaolinite.

Thus on this surface dimer formation does not appear to be energetically favored, or, at least, I have not been able to identify any dimer structure that is more stable than two separated adsorbed water monomers. This is the opposite of what is predicted and observed on many other surfaces [22, 98, 102–106]. In this system the single hydrogen bond formed between the two water molecules in the dimer is not sufficient to compensate for the distortions of the two water molecules away from their optimal adsorption sites, which break hydrogen bonds to the substrate.

Similar to water dimers, fourteen different adsorbed tetramer structures have been examined, including cyclic and non-cyclic structures [98]. The most stable structure of those considered is shown in Fig. 4.5b. The four water molecules do not form a cyclic structure as they do in the gas phase, instead three water molecules are connected to one central water molecule, which donates one hydrogen bond to the surface. The adsorption energy of this structure is -0.58 eV/H_2O, which is equal to that of the water monomer. Thus the clustering of four water molecules does not lead to any energetic stabilization.

Adsorbed cyclic hexamers have been observed with STM on several hexagonal metal surfaces [103, 105–107], and so the adsorption of cyclic water hexamers was examined here. The symmetry match of the hexamer with the substrate reduces the number of likely adsorption structures considerably but still twelve trial structures were considered. Some were built from adsorbed bilayers (below), and some hexamers considered had all six water molecules initially flat on the surface based on the structure reported on Pd(111) and Ru(0001) [108, 109]. However, the most stable adsorbed hexamer identified is one that resembles the structure of a gas phase cyclic water hexamer with three water molecules directed at the surface and the other three to the vacuum. The adsorption energy of this hexamer is -0.59 eV/H_2O and its structure is shown in Fig. 4.5d. Thus the adsorbed hexamer is slightly more stable than separated monomers, but the energy gain upon clustering is by no means large.

Since 1D water chains are found experimentally at, for example, steps of the Pt(111) surface [110, 111], adsorbed 1D water chains on kaolinite have been examined. Chains with a coverage of 1/3 ML (four water molecules per cell) and 1/2 ML (six water molecules per cell) were also considered with water molecules arranged in various starting configurations. The most stable 1D chain structure, which has an adsorption energy of -0.57 eV/H_2O, is shown in Fig. 4.5c. It is comprised of flat water molecules and water molecules in the plane of the surface normal directed towards the surface with every water molecule being a hydrogen bond acceptor and a hydrogen bond donor. This structure is equally stable to isolated water monomers and thus not necessarily prohibited from forming on energetic grounds.

4.5.3 2D overlayer adsorption

The hydroxylated (001) surface presents a quasi-hexagonal arrangement of hydroxyl groups with computed next-nearest neighbour O-O distances ranging from 2.81 to 3.41 Å . With an equivalent O-O distance of 2.71 Å in ice Ih, there is a DFT-PBE mismatch that ranges from 0.1 Å (3.7%) to 0.7 Å(25%). The corresponding experimental dis-

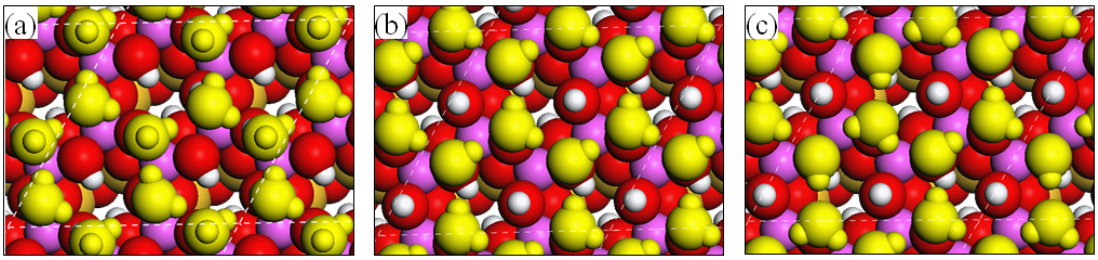

Figure 4.6: Top views of some 2D overlayer adsorption structures examined at a coverage of 2/3 ML on the hydroxylated (001) surface of kaolinite. (a) is the conventional but unstable H-up overlayer. (b) is the proton ordered H-down overlayer. (c) is a partially proton disordered H-down overlayer.

tances are 2.77 to 3.45 Å in bulk kaolinite [81, 82] and 2.75 Å in ice Ih [92], yielding a rather similar experimental mismatch of 0.7-25%. On this substrate I explored the possibility of adsorbing hexagonal ice-like overlayers. An extensive range of overlayer structures were considered with different coverages and various arrangements of the substrate and overlayer hexagonal meshes[5]. I discuss now a range of commensurate overlayers all with a coverage of 2/3 ML. Specifically these include a conventional ice bilayer with each water molecule directly above an hydroxyl of the substrate. In this conventional bilayer structure half the water molecules are parallel to the surface and the other half sit in the plane of the surface normal with one of their two OH groups pointing up into the vacuum (Fig. 4.6a). In borrowing the terminology of bilayer adsorption studies on metals this is described as a "H-up" bilayer. A related bilayer structure can be constructed by turning the OH groups that dangle into the vacuum in the H-up bilayer toward the surface, yielding a structure known as a "H-down" bilayer (Fig. 4.6b) [112]. Mixed H-up plus H-down and several other commensurate but non-

[5]The structures considered included commensurate overlayers in which the hexagonal overlayer and substrate meshes were in registry, in cells ranging from p(1×1) to p(3×3) all at 2/3 ML. Non-commensurate overlayers with longer range periodicities were also considered. For example, a 6/7 ML structure in a $\sqrt{7} \times \sqrt{7}$-R(41°) cell was considered. The latter structure was examined because it had a small epitaxial mismatch of just ∼4%. However, this and other overlayers considered were all less stable than the H-down overlayer discussed. Specifically the $\sqrt{7} \times \sqrt{7}$-R(41°) overlayer yielded an adsorption energy of ∼-0.60 eV/H_2O and several $\sqrt{3} \times \sqrt{3}$-R(30°) overlayers considered yielded adsorption energies of ∼-0.58 eV/H_2O.

bilayer-like models were also considered, including mixed water-hydroxyl overlayers previously reported for water on metal surfaces [91, 108, 109, 113, 114].

The most stable overlayer identified on this surface is a H-down structure with an adsorption energy of -0.65 eV/H_2O. The adsorption energy in the H-up version of this structure is quite a bit less at -0.48 eV/H_2O[6]. From the resulting structures of the optimized bilayers it is clear why the H-down structure is favored over the H-up structure: in the H-down system there is no dangling hydrogen bonds ensuring that each water molecule is fully coordinated being involved in four hydrogen bonds.

The structure of the H-down overlayer, shown in Fig. 4.6b, differs significantly from a bilayer in ice, most prominently in terms of the O-O buckling between the two types of water molecules in the bilayer. In ice the O-O buckling is $\sim$0.96 Å, but the overlayer identified here is essentially a flat overlayer with a buckling between the two types of water molecule of $\sim$0.01 Å. In addition, the in-plane H_2O-H_2O distances are all between 2.90 and 3.06 Å, noticeably larger than the O-O distances in ice, which are 2.71 Å in the calculations. The range of O-O distances in the overlayer reflects an asymmetry in the substrate with two different hexagonal sets of O-O distances that the water molecules partly compensate for by displacing from the precise atop sites.

As I have said the adsorption energy of the H-down overlayer is -0.65 eV/H_2O. This is noteworthy because it is essentially identical to the computed cohesive energy of ice Ih (-0.66 eV/H_2O). It has been argued that water has the ability to wet a substrate when the adsorption energy matches or exceeds the cohesive energy of ice [91]. Thus with this criterion, and to within the accuracy of the current computational set-up, the overlayer identified here has the potential to wet kaolinite. To test this finding, the relative energy of ice and the H-down overlayer with several other exchange-correlation functionals (RPBE [52], PBE-WC [53], and PW91 [54]) have been evaluated. As shown

[6]All mixed H-up plus H-down structures considered yielded adsorption energies between the -0.65 eV/H_2O and -0.48 eV/H_2O of the pure H-up and pure H-down bilayers. The implication is that energy is gained by converting an upwardly pointing water into a down pointing water.

Table 4.3: Adsorption energy (E_{ads}) of the H-down overlayer on the hydroxylated (001) surface and cohesive energy (E_{coh}) of ice Ih computed with several exchange-correlation functionals. All values are in units of eV/H_2O.

	PBE	PW91	RPBE	PBE-WC
E_{ads}	-0.65	-0.67	-0.48	-0.73
E_{coh}	-0.66	-0.69	-0.49	-0.77

in Table 4.3 the conclusion that the overlayer is of comparable stability to ice is not altered, with the largest difference between adsorption energy and cohesive energy being only 0.04 eV/H_2O. I have also considered how zero point energy corrections affect the relative stability of the H-down overlayer and ice. It is found that the zero point energy in the overlayer and in the ice Ih model is the same, each being 0.13 eV/H_2O. Thus zero point energy does not alter the conclusion that the H-down overlayer identified here has a stability matching that of ice.

The stable H-down overlayer identified here is fully proton ordered, i.e., all the water molecules of each type (flat and down pointing) adopt the same orientations. In proton disordered structures the water molecules adopt random orientations whilst remaining consistent with the ice rules [92]. To address the question of proton disorder an additional structure in the p(2×2) surface cell (Fig. 4.6c) and two additional structures in a p(3×3) surface cell were calculated. However, the adsorption energies of these proton disordered structures are also -0.65 eV/H_2O. Thus, from this admittedly limited trial of partially proton disordered structures, I concluded that the adsorption energy of the H-down overlayer is not particularly sensitive to the issue of proton order.

4.5.4 Adsorption beyond the 2D overlayer

Having identified a stable 2D overlayer that is of comparable stability to bulk ice, it was then sought to understand how facile subsequent water adsorption would be by examining the adsorption of additional water on top of the H-down (and some other) overlayer(s). Specifically, the adsorption of water monomers and a second complete overlayer on top of the 2/3 ML overlayers were examined.

Several trial structures for water monomers on top of the H-down overlayer, corresponding to a coverage of 3/4 ML, were examined. In these calculations the extra water molecules were either placed at the center of the underlying water hexagon or directly above the flat or down pointing molecules of the overlayer. Upon optimization the most stable structure identified has the extra water molecule located at a bridge-like site. At this site the additional water interrupts the H bond network of the underlying water layer by donating one hydrogen bond to one of the down pointing water molecules and accepting one hydrogen bond from one of the originally flat but now tilted water molecules. The binding energy per water in this overlayer is only marginally less than the stable H-down overlayer (-0.64 eV/H_2O).

Several structures comprised of two complete bilayers were also considered. A total of eleven different double layer structures involving changes of orientation of water in both layers were examined. However, it was found that adsorption of a complete second layer of water on the first layer is energetically unfavorable. All the double bilayer structures are at least $\sim$0.07 eV/H_2O less stable than the single H-down bilayer. Thus after the first 2D ice-like layer wets the surface, the second layer is unfavorable. Another way of saying this is that while the hydroxylated (001) surface is hydrophilic, the water covered kaolinite surface is hydrophobic. It is most likely that this change of water adsorption energy is caused by a combination of at least two factors. First, in the H-down overlayer every water molecule is already involved in four hydrogen bonds and so does not have any dangling OH groups or dangling lone pairs with which additional water molecules could interact. Second, this applies generally to all the double

bilayer structures considered, there is a lattice mismatch between the substrate and ice: A single bilayer is essentially free to compensate for any mismatch by reducing the buckling within the layer, i.e., by compressing. With more than one layer, however, hydrogen bonds must be formed between the layers. This interlayer hydrogen bonding is hampered if the bilayers flatten.

4.5.5 Electronic structure analysis

I now briefly address the electronic structure of the adsorption systems examined, in particular the monomer and H-down overlayer systems. To this end the DOS and how the total electron densities rearrange upon adsorption are considered. The electron density rearrangement, $\Delta\rho$, defined as

$$\Delta\rho = \rho_{nH_2O/slab} - \rho_{slab} - \rho_{nH_2O}, \tag{4.5}$$

where $\rho_{nH_2O/slab}$, ρ_{slab}, and ρ_{nH_2O} are the electron densities of the particular water-kaolinite adsorption system under consideration, the isolated clean (001) kaolinite slab, and the isolated water molecule(s), each in the exact structure they adopt in the adsorption system.

A plot of the electron density difference for the water monomer at the most stable threefold adsorption site is shown in Fig. 4.7a. The nature of the electron density rearrangement displayed in Fig. 4.7a is characteristic of that observed before for hydrogen bonding with depletion of density around the hydrogen atoms involved in each hydrogen bond and an accumulation in density in the region of the oxygen lone pairs [98, 102, 115]. Clearly, when the water monomer sits at this site, three hydrogen bonds are formed, one hydrogen bond it is donating and two it is accepting. From the plot of the electron density difference there is an indication that the hydrogen bond the water monomer is donating is stronger than the two it is accepting due to the greater extent of the charge rearrangement around this bond. This is also consistent with the shorter bond length of this hydrogen bond, 1.73 Å compared to 2.00 Å and 2.03 Å.

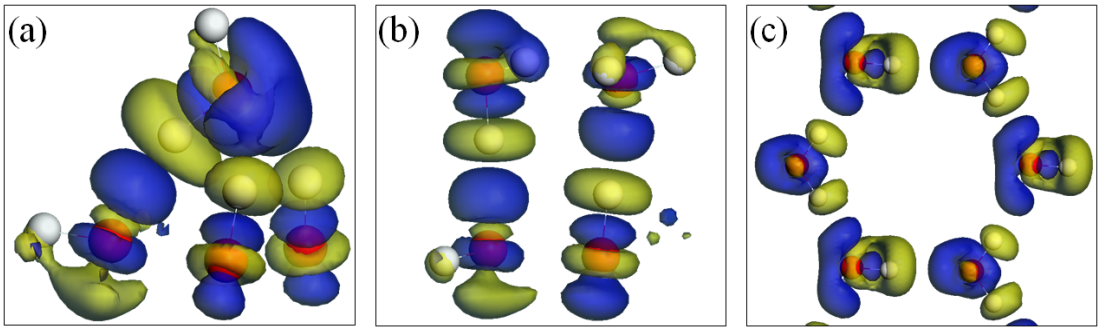

Figure 4.7: Plots of electron density rearrangement for an adsorbed water monomer and water overlayer on kaolinite. Specifically (a) and (b) are side views of how the density around a single water monomer (a) and the H-down overlayer (b) rearrange upon adsorption according to Eq. (4.5). (c) is a top view of how the electron density rearranges within the adsorbed H-down overlayer, according to Eq. (4.6). (a) and (b) are designed to yield information on water-substrate bonding whereas (c) depicts water-water bonding. A constant density isosurface of 0.01 electrons/Å^3 is displayed in all plots. Blue regions indicate positive regions (electron accumulation) and yellow (bright) negative regions (electron depletion).

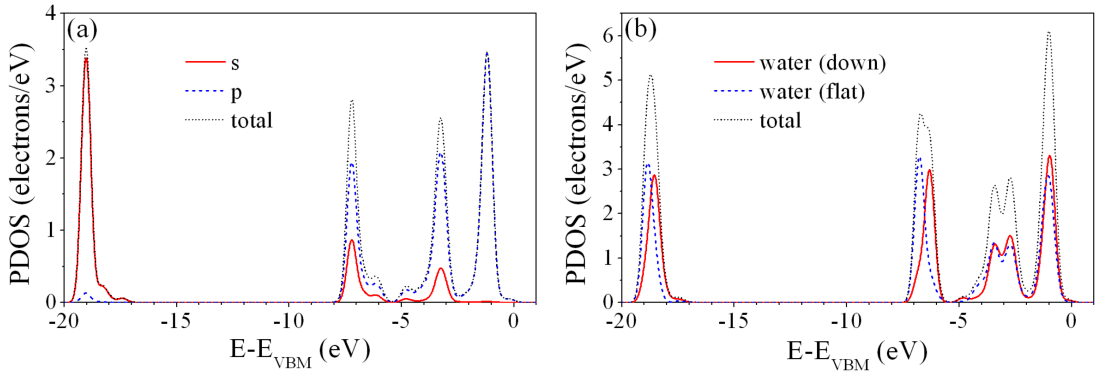

Figure 4.8: PDOS on an adsorbed water monomer (a) and the H-down overlayer (b) on the hydroxylated (001) surface of kaolinite. The energy windows shown depict the four highest occupied Kohn-Sham orbitals (**2a**$_1$, **1b**$_2$, **3a**$_1$, and **1b**$_1$ from left to right) of adsorbed water. E_{VBM} is the energy of the valence band maximum.

Partial DOS plots for the monomer adsorption system are shown in Fig. 4.8a. Specifically, states projected onto the s and p orbitals of the water monomer are displayed. In order of increasing energy these are the $\mathbf{2a}_1$, $\mathbf{1b}_2$, $\mathbf{3a}_1$, and $\mathbf{1b}_1$ states. The splitting between these states is rather similar to what it is for a gas phase water molecule, differing from the gas phase by $<$0.2 eV. Upon inspection of the individual Kohn-Sham eigenstates within each peak only very weak character from the substrate is found, i.e., there is an extremely small amount of electron density mixing of the water molecule with the substrate. In other words I do not see any strong covalent bonding between the molecule and the substrate, but rather the interaction is electrostatic in nature.

Moving to the H-down overlayer, the electron density difference for this system is shown in Fig. 4.8b. The distinct roles the two types of water molecule play in this system are immediately clear: the flat water molecule is accepting a hydrogen bond from the substrate; and the down pointing water molecule donating a hydrogen bond to the substrate. From the extent of the electron density rearrangement around each type of water molecule, it appears that their interaction with the substrate is equally strong. However, as I have said, the mode of interaction between each water molecule and the substrate differs. This can be further seen by examining the water related states in the PDOS plot for the H-down overlayer shown in Fig. 4.8b. Specifically, for the flat water molecule the $\mathbf{2a}_1$ and $\mathbf{1b}_2$ resonances are $\sim$0.3 and $\sim$0.4 eV lower in energy than they are for the down pointing water. Likewise the second closest band to the valence band maximum, $\mathbf{3a}_1$, is split into two states caused by the differing interactions between water molecules within the overlayer and between water molecules and the substrate. As with the water monomer, inspection of the individual Kohn-Sham eigenstates contained within each peak revealed only marginal covalent mixing with the substrate.

It is interesting to ask now what the nature of the interactions between the water molecules within the overlayer are and how these compare to the water-substrate inter-

actions. To facilitate this, a specific type of electron density rearrangement is defined as

$$\Delta\Delta\rho = \rho_{nH_2O/slab} + \rho_{slab} - \rho_{H_2O\_flat/slab} - \rho_{H_2O\_down/slab}, \tag{4.6}$$

where $\rho_{H_2O\_flat/slab}$ and $\rho_{H_2O\_down/slab}$ are the densities of the adsorbed flat and down pointing water molecules in the exact structure they assume in the H-down adsorption system. As before, $\rho_{nH_2O/slab}$ and ρ_{slab} are the electron densities of the adsorption system and the clean substrate, respectively. The density rearrangement defined in Eq. (4.6) is displayed in Fig. 4.7c, revealing exclusively water-water interactions within the H-down overlayer. Again depletion of density on the hydrogen atoms and accumulation around the oxygen lone pairs is observed, characteristic of hydrogen bonding. Comparison of Fig. 4.7b and c indicates that the extent of density rearrangement is similar within the overlayer (Fig. 4.7c) to what it is between the overlayer and the substrate (Fig. 7b).

The plots of electron density rearrangement do not directly show the strength of the various hydrogen bonds in the adsorption system. A better indication of the balance between water-water and water-substrate interactions can be obtained by performing a series of interaction energy decompositions [116]. First, the interaction energy per hydrogen bond between water molecules in the overlayer, $E_{H_2O-H_2O}$, is defined as

$$E_{H_2O-H_2O} = 2/3 \cdot (E_{nH_2O/slab} + E^*_{slab} - E_{H_2O\_flat/slab} - E_{H_2O\_down/slab})/n, \tag{4.7}$$

where E^*_{slab}, $E_{H_2O\_flat/slab}$, and $E_{H_2O\_down/slab}$ are the total energies of the isolated clean (001) kaolinite slab, the flat water molecules in the overlayer adsorbed exclusively on the surface, and the down pointing water molecules adsorbed exclusively on the surface, each in the exact structures they adopt in the H-down overlayer. The factor 2/3 indicates that each of the two water molecules shares three hydrogen bonds in the overlayer. The water-water interaction energy obtained from this decomposition is -0.28 eV/H bond. An analogous energy decomposition designed to reveal exclusively the interaction between a preformed H-down overlayer and the substrate, $E_{H_2O-slab}$, is defined as

$$E_{H_2O-slab} = (E_{nH_2O/slab} - E_{nH_2O} - E^*_{slab})/n, \tag{4.8}$$

where is E_{nH_2O} the total energy of the isolated water overlayer in vacuum fixed in the structure it assumes when adsorbed. This water-substrate interaction energy has a value of -0.32 eV/H bond, which is slightly larger than the hydrogen bond strength between water molecules in the overlayer. Thus, in this adsorption system water molecules appear to bond more effectively with kaolinite than they do with other water molecules. This is also consistent with the computed O-O distances in the adsorption system: The O-O distances between the water molecules within the overlayer are in the interval 2.90-3.06 Å and the O-O distances between the adsorbed water molecules and the substrate are 2.72-2.81 Å.

4.6 Discussion and conclusions

I now summarize the energetics of the various adsorption systems examined here and place the results in the broader context of water adsorption on solid surfaces in general. To facilitate this I plot in Fig. 4.9 the average adsorption energy per water molecule as a function of coverage. There are several interesting features of this plot and the results described in Section 4.5, which I now discuss.

First, at low coverages the water adsorption energy is reasonably constant at $\sim$-0.57 eV/H_2O. This is a rather large value for the DFT-GGA adsorption energy of water on a solid surface: on close-packed metals, for example, water monomer adsorption energies of $\sim$-0.1 to -0.4 eV/H_2O are typically reported [98, 102, 117, 118]; on NaCl values of $\sim$-0.3 to -0.4 eV/H_2O are found [100, 101]; and on metal oxides, such as TiO_2, values of $\sim$-0.40 eV/H_2O have been reported [119–121]. Indeed, the only other report of DFT-GGA adsorption energies for water monomers as large as or larger than the value obtained here are also on hydroxylated surfaces: $\sim$-0.5 to -0.7 eV/H_2O on cristobalite [99] and -0.54 eV/H_2O on α-quartz [122]. Thus it is clear that an important aspect of a strong adsorption bond between water and a substrate is the presence of hydroxyl groups and the possibility of accepting and donating hydrogen bonds to and from them.

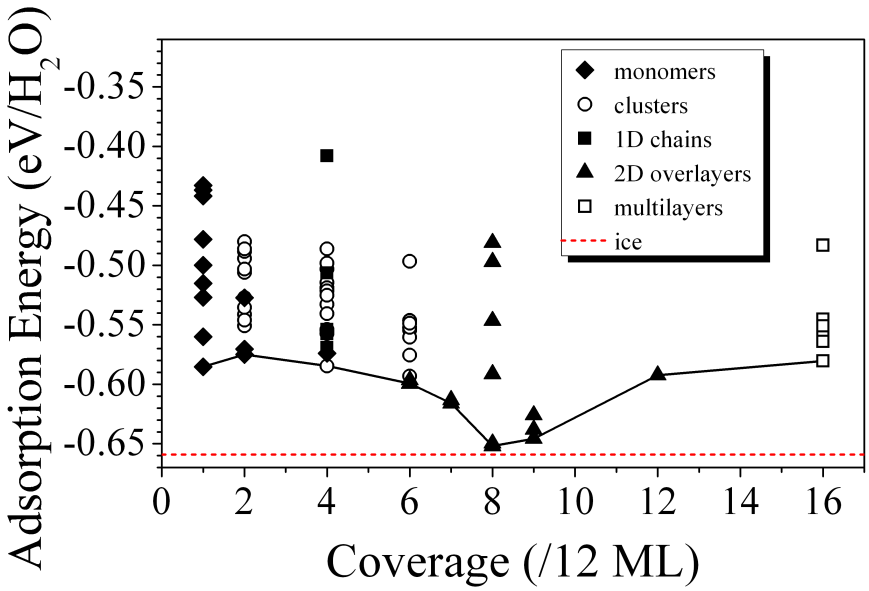

Figure 4.9: Average adsorption energy per water on the hydroxylated (001) surface of kaolinite as a function of coverage. The solid line is a guide to the eye connecting the structure with largest adsorption energy at each coverage considered and the dashed line indicates the cohesive energy of ice Ih.

Second, it is found that water clustering is not favored to any great extent. This was discussed in Section 4.5.2 and can be clearly seen in Fig. 4.9, where points corresponding to dimers, tetramers, and hexamers are equally stable to water monomers at best. Again this behavior is not common for adsorbed water and different from what is observed experimentally and predicted theoretically on metal and some oxide substrates, where clustering is strongly favored [98, 102–106, 123]. On the (111) surfaces of Cu, Pd, Pt, and Ni, for example, DFT calculations predict that water monomers gain 0.1-0.2 eV/H_2O by coming together to form adsorbed dimers. Likewise water molecules on some hydroxylated substrates gain 0.1-0.2 eV/H_2O by dimerisation [99]. Although unusual there are, however, other substrates on which similar behavior has been predicted [101, 122] notably on the hydroxylated α-quartz (0001) surface [122].

Third, the most stable overlayer identified at any coverage is the 2/3 ML H-down over-

layer. As discussed above, this overlayer has a stability similar to that of ice Ih. Again this feature of water on kaolinite differs from the behavior on many other substrates. On the low energy hexagonal surfaces of close-packed metals, for example, both the H-up and H-down overlayers tend to have adsorption energies $\geqslant$0.1 eV/H_2O less than the cohesive energy of ice [9, 116]. Likewise overlayers on other substrates often yield computed adsorption energies that are less than the cohesive energy of ice, such as on NaCl(001) which supports ice-like overlayers with computed adsorption energies of $\sim$-0.46 to $\sim$-0.57 eV/H_2O [100, 101]. The application of different exchange correlation functionals, the inclusion of zero point energies, or proton disorder effects in the adsorption system does not alter the conclusion that the H-down overlayer on kaolinite is almost equally stable to bulk ice. Examination of the atomic and electronic structures in the stable H-down adsorption system provides a clear explanation for the stability of this overlayer. In it each water molecule is fully coordinated with four strong hydrogen bonds. This is made possible by the fact that kaolinite, like water, is amphoteric with the ability to accept and donate hydrogen bonds, which is possible because of the structural flexibility of the surface hydroxyl groups. This flexibility is crucial and allows the hydroxyl groups to tilt to support a stable water overlayer without dangling hydrogen bonds. Should other hydroxylated surfaces not possess such orientationally flexible hydroxyl groups then it is feasible that they may not be able to support such a stable water overlayer as kaolinite does.

Looking again at Fig. 4.9 several points are indicated for structures with slightly lower coverage (1/2 ML and 7/12 ML) and slightly higher coverage (3/4 ML) than that of the H-down overlayer. The latter (3/4 ML) correspond to monomers adsorbed on the H-down overlayer and the former to defective quasi-2D overlayers[7]. All of these structures are less stable than the 2/3 ML H-down overlayer, again pointing to the high stability of this overlayer with its fully coordinated water molecules.

[7]Removing a flat or an upright water molecule from the 2/3 ML H-down overlayer yielded two 7/12 ML structures. Upon optimization these structures had equal stabilities with adsorption energy of $\sim$-0.61 eV/H_2O. Removing two water molecules (a flat and a down pointing water molecule) yielded a 1/2 ML structure. Upon optimization this had an adsorption energy of -0.60 eV/H_2O.

Finally, I have not identified any stable double bilayer structures. All double bilayer structures examined yield adsorption energies at least 0.07 eV/H_2O less than the H-down overlayer, and are thus less stable than ice by a similar amount. Thus although a single stable wetting layer is predicted, subsequent ice growth is not favored. Essentially these results indicate that the surface of the H-down overlayer is hydrophobic. A similar conclusion has recently been made for the H-down bilayer which is thought to form on Pt(111) [124] and the OH-H_2O overlayer which also forms on Pt(111) [125]. Moreover, these results imply that the (001) basal plane of kaolinite does not support epitaxial multilayer ice growth. Thus the role played by kaolinite in heterogeneous ice nucleation is likely to be more complex than previously thought to be [8]. This may involve preferential nucleation at defective or reconstructed surfaces or nucleation on other facets.

Chapter 5

Polar (001) basal plane of kaolinite

Kaolinite is thought to be an efficient ice nucleating agent because kaolinite crystals expose perfect unreconstructed (001) basal surfaces which provide a suitable template for ice growth. However, it is shown here with the aid of DFT calculations that the unreconstructed basal surface is polar. Various mechanisms to eliminate the surface dipole and in so-doing stabilize the basal surface are considered. The most promising option identified so far involves the adsorption of foreign atoms (for example, Na and Cl atoms) on the perfect basal surface, since this yields a non-metallic surface with a cleavage energy lower than the unreconstructed polar basal surface.

5.1 Introduction

Clay minerals are abundant in soil and important to a wide variety of disciplines such as environmental chemistry, astrophysics, geology, and the ceramics industry. However, our understanding of the crystal structures of clay mineral surfaces is still far from complete at the atomic level, and lags behind the existing knowledge about other simpler oxide or semiconductor surfaces. Nonetheless it is necessary to understand the properties of clay mineral surfaces, especially their cleavage surfaces, because of the central role they play in catalyzing different physical and chemical phenomena. For

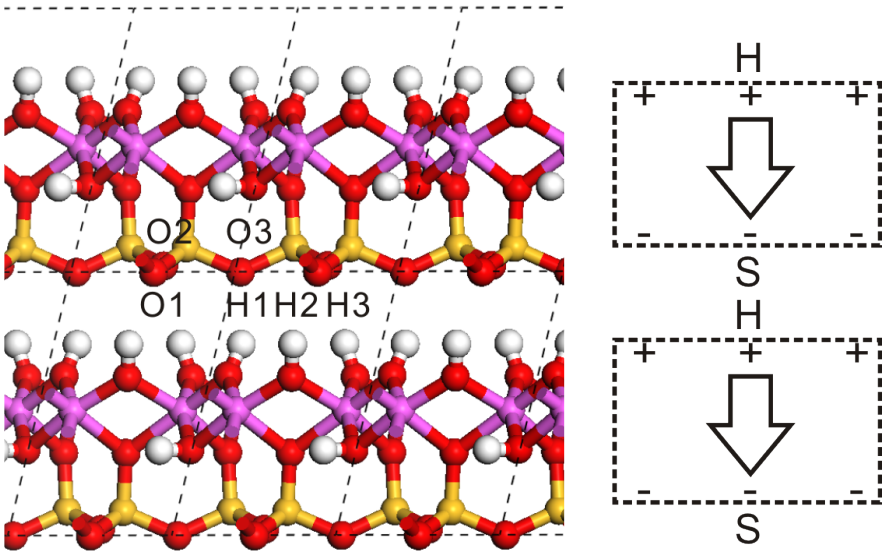

Figure 5.1: The structure of kaolinite bulk (left) and a schematic illustration of the classical electrostatic dipole moment within an individual layer of kaolinite (right). In the figure on the left two layers of kaolinite are shown. The dashed lines on the left indicate the primitive unit cell. As before, white, red, purple, and yellow spheres represent hydrogen, oxygen, aluminium, and silicon atoms, respectively. Certain oxygen and hydrogen atoms discussed in the text are indicated.

example, the clay mineral kaolinite ($Al_2Si_2O_5(OH)_4$), an aluminosilicate as I have presented in last chapter, is an effective heterogeneous ice nucleating agent and important in regulating other chemical and physical processes in the troposphere [8].

Due to the complex structure of layered kaolinite, I introduce here its structure again. As shown in Fig. 5.1, kaolinite is a 1:1 layered aluminosilicate with each layer comprised of an octahedrally coordinated aluminate-terminated sublayer connected to a tetrahedrally coordinated siloxane-terminated sublayer. The oxygen atoms bonded exclusively to aluminium atoms exist as hydroxyl groups. Most of the hydroxyl groups are located on the aluminate-terminated (001) surface and hold adjacent layers together through hydrogen bonds. The (001) surface - the basal surface - is the cleavage plane of kaolinite as well as the main exposed surface of kaolinite crystals [96, 97]. The adsorption of a wide variety of atoms and molecules on the kaolinite basal surface has

been examined, with water adsorption a particular focus because of the relevance of kaolinite to ice nucleation [8, 83, 84, 126–130]. In previous theoretical studies (including the water and ice adsorption studies on kaolinite in chapter 4), "perfect" layers of kaolinite have been used to model adsorption on the (001) surface [83, 84, 128–130]. However, it is pointed out here that this practice may have some limitations because the clean unreconstructed (001) basal surface of kaolinite is polar. This can be simply inferred from its structure (Fig. 5.1), where it can be seen that each individual layer of kaolinite carries a dipole. Since on classical electrostatic grounds the electrostatic contribution should diverge and polar surfaces should not exist, the assumption that kaolinite crystals expose perfect unreconstructed basal surfaces must be questioned. With this in mind DFT is used to investigate the electronic and geometric structure of the kaolinite basal surface. The calculations reveal that the perfect clean (001) basal surface is indeed polar, although beyond a critical thickness electron density redistribution, leading to surface metallization, greatly reduces the macroscopic dipole perpendicular to the surface and in so-doing reduces the cleavage energy (E_{cleave}). Of the many alternative basal plane terminations considered those involving foreign atoms, e.g. Na and Cl, on the perfect basal surface are the most promising since they yield non-metallic surfaces with low E_{cleave}. Thus in nature the surfaces of kaolinite crystals may always be "dirty" and stabilized by adsorbates. This is likely to have implications for ice nucleation on kaolinite and I hope that this brief account will prompt further theoretical and experimental work into determining the detailed surface structure of the kaolinite basal surface. For example, the use of scanning tunneling microscopy or molecular dynamics combined with the simulated annealing technique, that has been successfully applied to other polar surface reconstruction, may prove useful for this system too [131–133]. Indeed, the issues discussed herein are likely to be of relevance to all layered 1:1 aluminosilicates, which also possess polar basal surfaces.

5.2 Computational details

The DFT calculations reported in this chapter have been performed with the plane wave pseudopotential supercell approach, as implemented in the VASP code [37, 38]. PAW potentials [68, 69] with a plane wave cutoff of 400 eV have been used[1]. The GGA-PBE [50, 51] exchange-correlatoin functional has been employed throughout. A variety of bulk and surface unit cells have been employed, as detailed below. In all cases Monkhorst-Pack ***k*** point meshes [66] equivalent to 4×4×3 (4×4×1) corresponding to 24 (8) ***k*** points per bulk (surface) primitive cell - from the conventional cell reported by Bish [81] - were used. There is a vacuum region between slabs for all surface calculations of about 15 Å. During structure optimizations all atoms are fully relaxed until the forces are reduced below 2×10^{-2} eV/Å. For the surface calculations the dipole across the slab has been corrected with the scheme introduced by Neugebauer and Scheffler and implemented in VASP [134, 135]. For any unit cell in which there was an odd number of electrons spin polarized calculations were performed.

5.3 Polar basal surface

5.3.1 Perfect surface structures

In the studies of kaolinite E_{cleave} is used as the main measure of the stability of the slabs examined. For stoichiometric chemically unmodified surfaces, it can be obtained from the following relation:

$$E_{cleave} = (E_{slab} - n \cdot E_{bulk})/(2 \cdot A), \tag{5.1}$$

where E_{slab} is the total energy of a multilayer slab of kaolinite, n the number of layers in the slab, and E_{bulk} is the total energy of a single kaolinite layer in bulk. The factor 2 in the denominator accounts for the fact that there are two outer surfaces on each slab.

[1] A plane wave cutoff of 600 eV yields a cleavage energy within 1 meV/Å^2 of that obtained at 400 eV.

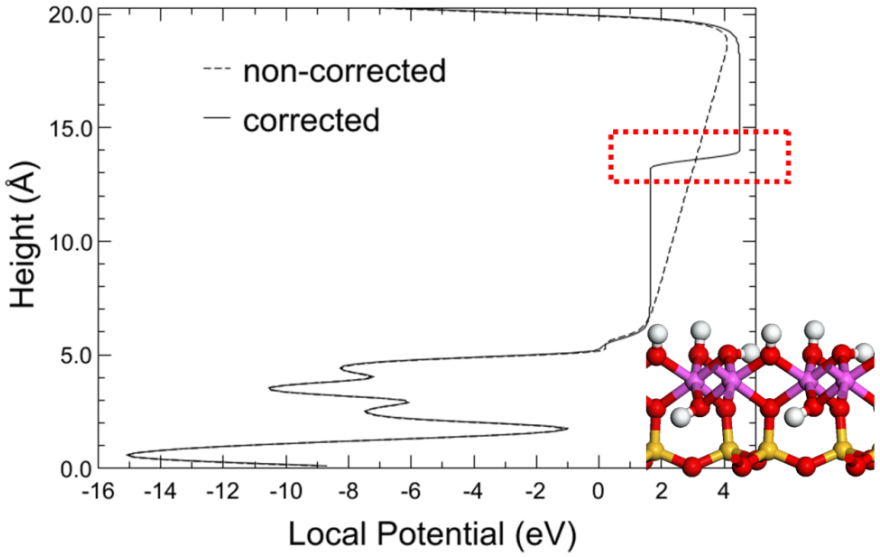

Figure 5.2: Local potential in the [001] direction of a single layer of kaolinite in vacuum. The structure of the layer and its location within the simulation cell is given in the inset. The black dashed and solid lines show the local potential before and after the application of an external electrostatic dipole correction. The dashed red region indicates the location of the artificial dipole correction and highlights the local potential difference between the two (001) surfaces.

E_{cleave} is therefore the average surface energy of both (001) surfaces. The area of each surface is A.

First I consider a single layer of kaolinite. Because of the different chemical composition on either side of the layer, the electronic charge distributions differ and there is a non-zero dipole moment across it. The dipole moment can be inferred from Fig. 5.1, or more precisely, obtained from the DFT calculations by inspection of the local potential difference across the layer. This is shown in Fig. 5.2, where it can be seen that the local potentials of the hydroxyl- and siloxane-terminated surfaces differ. In the used periodic supercell this leads to a steady drop across the vacuum region with the slope in the potential across the vacuum being a signature of the dipole within the kaolinite layer. In the supercell calculations the slope across the vacuum will lead to a spurious interaction between adjacent periodic images, and so it is compensated

through the application of an external electrostatic field in the vacuum [134]. The corrected potential is shown by the solid line in Fig. 5.2. The application of the external potential also allows for a better estimate of the local potential difference within the layer to be obtained. Specifically the local potential at the siloxane-terminated surface is $\sim$2.8 eV higher than that at the hydroxyl-terminated surface. E_{cleave} for the single layer is 8 meV/Å^2 with the current computational setup, essentially the same as the value reported in Section 4.4 of the last chapter. This is a low value for E_{cleave} but reasonable because creation of the surface only involves the cleavage of interlayer hydrogen bonds. It is, for example, similar to the PBE surface energy of ice [136]. The structure of a single isolated layer of kaolinite resembles closely a layer of kaolinite in bulk. The only noteworthy difference is that when the basal surface is exposed to vacuum 1/3 of the surface hydroxyl groups on the (001) surface tilt and become almost parallel to the (001) surface (*c.f.* Fig. 5.1 and 5.2).

Consider now a stack of individual kaolinite layers that make a slab. Just as with a single layer, the entire slab carries a dipole perpendicular to the surface, and according to Tasker's classification[2] of crystal surfaces [137] can be considered as a polar surface (type III). From classical electrostatics, two different surfaces with opposite charge can be treated as a capacitor. The total dipole moment and E_{cleave} of the entire multilayer slab are within classical electrostatic picture proportional to the number of capacitors in the slab. Thus, E_{cleave} and the dipole moment of the slab will diverge as it approaches a macroscopic thickness. It is well known that the classical electrostatic theory just described is oversimplified and ignores the redistribution of the electron density during the process of cleavage and growth of a surface. Indeed it has often

[2]According to classical electrostatic grounds, the stability of a specific crystal surface depends on the characteristics of the charge distribution in the structural unit which repeats itself in the direction perpendicular to the surface. Thus, Tasker classified surfaces of any ionic or partly ionic crystal into three types: type I, neutral surfaces with stoichiometric proportions of anions and cations in each plane of the repeated unit; type II, charged surfaces with no dipole moment in the repeated unit perpendicular to the surface; and type III, charged surfaces that have a dipole moment in the repeated unit perpendicular to the surface.

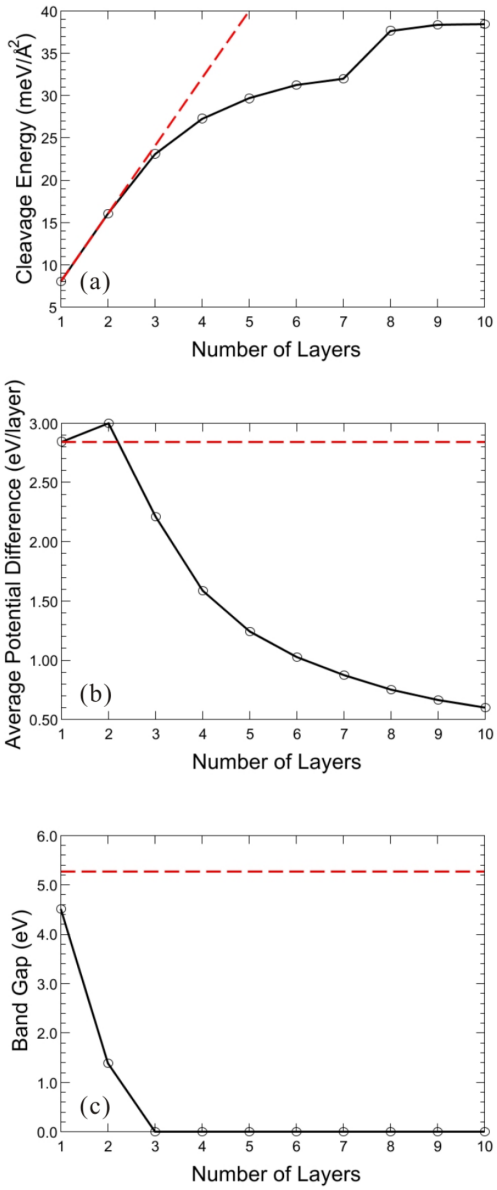

Figure 5.3: (a) Plot of the DFT-PBE E_{cleave} for the (001) surface as a function of the number of layers of kaolinite. The dashed line shows the linear increase of E_{cleave} according to the oversimplified classical theory. (b) Average DFT-PBE potential difference per layer between the two different (001) surfaces of the kaolinite slab as a function of the number of layers in the slab. The dashed line shows the value of a single layer of kaolinite as a reference. (c) Estimated DFT-PBE band gap of the kaolinite slab as a function of the number of layers in the slab. The dashed line shows the DFT-PBE band gap of bulk kaolinite.

been suggested that polar surfaces can compensate the macroscopic dipole moment by electronic charge redistributions [138–141]. Concerning the electronic structure redistribution contribution to the energy of the finite kaolinite slab, the DFT calculations of E_{cleave} as a function of the number of layers of kaolinite in a 2D slab are shown in Fig. 5.3a. It can be seen that the computed DFT values for E_{cleave} deviate significantly from the classical prediction of a linear relation between E_{cleave} and the slab thickness. Indeed E_{cleave} is considerably reduced beneath the linear regime and for the relatively thin slabs considered (up to ten layers) remains rather small ($<$40 meV/Å^3). However, as I will discuss below, the jump between seven and eight layers leads it to be suggested that E_{cleave} will not actually converge to a finite value for thicker slabs.

How does the electron density rearrange to compensate the partial macroscopic dipole moment? Analysis of the DFT Kohn-Sham band gap, DOS, and PDOS over each layer provides the answer. In Fig. 5.3b the average local potential differences per layer between the siloxane- and hydroxyl-terminated surfaces in the kaolinite slab versus the number of layers are plotted. It can be seen that as the slab gets thicker the average potential difference drops. For the thickest ten layer slab considered it is only 0.6 eV/layer compared to 2.8 eV for the isolated layer of kaolinite. In Fig. 5.3c the computed band gaps of the bulk and surface slabs are shown. It can be seen that the DFT-PBE Kohn-Sham band gap is large, at least 4 eV for both kaolinite bulk and a single layer of kaolinite in vacuum. Upon detailed inspection of the electronic structures of bulk kaolinite and an isolated layer of kaolinite it is found that they have similar electronic structures. However, if I consider multilayer slabs, it is found that the DOS and related band gap (Fig. 5.3c) depend sensitively on the thickness of the slab, and as the slabs get thicker the band gap gets smaller. This is clearly shown in Fig. 5.3c where it can be seen that already with a three layer slab the band gap has reduced to zero. This modification of the band gap seen many times before in self-consistent electronic structure calculations is usually referred to as "metallization of the polar surface" [138, 141, 142]. The explicit explanation for the metallization can be found in Figs. 5.4a and b where the PDOS of each individual layer within a three layer kaolinite

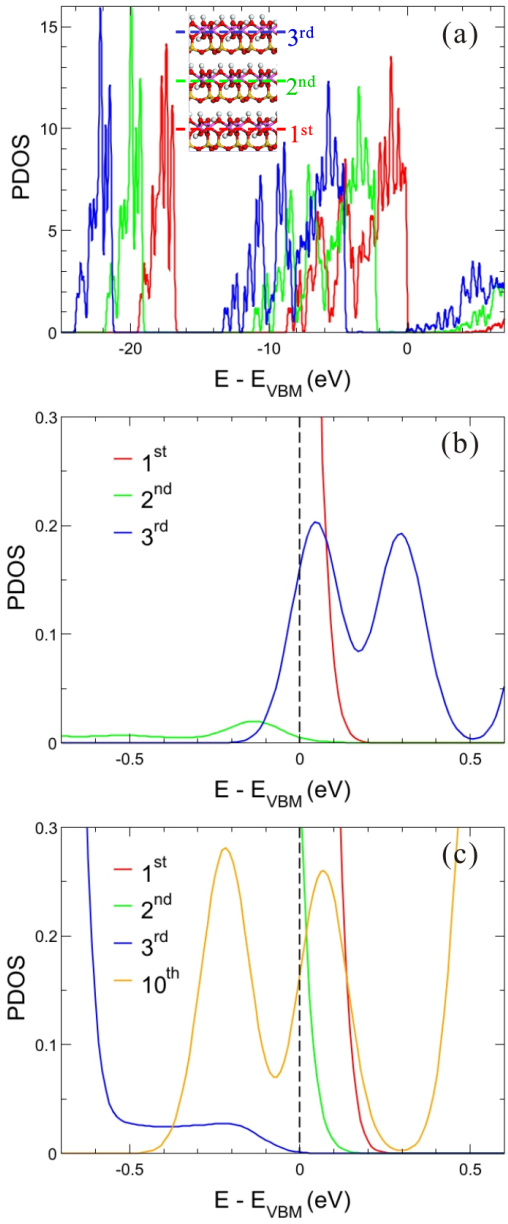

Figure 5.4: (a) DFT-PBE projected density of states (PDOS) of each individual layer in a three layer kaolinite slab. The energy zero, E_{VBM}, is the energy of the valence band maximum. A side view of the structure of the three layer slab is shown in the inset, with each of the layers (1^{st}, 2^{nd}, and 3^{rd}) indicated. (b) A zoom in of the PDOS shown in (a) focusing on the region around E_{VBM}. This PDOS makes the small charge transfer from the siloxane-terminated first layer to the hydroxyl-terminated third layer more apparent. (c) PDOS around E_{VBM} for a ten layer kaolinite slab, indicating that charge is now transferred from the first two layers on the siloxane-terminated side of the slab to the (10^{th} layer) hydroxyl-terminated side of the slab.

slab is plotted. The densities of states of each individual kaolinite layer are displaced by $\sim$2 eV with respect to each other, with the states on the hydroxyl-terminated side of the slab (3^{rd} layer) lowest in energy and those at the siloxane-terminated side of the slab (1^{st} layer) highest in energy. This splitting leads to a small amount of overlap between the valence band of the first layer and the conduction band of the third layer, which in turn leads electron density to be transferred from the first to the third layer (Fig. 5.4b). With the closing of the band gap and the ensuing electron transfer the dipole moment across the slab and hence E_{cleave} are greatly reduced compared to the simple electrostatic model shown in Fig. 5.3a. The DOS and PDOS plots for all other thicker multilayer kaolinite slabs exhibit similar metallization. I have not been able to find reports of the experimental optical band gap of kaolinite. However it is anticipated that the Kohn-Sham band gap obtained here is underestimated compared to the experimental gap. With a larger band gap, the critical thickness for the onset of the surface metallization is likely to be larger than the three layers identified here.

Surface metallization compensates the surface dipole and has been shown to lead to a finite E_{cleave} that converges with respect to the number of layers in the slab in other materials [140, 142, 143]. Indeed for kaolinite E_{cleave} up to seven layers appears to be steadily converging. However the jump between seven and eight layers points to a subtlety in kaolinite that arises because of its layered structure. Specifically a PDOS analysis reveals that upon going from seven to eight layers electron density is not only transferred from the outermost siloxane-terminated layer to the outermost hydroxyl-terminated layer but also from the subsurface layer on the siloxane-terminated side of the slab. This is shown, for example, by the PDOS plot for a ten layer slab in Fig. 5.4c where there is a small amount of overlap between the valence bands of the first and second layers and the conduction band of the tenth. Because of difficulties in converging the electronic structure I have not been able to investigate slabs thicker than ten layers. However it is expected that discrete jumps in E_{cleave} will be observed each time electron transfer from a new subsurface layer kicks in. Thus it is unlikely that surface metallization is an effective means to yield a converged finite value of E_{cleave}

Table 5.1: Cleavage energies of selected kaolinite (0 0 1) surfaces examined. The details of the structures are discussed in the text and figures. The number of kaolinite layers in each slab is also given in parenthesis. Note that only values in bold can be considered as converged with respect to slab thickness. Other values for surfaces that remain polar are not converged and are shown for reference only.

Model	E_{cleave} (meV/Å^2)
(001) (10)	37
(001)-H_2O-removed (3-5)	**211**
(001)-H_2-removed (3-5)	**152**
(001)-k-g-k (6)	40
(001)-k-p-k (6)	50
(001)-k-k (10)	51
Water covered (001) (10)	8
Hydroxylated (001)-Cl-adsorption (3-5)	**26**
Siloxane (001)-Na-adsorption (3-5)	**5**

for kaolinite.

5.3.2 Defective surface structures

There are of course other mechanisms apart from surface metallization for compensating the surface dipole, such as a change in chemical composition at the surface, surface reconstruction or adsorption of foreign atoms or molecules. An extensive series of calculations involving each of these possibilities have been performed and now I briefly summarize some of the key results. The cleavage energies for the surface structures discussed below are given in Table 5.1.

First, changes to the stoichiometry of the (001) surface of kaolinite through the re-

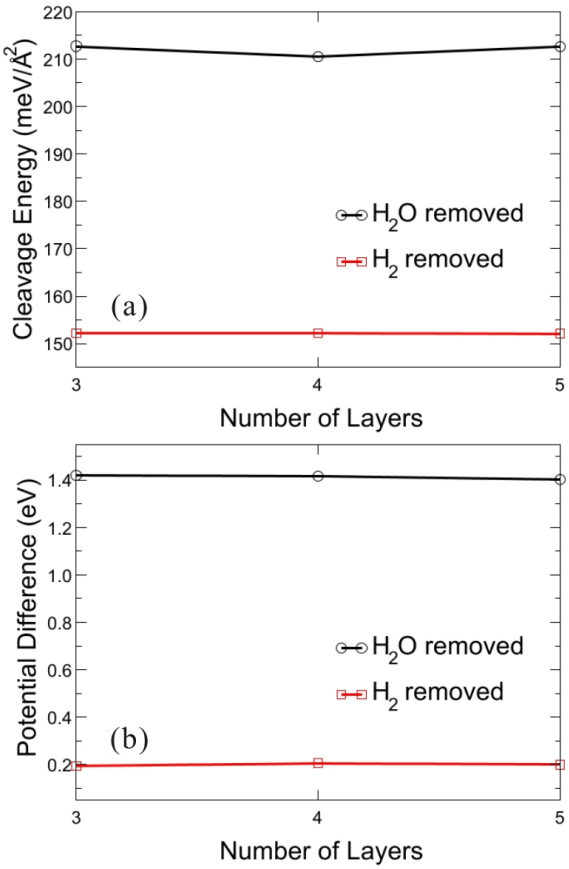

Figure 5.5: (a) Plot of DFT-PBE E_{cleave} as a function of the number of layers of kaolinite in two defective kaolinite slabs. In one, labeled "H_2O removed", two hydrogen atoms (H2 and H3 in Fig. 5.1) of the outermost hydroxyl-terminated surface and one oxygen atom (O2 in Fig. 5.1) of the outermost siloxane-terminated surface have been removed from the perfect kaolinite structure in each primitive surface cell. In the other defective structure, labeled "H_2 removed", two hydrogen atoms (H2 and H3 in Fig. 5.1) of the outermost hydroxyl-terminated surface have been removed. (b) DFT-PBE (absolute) potential difference between the two outermost (001) surfaces for the same two defective structures as a function of the number of layers in the slab.

moval of oxygen and hydrogen atoms are discussed. A large variety of oxygen and hydrogen deficient surfaces were examined. I just discuss two out of the many structures considered, specifically those which resulted in significant reductions in the surface dipole. To compare the energies of the various surfaces, I now use the relation:

$$E_{cleave} = (E_{slab} + m \cdot E_{molecule} - n \cdot E_{bulk})/(2 \cdot A), \tag{5.2}$$

where E_{slab} is the total energy of the defective multilayer kaolinite slab, $E_{molecule}$ is the total energy of the most stable molecular form of removed atoms in the gas phase (either H_2O or H_2), m is the number of the molecular formula units removed from the unit cell, and E_{bulk}, n, and A are as defined in (5.1). In the first structure discussed a H_2O formula unit is removed. This involves the removal of 2/3 of the hydrogen atoms from the surface hydroxyl groups on the outermost hydroxyl-terminated (001) surface and 1/3 of the oxygen atoms from the outermost siloxane-terminated (001) surface. Specifically, H2, H3 and O2 as labeled in Fig. 5.1 are removed from each unit cell. Except for the two outermost layers, the other layers in the slab retain the stoichiometry of perfect kaolinite. Fig. 5.5 shows E_{cleave} and the local potential difference as a function of the number of kaolinite layers in the slab with the defective (001) surfaces. It can be seen that E_{cleave} and the total potential difference between the two outermost terminations of this slab stay at around 211 meV/Å^2 and 1.4 eV, respectively, as the number of kaolinite layers increases from three to five. Therefore, contrary to the perfect kaolinite surface, E_{cleave} of this surface is rather insensitive to the number of layers in the slab. However, the absolute value of E_{cleave} at $>$200 meV/Å^2 is very large and therefore I conclude that this does not represent a plausible alternative surface structure. A similar picture emerges for another low dipole surface created when a H_2 formula unit is removed. Specifically, 2/3 of the hydrogen atoms (H2 and H3) on the outermost hydroxyl-terminated (001) surface are removed. E_{cleave} and the total potential difference across the slab versus the number of layers in the slab is also shown in Fig. 5.5. For this surface the local potential difference is as small as 0.2 eV, i.e., the macroscopic dipole moment is almost completely eliminated by the creation of the

defective structure[3]. However, E_{cleave} of this structure, with a value of 152 meV/Å^2, is very large and again does not represent a plausible alternative surface structure. The defect concentrations for the two defective surfaces just discussed are very high (2/3 of the hydrogen atoms of the surface hydroxyls are removed). Many structures with lower defect concentrations were considered. For brevity I do not discuss them because they failed to eliminate the surface dipole and/or yielded large values of E_{cleave}. The high cleavage energies of the exemplar oxygen and hydrogen deficient surfaces just discussed simply reflect the fact that strong covalent bonds in the silica or alumina frameworks must be broken to form defects.

5.3.3 Mixed mineral structures

The second strategy I have considered to cancel the macroscopic dipole moment at the polar kaolinite basal surface is through the mixed growth of clay minerals. Mixed mineral structures are worth considering because layered aluminosilicates naturally contain impurity layers of other clays [97, 144]. Specifically, natural kaolinite samples contain charged and uncharged 2:1 layered clay minerals [145]. A host of mixed mineral structures has been considered. The most interesting ones, which entirely eliminate the macroscopic dipole, are a series of "sandwich" structures. These are comprised of an impurity layered mineral (e.g. pyrophyllite or gibbsite) placed in the centre of an even number of kaolinite layers. The kaolinite layers were arranged to have exclusively their siloxane- or hydroxyl-terminated surfaces directed towards the impurity layer so that simply by symmetry there was no dipole perpendicular to the surface. An example of a gibbsite layer sandwiched between two layers of kaolinite, each with their siloxane-terminated surfaces exposed to the vacuum is shown in Fig. 5.6a, and an equivalent structure but with a pyrophyllite central layer is shown in Fig. 5.6b. The definition of E_{cleave} for these structures is

$$E_{cleave} = (E_{slab} - n \cdot E_{bulk} - E_{center-bulk})/(2 \cdot A), \tag{5.3}$$

[3]These two defective structure are non-metallic, with DFT-PBE band gaps within 0.5 and 2.2 eV of bulk kaolinite for the H_2 and H_2O removed defective structures, respectively.

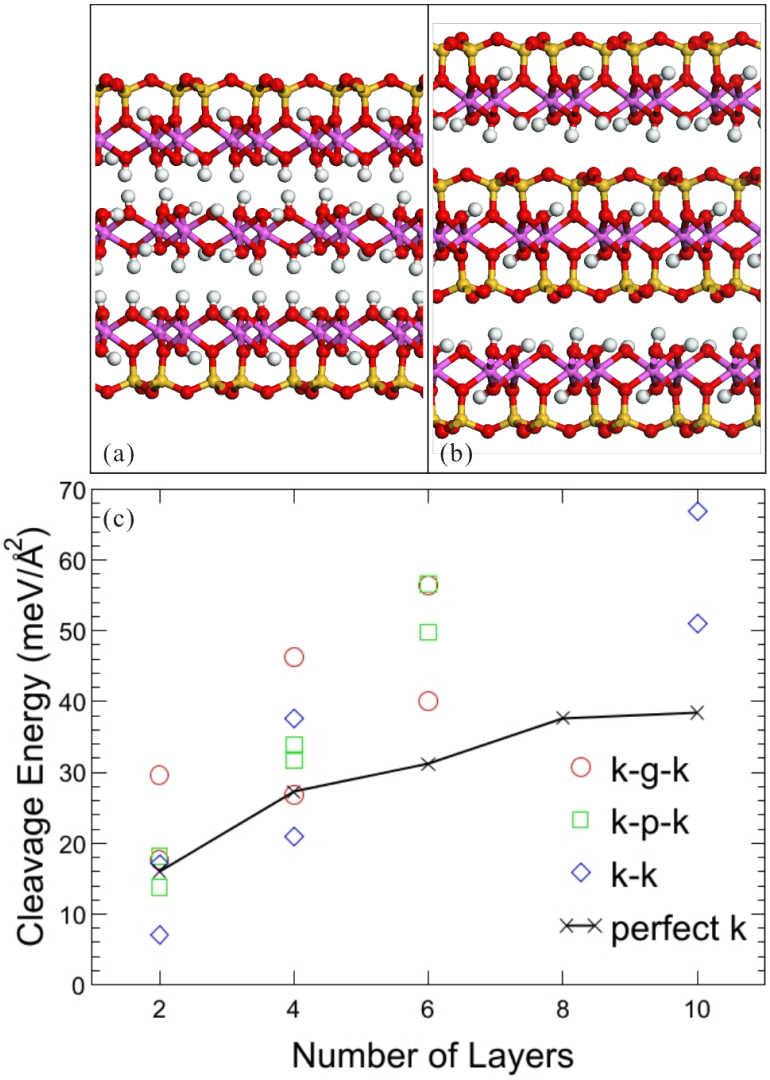

Figure 5.6: Side views of some of the trial mixed clay mineral structures considered and a plot of the DFT-PBE cleavage energies of different mixed minerals as a function of the number of layers of kaolinite. K-g-k indicates the kaolinite-gibbsite-kaolinite sandwich structure (a), k-p-k the kaolinite-pyrophyllite-kaolinite sandwich structure (b), and k-k is the "upside-down" kaolinite structure. For each class of structure the siloxane-terminated surfaces and hydroxyl-terminated surfaces exposed to vacuum were considered, only siloxane-terminated structures are shown here in (a) and (b). However, in (c), cleavage energies for both the hydroxyl-terminated and the siloxane-terminated structures are reported. In every case the siloxane-terminated slabs are 2-20 meV/Å^2 more stable than the hydroxyl-terminated slabs. As a reference, the solid line indicates the calculated values of E_{cleave} for perfect kaolinite slabs.

where $E_{center-bulk}$ is the total energy of a single layer of gibbsite or pyrophyllite in bulk. These bulk reference energies for gibbsite and pyrophyllite are obtained from separate bulk calculations using the experimental lattice constants [146, 147] for these materials. Since the in-plane lattice mismatch between kaolinite, gibbsite, and pyrophyllite is small ($\lesssim$2%), on the calculations, the kaolinite surface cell is used throughout and all atoms are allowed to relax within it. The cleavage energies of the two specific sandwich structures shown in Figs. 5.6a and b are 18 meV/Å^2 and 14 meV/Å^2, respectively. These structures contain two layers of kaolinite and have similar cleavage energies to a two layer kaolinite slab (16 meV/Å^2 in Fig. 5.6c). Therefore, these look like promising structures. However, when the thickness of these sandwich structures is increased by adding more layers of kaolinite on either side of the impurity layer, it is found that they have similar stabilities to the perfect polar kaolinite slab (Fig. 5.6c) and also become metallic. I note that these conclusions are not changed even if fully relaxed lattice constants for $E_{center-bulk}$ are used. Specifically, the surface metallization still appears and the cleavage energies are all within 3 meV/Å^2 of those shown in Fig. 5.6. Although the total slab does not carry a dipole, the individual stacks of kaolinite layers on each side of the impurity layer do, i.e., there are two dipoles directed at each other which cancel. A similar scenario applies to zero dipole "upside-down" structures of kaolinite that were considered. These structures stack together with an inverse symmetry, i.e., half of the kaolinite layers stand upwards and the other half downwards, similar to the structures shown in Figs. 5.6a and b but without the impurity minerals in the middle. Consequently, pure upside-down kaolinite slabs are no more stable than the regular polar kaolinite slab (Fig. 5.6c) and again become metallic.

5.3.4 Foreign atom or molecule adsorbed structures

Various adsorbates on the perfect (001) surface were considered as another means to compensate the surface dipole. These included H, O, and Cl atoms, metal atoms, and water. The definition of E_{cleave} used for these structures is

$$E_{cleave} = (E_{slab} - n \cdot E_{bulk} - m \cdot E_{molecule})/(2 \cdot A), \tag{5.4}$$

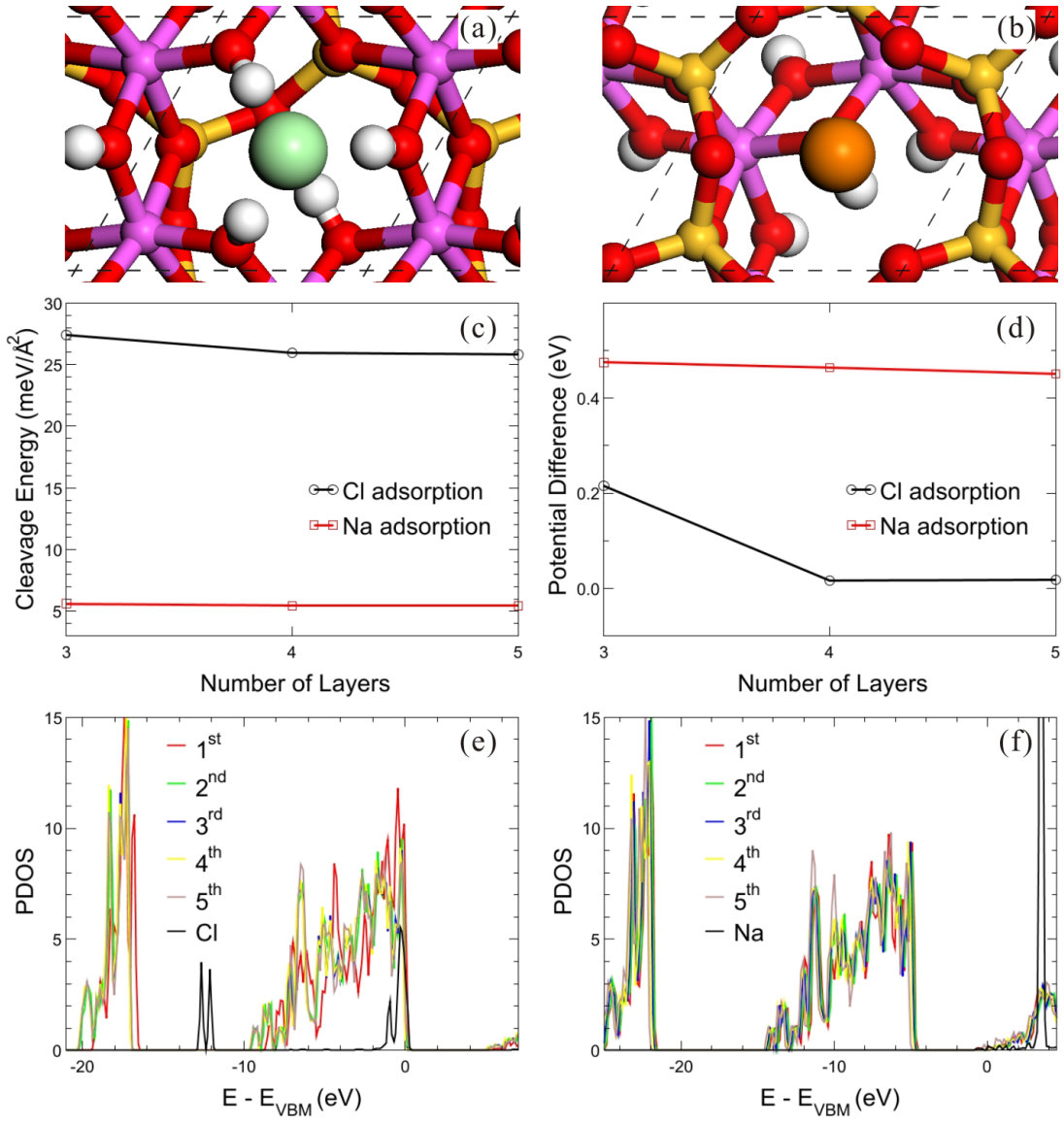

Figure 5.7: (a) Top view of kaolinite with Cl adsorbed on the outermost hydroxyl-terminated surface (only the outermost layer is shown). (b) Top view of kaolinite with Na adsorbed on the outermost siloxane-terminated surface (only the outermost layer is shown). (c) Plot of DFT-PBE E_{cleave} as a function of the number of layers of kaolinite for kaolinite slabs with Cl adsorbed on the outermost hydroxyl-terminated surface or Na adsorbed on the outermost siloxane-terminated surface. (d) DFT-PBE absolute potential difference between the two outermost (001) surfaces for the same two adsorption structures as a function of the number of layers in the slab. (e) DFT-PBE PDOS of each individual layer and of the adsorbed Cl atom for the five layer Cl/kaolinite adsorption system. (f) DFT-PBE PDOS of each individual layer and of the adsorbed Na atom for the five layer Na/kaolinite adsorption system.

where all terms are as defined as before in this chapter. The first adsorbate discussed is water, specifically a complete 2/3 ML ice-like water overlayer - the H-down bilayer discussed in Subsection 4.5.3 of the last chapter. The adsorption energy of the H-down overlayer is -658 meV/H_2O with the current computational setup and does not vary with the thickness of the slab. From Eq. (5.4) this yields a E_{cleave} for a ten layer kaolinite slab of 8 meV/Å[24]. However, the local potential difference across this surface is still large (for example, 2 eV/layer for a three layer slab) and, moreover, the DOS reveals that this surface also undergoes metallization, that is the adsorption of water does not eliminate the dipole moment across the kaolinite slab.

Of all the options considered to yield a stable kaolinite surface the most promising candidates correspond to the adsorption of Cl or Na atoms on the outermost surfaces of perfect kaolinite slabs. In the Cl adsorption structure, one Cl atom in each primitive surface cell (half of the Cl_2 formula unit) is adsorbed at a hollow site of the outermost hydroxyl-terminated (001) surface as shown in Fig. 5.7a. In this hollow site, three surface hydroxyl groups are directed at the Cl adatom. The perpendicular distance of the Cl above the three hydrogens from the hydroxyl groups is $\sim$1.8 Å. Overall the structure of the kaolinite slab is not significantly changed compared to a bare kaolinite surface except that the subsurface hydroxyl groups adopt their upright bulk orientation. In the Na adsorption structure, one Na atom in each primitive surface cell (half of the Na_2 formula unit) is adsorbed at a hollow site on the outermost siloxane-terminated (001) surface as shown in Fig. 5.7b. The Na atom resides $\sim$1.5 Å outside the surface oxygen layer. Again the structure of the kaolinite surface is very similar to that of the bare surface. E_{cleave} and the local potential difference of the two candidate structures as a function of the number of kaolinite layers in the slab are shown in Figs. 5.7c and d. It can be seen that the cleavage energies of the two structures are rather small and insensitive to the number of layers, with values of around 26 and 5 meV/Å^2 for Cl atom and

[4]Since the adsorption energy does not vary with the thickness of the slab, there is a constant difference (28.6 meV/Å^2) between E_{cleave} for perfect kaolinite and the water covered (001) surface. E_{cleave} for the water covered ten layer kaolinite slab was obtained by adding this difference to the clean surface E_{cleave}.

Na atom adsorption, respectively. The local potential differences across the two slabs are also rather small at 0.5 eV or less for slabs of up to five layers thickness. Contrary to the clean unreconstructed (001) basal surface and other trial structures considered, the Cl and Na adsorption structures stabilize the slab and eliminate the macroscopic dipole moment almost entirely. What do the electronic structures of these adsorption system look like? To answer this, PDOS plots for the two adsorbates on a five layer kaolinite slab are plotted in Figs. 5.7e and f. It can be seen that in each case the surface metallization disappears and the PDOS of each individual layer within the kaolinite slab overlaps again. For the Cl adsorption structure, there is a band gap of 5 eV. In the Cl atom adsorption system electron density on the hydroxyl-terminated (001) surface transfers to the Cl atom and in the Na atom adsorption system the electron on the Na atom partially transfers to the siloxane-terminated (001) surface. A Bader charge analysis [148] indicates that Cl carries a negative charge of 0.34 and Na a positive charge of 0.56. Both scenarios eliminate the surface dipole and remove the need for charge transfer which would lead to surface metallization within the kaolinite slab. It has been checked that this conclusion does not change if a hybrid exchange-correlation functional such as PBE0 [56, 59] is used. Indeed the only significant difference between the Cl/kaolinite (Na/kaolinite) PDOS obtained from PBE and PBE0 is the larger band gap of the latter ($\sim$1 eV larger). A lower coverage of adsorbates has also been considered, for example, one Cl atom per conventional surface cell (half the coverage of that shown in Fig. 5.7a). This lower coverage also compensates the surface dipole and leads to a converged E_{cleave} of $\sim$16 meV/Å^2. Thus, overall it is found that suitable foreign atom adsorption on either side of the polar (001) basal plane of kaolinite yields a low E_{cleave}. The main reasons for this are: (i) the electronic structure rearrangements - involving only the adsorbate and the related (001) surface - act to compensate the macroscopic surface dipole; and (ii) the formation of the perfect kaolinite surface does not break any covalent bonds, rather only relatively weak hydrogen bonds.

5.4 Conclusions

In conclusion, I have presented the results of DFT calculations that show that the kaolinite basal surface is polar. Indeed this can simply be inferred from its structure, a fact that has nonetheless not dispelled the assumption that kaolinite crystals undergo perfect cleavage along their basal plane and that kaolinite crystals predominately expose unreconstructed (001) basal surfaces [96, 97]. A selection of the possible mechanisms considered to eliminate the surface dipole has been discussed, with the most compelling scenario involving the adsorption of foreign atoms on the perfect basal surface. Hopefully this study will prompt further work aimed at characterizing the structure of the kaolinite basal surface and indeed other layered 1:1 aluminosilicates, such as those in the trioctahedral serpentine group and other dioctahedral kaolinite group minerals which are likely also to suffer from the same interesting complications highlighted here.

Chapter 6

Towards a general understanding of water monomer adsorption on rocksalt oxide surfaces

Water-oxide interfaces have been widely examined, yet simple but fundamental questions remain unanswered and general rules to predict how stable and in which state (intact or dissociated) water will be in on a given surface have not yet been identified. As a first step towards addressing these issues, DFT calculations have been performed for water on a series of simple rocksalt oxide (001) surfaces. Specifically, water monomer adsorption and dissociation is examined on the alkaline earth oxide series from MgO to BaO. It is revealed that as one moves down the series both the adsorption energy of water and its tendency to dissociate increase. Intact water is stabilized through hydrogen bonds to the substrate, which increase in strength as one moves down the series. The dissociated state resembles two interacting hydroxyl ion groups, whose mutual repulsion also decreases upon descending the series. Of crucial importance to all of these observations is the rumpling of the substrate and its lattice constant.

6.1 Introduction

The interaction of water with metal, oxide, and semiconductor surfaces has attracted a great deal of attention because of its importance to a variety of scientific disciplines and industrial applications [6, 7]. A fundamental question to many of these studies is to understand the adsorption structures of water on surfaces and in particular to know which state the water is in: either intact or dissociated. This is important to know because the properties of interfacial water systems differ greatly depending on whether the water molecules dissociate or not. For example, water dissociation at metal surfaces can be the first step in oxidation leading to corrosion or at oxide surfaces can lead to hydroxylation and hydride formation. This will leave the surfaces with very different properties to those of a simple "wet" surface covered in intact molecular water.

Many factors can affect the dissociation of water on surfaces. The presence of defects has long been known to promote dissociation, for example, on MgO and TiO_2 [7, 149]. Another factor, as shown before [150, 151] and in the next chapter, is the interaction (hydrogen bonding) between water molecules which can facilitate water dissociation through the increased strength of water-hydroxyl hydrogen bonds compared to water-water hydrogen bonds. The water-surface interaction or surface reactivity is, of course, another crucial factor. Here I consider the water-surface interaction and in so-doing focus exclusively on water monomer adsorption so as to establish the inherent reactivity of a range of surfaces to water adsorption. The surfaces examined are a series of (001) surfaces of alkaline earth metal oxides with the rocksalt structure (MgO, CaO, SrO, and BaO). These have been selected mainly because they are a periodic series of oxide surfaces with a simple structure, but also some of them have been widely studied before [23, 27, 28, 152].

The main results to come from this study are the following: as one moves down the series both the adsorption energy of water and its tendency to dissociate increase. Intact water is stabilized through hydrogen bonds to the substrate, which increase in strength as one moves down the series. The dissociated state resembles two interacting hy-

droxyl ion groups, whose mutual repulsion also decreases upon descending the series. Of crucial importance to each of these observations is the rumpling of the substrate and its lattice constant. It is hoped that this study will represent a small but important step towards a general theory of water adsorption on oxide surfaces.

The remainder of this chapter is organised as follows. Computational details are briefly presented in the next section. In Section 6.3 the general trends observed with regard to water adsorption and dissociation are presented. Following this the nature of the (intact and dissociated) water monomer adsorption bond is discussed and analysed. In Section 6.4 some conclusions are drawn.

6.2 Computational details

DFT calculations were performed with the periodic plane wave code VASP [37, 38] using the PBE [50, 51] exchange-correlation functional, PAW potentials, and a 400 eV plane wave cutoff. With the chosen PAW potentials[1] [68, 69], the PBE values of the bulk lattice constant (a_0) are 4.25 Å for MgO, 4.84 Å for CaO, 5.20 Å for SrO, and 5.61 Å for BaO, respectively. Each of these values are similar to previous GGA-PBE or GGA-PW91 calculations [153–155] and slightly overestimated compared to experimental values of 4.21 Å for MgO, 4.81 Å for CaO, 5.16 Å for SrO and 5.52 Å for BaO [64]. All calculations involved (001) surfaces in which the slabs were three layers thick[2] with a fixed bottom layer in a $(1.5\times1.5)\sqrt{2}a_0$ surface cell. A $2\times2\times1$ Monkhorst-Pack [66] $\boldsymbol{k}$ point mesh was used to sample the Brillouin zone. The vacuum region between slabs is 15 Å and the dipole across the slab, present because of

[1]The particular PAW potentials used treat the following electrons as valence electrons: Mg, $2p^6 3s^2$; Ca, $3s^2 3p^6 4s^2$; Sr, $4s^2 4p^6 5s^2$; Ba, $5s^2 5p^6 6s^2$; and O, $2s^2 2p^4$.

[2]An eight layer thick slab yields an adsorption energy of (intact or dissociated) water on each surface within 10 meV of that obtained with the three layer thick slab. Specifically, the adsorption energy in the most stable adsorption structure is -0.48 (-0.48), -0.90 (-0.91), -1.26 (-1.27), -1.49 (-1.48) eV with three (eight) layer slabs on MgO, CaO, SrO, and BaO, respectively.

adsorption on just on one side of the slab, was corrected by the scheme introduced by Neugebauer and Scheffler [134]. During structure optimizations all forces on relaxed ions are reduced below 1.5 meV/Å.

Some quantities used in this chapter are defined here. The adsorption energy of a water monomer on the (001) surface is defined as usual by

$$E_{ads} = E_{water/MO} - E_{MO} - E_{water}, \tag{6.1}$$

where $E_{water/MO}$, E_{MO}, and E_{water} are the total energies of the intact or dissociated water monomers adsorbed on the (001) surfaces, the clean surfaces, and the isolated water molecule, respectively. In the analysis below, the adsorption energy is decomposed into energy contributions from the bonding to the surface and the structure deformation. The part designed to reveal exclusively the interaction between the water monomer and the substrate, E_{bond}, is defined as

$$E_{bond} = E_{water/MO} - E^*_{MO} - E^*_{water}, \tag{6.2}$$

where E^*_{MO} and E^*_{water} are the total energies of the isolated clean oxide slab and the isolated water monomer in vacuum, each fixed in the structure they assume in the adsorption system. The energetic contribution coming from structural deformation of the water monomer and substrate, E_{str}, is defined as

$$E_{str} = E^*_{MO} + E^*_{water} - E_{MO} - E_{water}, \tag{6.3}$$

where all terms are defined as in Eqs. (6.1) and (6.2). To reveal the nature of the interaction between the monomer and the substrate, the electron density rearrangement, $\Delta\rho$, is defined as

$$\Delta\rho = \rho_{water/MO} - \rho_{MO} - \rho_{water}, \tag{6.4}$$

where $\rho_{water/MO}$, ρ_{MO}, and ρ_{water} are the electron densities of the particular water-oxide adsorption system under consideration, the isolated clean rocksalt oxide (001) surface, and the isolated water monomer, each in the exact structure they adopt in the adsorption system. Finally, the degree of rumpling of the (001) surfaces is evaluated by

$$\Delta d = d_M - d_O, \tag{6.5}$$

where d_M and d_O are the heights of the metal and oxygen ions of the outermost MO layer. With this definition a positive Δd indicates that the metal ions in the outermost layer are higher (i.e., further out in to the vacuum) than the oxygen ions.

6.3 Adsorption and dissociation trends

6.3.1 Adsorption structure and energy

To begin, I discuss some of the relevant adsorption structures identified for water on the four surfaces (Fig. 6.1). Fig. 6.1a shows the most stable intact monomer structure on MgO(001). This structure has the oxygen of the water molecule located $\sim$2.2 Å above a Mg site with one of the OH bonds directed at a neighbouring oxygen site to form a hydrogen bond of $\sim$1.7 Å and the other OH bond is directed toward the vacuum. The adsorption energy of this structure is -0.48 eV. Slightly less stable, with an adsorption energy of -0.46 eV, is a symmetric structure (not shown), where the oxygen of the water molecule is located above the Mg site but with the two OH bonds directed to neighbouring oxygen sites to form hydrogen bonds of $\sim$2.0 Å. Several other intact water monomer adsorption structures on MgO(001) have also been identified with adsorption energies between -0.30 and -0.40 eV, but no stable dissociated water monomer structures were identified. Intact water monomers on the three other surfaces adopt an alternative structure (Fig. 6.1b), where the oxygen of the water molecule is located on a hollow site with the two OH bonds directed towards surface oxygen sites. The adsorption energy of this structure is -0.70, -0.84, and -0.85 eV on CaO, SrO, and BaO, respectively. However, on these three surfaces, dissociated water structures are more stable than intact monomer structures. The most stable dissociated monomer structure identified on the three surfaces is similar and is shown in Figs. 6.1c. One hydrogen of the water is adsorbed on the surface oxygen site and the hydroxyl sits upright with the hydroxyl bond directed toward the vacuum. The adsorption energy of this dissociated

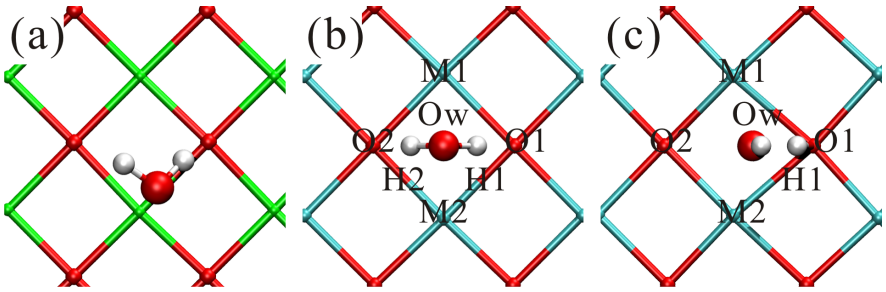

Figure 6.1: Water monomer adsorption structures on MO (M = Mg, Ca, Sr, and Ba) (001) surfaces: (a) the most stable structure of a water monomer on MgO(001); (b) the most stable structures for an intact water monomer on CaO, SrO, and BaO; (c) the most stable dissociated structures for a dissociated water monomer on CaO, SrO, and BaO. In (c) and (d) some ions are labelled for discussion purposes. White, red, and green (blue) spheres represent hydrogen, oxygen, and metal ions, respectively.

structure is -0.90, -1.26, and -1.49 eV on CaO, SrO, and BaO, respectively[3]. Thus, overall the calculations predict that water monomers remain intact on MgO(001) but dissociate on the three other rocksalt oxide (001) surfaces, which is in agreement with a recent study [155].

So as to understand more clearly the variation in the adsorption behaviour on descending the alkaline-earth oxide series (from Mg to Ba), the energies of the intact and dissociated states are plotted in Fig. 6.2. Two main features are apparent from Fig. 6.2. First, the energy of the intact and dissociated water states increases (i.e., becomes more stable) upon descending the series. Second, the energy of the dissociated state drops more rapidly than that of the intact state with the consequence that the tendency to dissociate increases as one moves down the series. These trends are now discussed with a detailed analysis of the electronic structures of the various adsorption systems.

[3]Several other less stable dissociated structures ($\sim$0.1 to $\sim$0.2 eV less stable) have been identified, but are not shown here or discussed further.

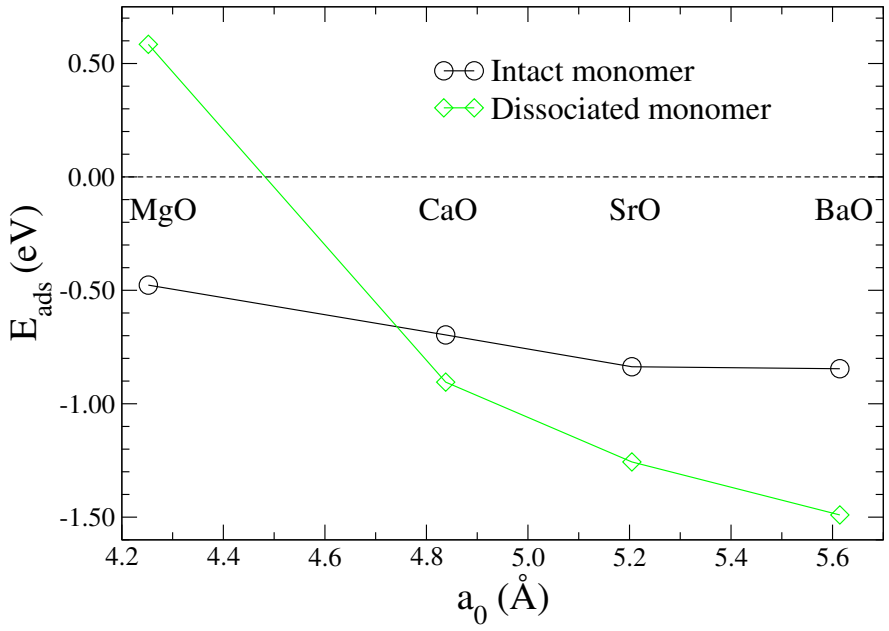

Figure 6.2: Adsorption energies of the most stable intact and dissociated monomer structures on MO (M = Mg, Ca, Sr, and Ba) (001) surfaces as a function of lattice constant. The most stable intact water monomer structure on MgO(001) is shown in Fig. 6.1a. The energy shown for the dissociated monomer on MgO(001) corresponds to an adsorption structure where the proton and the hydroxyl of the dissociated water are at least $\sim$3.5 Å so as to prevent them from recombining. The most stable intact and dissociated monomer structures on the other three surfaces are shown in Figs. 6.1b and c, respectively.

6.3.2 Intact water monomer analysis

As shown in Fig. 6.2, the adsorption energy of the (intact and dissociated) water monomer increases as one moves from the top (MgO) to the bottom (BaO) of the alkaline earth oxide series. To understand the trend, the electronic and geometric structures of the intact water monomer are analysed now. Specifically, the stable intact water adsorption structure shown in Fig. 6.1b is considered[4]. The partial DOS (PDOS) of the oxygen of the water molecule, the surface oxygen, and the metal ions are shown in Fig. 6.3 for the four surfaces. On each surface, three main peaks on the water are observed, corresponding to the three higher energy occupied molecular orbitals of the water molecule. A careful examination of the individual Kohn-Sham eigenstates within each peak reveals that states within the lower energy peak at $\sim$-7 to $\sim$-8 eV are mainly of $\mathbf{1b}_2$ character of water plus a small contribution from p states of the surface oxygen. States within the intermediate energy peak at $\sim$-4 to $\sim$-5 eV are of $\mathbf{3a}_1$ character of water mixed with p states from the valence band of the substrate. This is the main mixed adsorbate-substrate state in each adsorption system. States within the higher energy peak are of $\mathbf{1b}_1$ character of the water mixed very weakly with the substrate. Representative eigenstates from each of these three peaks are displayed in Fig. 6.3. Given the very minor overlap between the water and the substrate in each of these states, demonstrating the absence of any significant covalent bond formation, it is concluded that the nature of the interaction of water with the substrate is mainly electrostatic. Moreover, from the plots in Fig. 6.4 of the electron density rearrangement it can be seen that the electrostatic interaction is dominated by hydrogen bonding between water and the surface oxygen sites: The plots of the electron density rearrangement resemble those often seen for hydrogen bonded systems [98, 102, 115], with characteristic depletion of density on the hydrogen and density accumulation on the two oxygens on either side of the hydrogen bond. To further substantiate the suggestion that the adsorption to the surface happens primarily through hydrogen bonding an artificial adsorption structure was examined where the water molecule is flipped so

[4]For convenience in comparing with the three other surfaces, this specific structure is also used on MgO(001) despite it not being the most stable intact water adsorption structure on this surface.

that the two OH bonds are directed to the vacuum (with the other parts of the water-oxide adsorption system remaining unchanged). The adsorption energy ($E_{ads}^{no\ HB}$) of this specific structure is listed in Table 6.1 for each surface compared to that of the original stable adsorption structure. Without the hydrogen bonds between water and the surface, this structure is very unstable. In fact the interaction is repulsive on each and the adsorption energy increases monotonously upon descending the series, e.g., from 0.04 eV on MgO(001) to 0.45 eV on BaO(001).

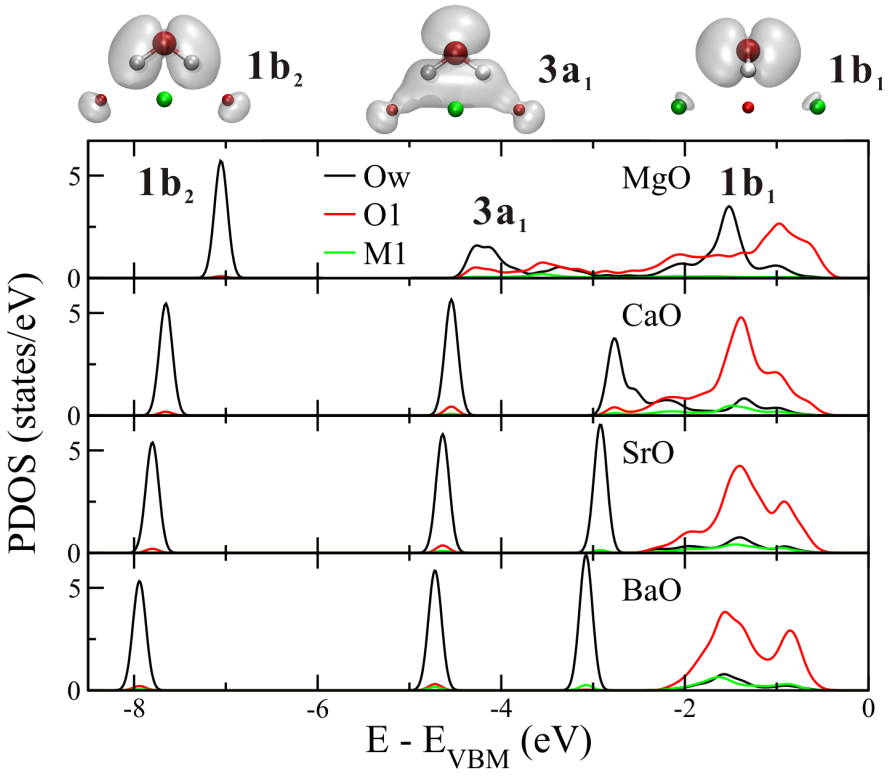

Figure 6.3: Partial density of states (PDOS) of the oxygen (Ow) of the intact water monomer, the surface oxygen (O1), and metal ions (M1) for the four surfaces. The specific Ow, O1, and M1 ions are labelled in Fig. 6.1b. The energy window shown depicts the three highest occupied Kohn-Sham orbitals (mostly $\mathbf{1b}_2$, $\mathbf{3a}_1$, and $\mathbf{1b}_1$ character from left to right) of the adsorbed water and three representative eigenstates from the three resonances are shown at the top of the figure. E_{VBM} is the energy of the valence band maximum.

To further understand these adsorption systems an energy decomposition of each ad-

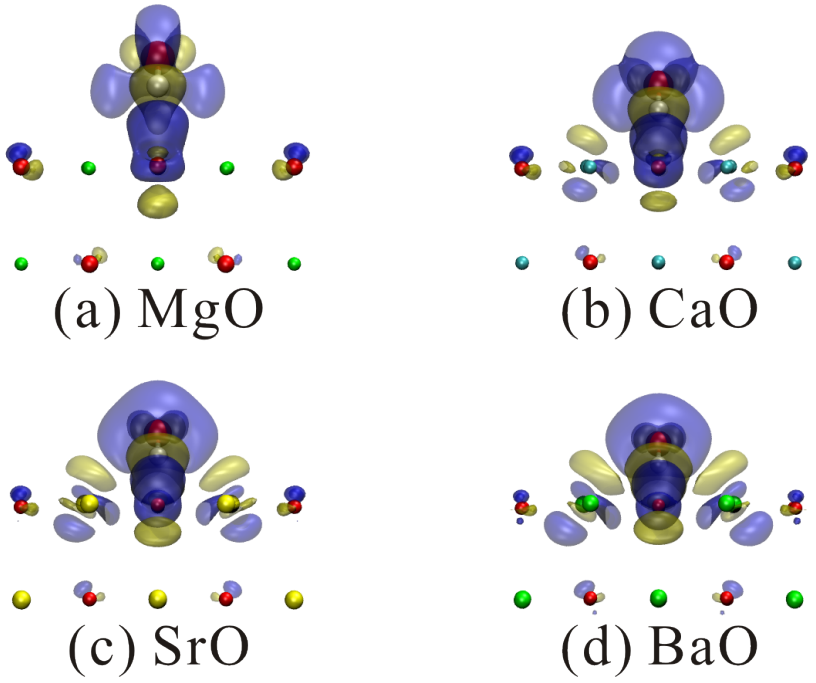

Figure 6.4: Electron density rearrangement of intact water with the structure shown in Fig. 6.1b (but viewed from the side here) on MO (M = Mg, Ca, Sr, and Ba) (001) surfaces. A constant density isosurface of 0.005 electrons/Å^3 is displayed. Blue regions indicate positive regions (electron accumulation) and yellow negative regions (electron depletion). With this side view, only one hydrogen of water is visible.

sorption system has been performed. Specifically, the adsorption energies are decomposed into: (i) the energy cost to deform to the adsorption structure; and (ii) the interaction energy between the deformed water and substrate. Precisely how each of these quantities are defined is given in Eqs. (6.2) and (6.3). As shown in Table 6.2, the interaction energy between water and the surface follows the same trend as the adsorption energy, i.e., it increases from the top to the bottom of the alkaline earth series. In contrast, the structural deformation part becomes more positive (unstable), from a cost of 0.07 eV for water on MgO(001) to 0.50 eV for water on BaO(001). This increasing deformation energy is in agreement with the structural information listed in Table 6.2. In Table 6.2 the OH bond length ($r_{(Ow-H1)}$) and the bond angle ($\angle_{(H1OwH2)}$) of water increases upon descending the series, and thus the water is deformed more on BaO(001) than on MgO(001). Associated with this, the length ($r_{(H1-O1)}$) of the hydrogen bond

Table 6.1: Energy decomposition of water monomer adsorption with the intact structure shown in Fig. 6.1b on rocksalt oxide (001) surfaces. E_{bond} and E_{str} are defined in Eqs. (6.2) and (6.3), respectively. $E_{ads}^{no\ HB}$ is the adsorption energy of the water interacting with the surface without hydrogen bonds (see the text for more details). All values are in units of eV.

	E_{ads}	E_{bond}	E_{str}	$E_{ads}^{no\ HB}$
MgO	-0.33	-0.40	0.07	0.04
CaO	-0.70	-0.91	0.21	0.11
SrO	-0.84	-1.16	0.32	0.22
BaO	-0.85	-1.35	0.50	0.45

between water and the surface oxygen site decreases, e.g., the hydrogen bond lengths decrease from 1.90 Å on MgO(001) to 1.65 Å on BaO(001), which means that the strength of the hydrogen bond increases. Similarly, the height of the water molecule above the surface (d_{Ow}) decreases from 2.36 Å on MgO to 1.77 Å on BaO. Therefore, it is suggested that this ability of the molecule to get closer to the surface and in so-doing form stronger hydrogen bonds is key to the increased adsorption energy as one moves down the alkaline earth oxide series. This explanation for the increased adsorption energy is ultimately then related to geometric effects: the increasing lattice constant as one moves from MgO to BaO enables the molecule to approach the surface more closely and form stronger hydrogen bonds with it.

6.3.3 Dissociated monomer analysis

Following the intact water adsorption structure on the rocksalt oxide (001) surfaces, the dissociated water adsorption structure on CaO(001), SrO(001), and BaO(001) is discussed now. The specific structure considered is the one shown in Fig. 6.1c. The PDOS over the hydroxyl oxygen, the surface oxygen to which the dissociated hydro-

Table 6.2: Bond length and angle in the intact water adsorption structure shown in Fig. 6.1b. $r_{(H1-O1)}$ is the length of the hydrogen bonds between water and the surface oxygens; d_{Ow} is the height of the adsorbed oxygen of water relative to the outermost surface layer (the maximum height of any ions in the outermost layer); and $r_{(Ow-H1)}$ is the average length of the OH bonds in the water; $\angle_{(H1OwH2)}$ is the internal bond angle of water. All ions are labelled in Fig. 6.1b. Only one bond is labelled if there are two equivalent bonds in the symmetric structure. All values are in units of Å for the lengths and degrees for the angle.

	$r_{(H1-O1)}$	d_{Ow}	$r_{(Ow-H1)}$	$\angle_{(H1OwH2)}$
MgO	1.90	2.36	0.99	103.2
CaO	1.70	2.03	1.02	106.0
SrO	1.67	1.90	1.04	107.6
BaO	1.65	1.77	1.05	109.4

gen is bonded, and the metal ion on the three surfaces are reported in Fig. 6.5 for each surface. There are four main peaks belonging to the hydroxyl and surface oxygen (Ow and O1) in the energy interval shown and representative eigenstates from each peak are illustrated on the top of Fig. 6.5. In contrast to the PDOS of the intact water adsorption, the bonding picture that emerges here essentially involves the interaction between two hydroxyl ion groups: the adsorbed hydroxyl group and the surface hydroxyl group[5]. A careful examination of the Kohn-Sham eigenstates within each peak reveals that the two lowest energy peaks (states 1 and 2), which occur in the range of $\sim$-7 to $\sim$-5 eV, are a pair of bonding and antibonding states between the adsorbed hydroxyl and the surface hydroxyl. Specifically, they are p_z+p_z-like bonding and p_z-p_z-like antibonding states. This two-orbital, four-electron interaction is repulsive and destabilizing [156]. It can be seen, however, that the splitting between the two states is reduced as one moves down the series from CaO to BaO. This is simply because of the

[5]The surface hydroxyl group is formed by the surface oxygen and the dissociated hydrogen.

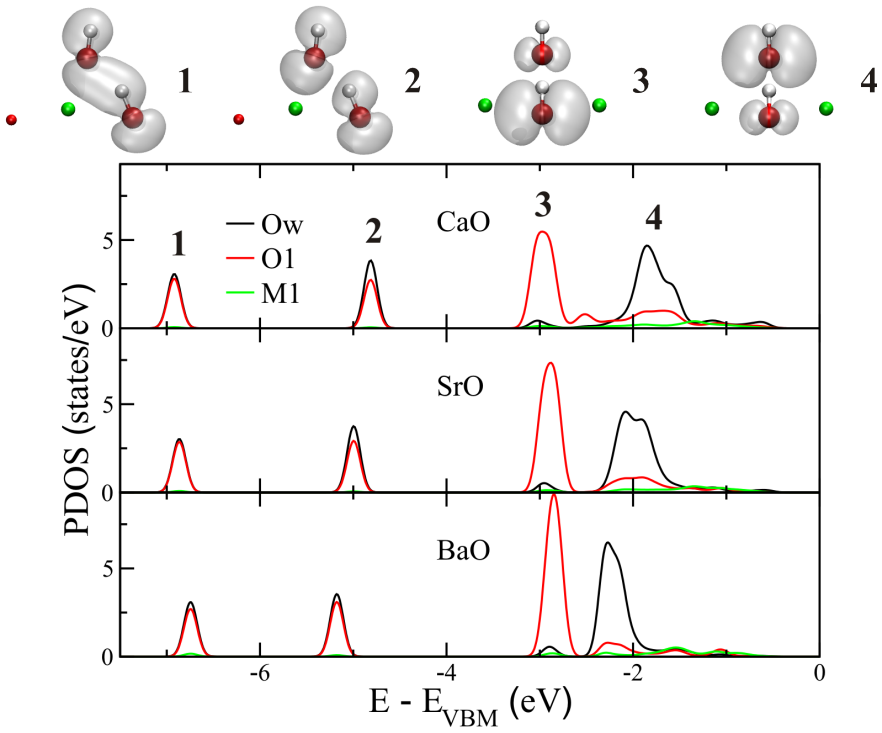

Figure 6.5: PDOS of the oxygen (Ow) of the dissociated water monomer and the surface oxygen (O1) and metal ions (M1) for the three surfaces on which water dissociates. The specific Ow, O1, and M1 ions are labelled in Fig. 6.1c. The energy window shown depicts the highest occupied Kohn-Sham orbitals of the adsorbed hydroxyl group and and the surface hydroxyl group. Representative eigenstates from the four main resonances are also shown.

increasing lattice constant which means that the two hydroxyl groups are further apart from each other on BaO compared to CaO (see Table 6.3). The higher energy states (states 3 and 4) correspond to the other p orbitals (p_x and p_y) of the surface hydroxyl and the adsorbed hydroxyl, respectively. These states are fully occupied, revealing that each oxygen has its full compliment of $\sim$6 p electrons. This indicates that water dissociation on each surface produces two hydroxyl ions. Indeed this is confirmed by a Bader analysis [148] that reveals both hydroxyl groups carry a charge of $\sim$0.8 electrons. Thus it can easily be understood that as the separation between the two hydroxyl ions increases (upon descending the series) the systems are stabilised.

Table 6.3: Bond lengths in the dissociated water adsorption structure shown in Fig. 6.1c. Here $r_{(Ow-H1)}$ is the bond length of the dissociated hydrogen with the oxygen of the adsorbed hydroxyl; d_{Ow} is the height of the adsorbed hydroxyl relative to the outermost layer (the maximum height of ions on the outermost layer); and $r_{(H1-O1)}$ is the bond length of the dissociated hydrogen with the surface oxygen. All ions are labelled in Fig. 6.1c. All values here are in units of Å.

	$r_{(Ow-H1)}$	d_{Ow}	$r_{(H1-O1)}$
CaO	1.49	1.75	1.04
SrO	1.59	1.76	1.02
BaO	1.68	1.79	1.01

6.3.4 Surface relaxation and lattice constant

To better understand water dissociation some additional analysis has been performed. First, the effect of surface relaxation was examined, revealing that it plays an important role. Specifically, the tendency for water to dissociate decreases if the surface is held fixed. The evidence for this can be seen by comparing the adsorption energies of the structure in Fig. 6.1c on the fixed and relaxed surfaces (Table 6.4). In each case the adsorption energy is reduced by ∼0.4 eV on the fixed substrate compared to the relaxed substrate. On CaO(001) this is actually sufficient to make the intact state more stable than the dissociated state when the surface is fixed. Thus, it is clear that the surface relaxation (or more precisely, the surface rumpling as discussed below) impacts upon the properties of each substrate with regard to water monomer adsorption and dissociation. Looking at this in more detail, the average displacements of the ions close to the adsorbate (two metal ions MI and M2, and two oxygen ions, O1 and O2 labelled in Fig. 6.1c) are listed in Table 6.5 for each surface. The average displacements when water has dissociated (i.e., water on CaO(001), SrO(001), and BaO(001)) are ∼0.2 Å, much larger than the 0.05 Å when water has not dissociated (i.e., water on MgO(001)). Upon inspection of the various substrate ions it is noticed that water adsorption is as-

Table 6.4: Water adsorption energy on relaxed and unrelaxed (001) surfaces with the adsorption site shown in Fig. 6.1c. On the relaxed surfaces only the atoms in the bottom layer of the slab are fixed and the other atoms including water are fully relaxed. On the unrelaxed surfaces all substrate atoms are artificially fixed at the fully relaxed clean surface positions while water is relaxed. The text in the parentheses indicates whether the water monomer is dissociated in each case. All values are in units of eV.

E_{ads}	relaxed	unrelaxed
MgO	-0.34 (Int)	-0.30 (Int)
CaO	-0.90 (Diss)	-0.61 (Int)
SrO	-1.26 (Diss)	-0.87 (Diss)
BaO	-1.49 (Diss)	-1.11 (Diss)

sociated with outward motion of the metal ions. In addition this outward motion of the metal ions increases from 0.05 Å for MgO to 0.23 Å for BaO. It is also noticed that the clean surfaces themselves (in the absence of any water) exhibit a similar trend with respect to the degree of surface rumpling (Table 6.5)[6]. Thus some additional calculations were performed to establish a possible connection between surface rumpling and water dissociation. To this end, a series of artificial structures have been built on CaO(001) with the substrate fixed at the relaxed surface positions and the metal ions on the outermost layer then moved upwards with a desired Δd. From the OH bond lengths ($D_{(Ow-H1)}$ and $D_{(O1-H1)}$) of the dissociated hydrogen (H1 labelled in Fig. 6.1c) with water oxygen (Ow) and substrate oxygen (O1), it can be seen in Table 6.6 that the water monomer gradually dissociates as the surface rumpling is increased.

A relation between water dissociation and surface rumpling has been revealed. To

[6]In agreement with previous DFT studies [153, 154], on the clean MgO(001) surface the metal ions sit inside the oxygen ions, with a negative value of the rumpling Δd. On CaO(001) the rumpling is almost zero and on SrO(001) and BaO(001) a positive rumpling is obtained, with the metal ions outside the oxygens.

Table 6.5: Surface rumpling for the clean (001) oxide surfaces and average displacement of substrate ions after water is adsorbed on the adsorption site shown in Fig. 6.1c. Δd is the surface rumpling of the clean relaxed surfaces. The average displacement of the four substrate ions close to the adsorbed water monomer (as labelled in Fig. 6.1c) is defined as $r = \frac{1}{4}\sum_{i=1}^{4}|r_i - r_i^0|$, where r_i and r_i^0 are the positions of four labelled atoms before and after water adsorption. The displacement of the metal ion (M1) and the oxygen ion (O1) are given as well. All values here are in units of Å.

	Δd	r_{M1}	r_{O1}	r
MgO	-0.05	0.05	0.04	0.05
CaO	0.01	0.20	0.17	0.18
SrO	0.05	0.21	0.18	0.19
BaO	0.11	0.23	0.17	0.20

Table 6.6: Adsorption structure on artificially rumpled CaO(001). These substrate structures are built from the clean CaO(001) surface and metal ions on the outermost layer were moved upwards and fixed to have a desired Δd. $r_{(Ow-H1)}$ and $r_{(O1-H1)}$ indicate the lengths of the two hydroxyl bonds (Fig. 6.1c). All values are in units of Å.

Δd	$r_{(Ow-H1)}$	$r_{(O1-H1)}$
0.01	1.08	1.43
0.05	1.10	1.38
0.10	1.23	1.20
0.15	1.33	1.12
0.20	1.39	1.08

Table 6.7: Adsorption energy of rumpled surfaces with a value of 0.1 Å for Δd and the energy cost to generate the desired rumpled surfaces. E_{ads} here shows the energy gain of the water adsorption structure shown in Fig. 6.1c relative to the total energies of the most stable fully relaxed clean surface and the gas phase water and E_{str}^{clean} the energy difference between the desired surface and the most stable surface. Whether water is intact or dissociated is indicated in the parentheses. All values are in units of eV.

	E_{ads}	E_{str}^{clean}
MgO	0.64 (Int)	1.01
CaO	-0.42 (Diss)	0.30
SrO	-0.88 (Diss)	0.09
BaO	-1.10 (Diss)	0.00

understand this relation in more general terms water adsorption and the question of whether or not it dissociates was examined on all four substrates, with each substrate fixed at the same degree of rumpling. Specifically, the metal ions of the outermost layer of each (001) surface are moved upwards to have a Δd of 0.1 Å. Water with the structure shown in Fig. 6.1c is then allowed to relax on each surface. It can be seen from Table 6.7 that water is not stable on the rumpled MgO(001) surface compared to on other surfaces. Much more energy is required to buckle MgO to enable water dissociation than for BaO(001) due to the fact that the energy to buckle the clean surface (E_{str}^{clean}) decreases as one moves down series. Thus, the easier it is to displace surface atoms, the stronger the adsorption can be and the more favoured water dissociation is.

The lattice constant (or the strain in the surface plane) was another factor investigated. Specifically, the lattice constants of CaO(001) and BaO(001) were exchanged and water adsorption in the structure of Fig. 6.1c on these strained substrates examined (Table 6.8). In contrast to a regular BaO substrate, it is found that water does not dissociate

Table 6.8: Adsorption energy of water monomer on various CaO(001) and BaO(001) substrates. $a_0(CaO, clean)$ and $a_0(BaO, clean)$ indicate that the substrates adopt the lattice constants and fully relaxed clean surface structures of CaO and BaO, respectively. $a_0(CaO, bulk)$ and $a_0(BaO, bulk)$ indicate that the substrates have bulk truncated surface structures at the CaO and BaO, respectively. E_{ads} is defined in Eq. (6.1), where, however, the total energies of the clean surface (E_{MO}) are different, i.e., they are the total energy of each fully relaxed or bulk truncated surface with the indicated lattice constants. Whether water is dissociated or not is indicated in each case. All values are in units of Å for distance and eV for energy.

E_{ads}	$a_0(CaO, clean)$	$a_0(BaO, clean)$	$a_0(CaO, bulk)$	$a_0(BaO, bulk)$
CaO	-0.61 (Int)	-1.39 (Diss)	-0.60 (Int)	-1.21 (Diss)
BaO	-0.45 (Int)	-1.10 (Diss)	-0.46 (Int)	-1.00 (Diss)

on a BaO substrate which is compressed to the CaO lattice constant. Similarly expanding CaO to adopt the BaO lattice constant makes the perfect unrelaxed CaO substrate reactive enough to dissociate water. Thus, it is again seen, that the lattice constant of the substrate is relevant to the question of water adsorption and dissociation. Finally, in separate studies (not shown) smaller variations in the lattice constant of CaO were made ($\pm 2\%$ from the equilibrium) and a clear correlation between the substrate lattice constant and adsorption energy was observed.

6.4 Conclusions

In conclusion, water monomer adsorption and dissociation on rocksalt oxide (001) surfaces has been investigated with DFT and some understanding of the factors controlling the reactivity of water-oxide interactions obtained. From the stability comparison of

the intact and dissociated water monomer on these surfaces, it is shown that as one moves down the series both the adsorption energy of water and its tendency to dissociate increase. Intact water is stabilized through hydrogen bonds to the substrate, which increase in strength as one moves down the series. The dissociated state resembles two interacting hydroxyl ion groups, whose mutual repulsion also decreases upon descending the series. Of crucial importance to each of these observations is the rumpling of the substrate and its lattice constant. It is hoped that through further analysis and by extending this work to other oxide surfaces, a more complete picture of the general principles underlying water adsorption and dissociation will be obtained.

Chapter 7

Proton transfer in adsorbed water dimers on MgO

DFT simulations of water on MgO(001) reveal rapid proton transfer within clusters of just two water molecules. Facile dissociation and recombination of the molecules within the dimers along with a concerted surface-mediated exchange of protons between water and hydroxyl molecules makes this possible. It is suggested that surface-mediated proton transfer is in general likely to lead to proton transfer in interfacial water systems whenever the relative energies of intact and dissociated states of water are similar.

7.1 Introduction

Proton transfer between water molecules is a fundamental process in chemistry, biology, and physics. For example it is central to all acid/base reactions in aqueous media, to water wires inside proteins and to the electrical conductivity of ice [15]. The Grotthuss mechanism [16, 17] has for more than 100 years provided the basic picture for how protons or protonic defects diffuse through extended 3D hydrogen bonded networks. However, less is known about proton transport where extended 3D networks

do not persist. A prominent example is water at interfaces, where understanding of proton transport is in its infancy despite compelling environmental and economic incentives to better understand the molecular-level details of e.g. nanofluidics, corrosion, and electrochemistry. Nonetheless, water at interfaces, particular at well-defined oxide, semiconductor, and metal surfaces, provides an excellent opportunity to probe the most intimate details of proton transport, as demonstrated by recent experimental and theoretical studies [14, 114, 157–159].

Here DFT simulations of water on MgO(001) are reported. This is one of the most widely studied interfacial water systems [7] and it is shown that despite having been intensively interrogated for the last twenty years it still has interesting secrets of general importance to reveal. Specifically it is shown that adsorbed water clusters of just two molecules (i.e. dimers) are sufficient to facilitate proton transfer between oxygen atoms. Facile dissociation and recombination of the molecules within the dimers along with a concerted surface-mediated exchange of protons between water and hydroxyl molecules makes this possible. It is suggested that surface-mediated proton transfer is in general likely to lead to proton transfer in interfacial water systems whenever the relative energies of intact and dissociated states are similar.

7.2 Computational details

DFT calculations were performed with the periodic plane wave codes CASTEP [35, 36] and VASP [37, 38]. Most results have been obtained with the PBE exchange-correlation functional [50, 51], although results of test calculations with the hybrid PBE0 [56, 59] functional are also reported. The Born-Oppenheimer MD simulations reported here were within the canonical ensemble (NVT), had deuterium masses for the hydrogens, and a 1 fs timestep. All MD simulations ran for either 25 or 50 ps and were performed on a thin two layer MgO slab along with a $(2\times2)a_0$ surface cell (a_0=4.25 Å for PBE and 4.21 Å for PBE0), Γ point sampling of the Brillouin zone, and

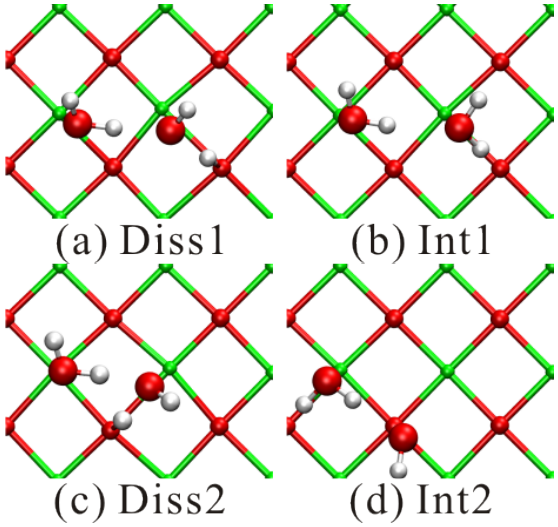

Figure 7.1: Top views of water dimer structures on MgO(001). Diss1 and Diss2 are the partially dissociated H_2O-OH-H dimers and Int1 and Int2 are the intact water dimers. The white, red, and green spheres are hydrogen, oxygen, and magnesium atoms, respectively.

a 400 eV plane wave cutoff. An extensive set of test calculations, some of which are reported in Table 7.1, revealed that this set-up yielded adsorption energies of each of the key adsorption structures shown in Fig. 7.1 that come within 0.02 eV/H_2O of those obtained with more expensive settings (four or eight layer MgO slabs in a $(2\times2)\sqrt{2}a_0$ surface cell with $2\times2\times1$ Monkhorst-Pack [66] $\boldsymbol{k}$ point sampling). Adsorption energies are defined here relative to isolated gas phase water molecules and clean surfaces through

$$E_{ads} = (E_{water/MgO} - E_{MgO} - n \cdot E_{water})/n, \tag{7.1}$$

where $E_{water/MgO}$, E_{MgO}, and E_{water} are the total energies of the intact or partially dissociated water clusters adsorbed on the surface, the clean surface, and the isolated water molecule, respectively. n is the number of adsorbed intact or partially dissociated water molecules in each adsorption structure. In addition, it can be seen from Table 7.1 that the results obtained from CASTEP (with ultra-soft pseudopotentials [67]) and VASP (with PAW potentials [68, 69]) agree to within 0.02 eV/H_2O.

Table 7.1: Adsorption energies (eV/H_2O) on MgO(001) for the structures shown in Fig. 7.1 and the water monomer. Values have been obtained with VASP except those in parentheses, which are from CASTEP.

	Diss1	Int1	Diss2	Int2	Monomer
PBE[a]	-0.57	-0.51	-0.61	-0.50	-0.48
PBE[b]	-0.57	-0.52	-0.61	-0.50	-0.48
PBE[c]	-0.55	-0.51	-0.59	-0.50	-0.48
	(-0.57)	(-0.52)	(-0.60)	(-0.50)	(-0.49)
PBE0[c]	-0.56	-0.53	-0.59	-0.49	-0.48

[a] Four layer MgO slab, 2×2×1 ***k*** point sampling, $(2\times2)\sqrt{2}a_0$ cell.

[b] Eight layer MgO slab, 2×2×1 ***k*** point sampling, $(2\times2)\sqrt{2}a_0$ cell.

[c] Two layer MgO slab, single (Γ) ***k*** point, $(2\times2)a_0$ cell.

7.3 Monomer and dimer adsorption structures

Before discussing the water dimer, water monomer adsorption is worth briefly mentioning again, although it has been discussed in Chapter 6. The most stable monomer adsorption structure as shown in Fig. 6.1a of Chapter 6, with an adsorption energy of ∼-0.5 eV (Table 7.1), has the oxygen of the water molecule located ∼2.2 Å above an Mg site with one of the OH bonds directed at a neighboring O site and the other OH bond directed toward the vacuum [155, 160, 161]. An extensive series of calculations were performed in an attempt to identify stable dissociated monomer structures. However, consistent with previous DFT studies [155, 162], the dissociated structures were considerably less stable (by at least ∼1 eV) than the intact molecular adsorption structure.

Moving to the water dimer, the situation is more complex and interesting. Several dimer structures with similar stabilities have been identified. Four particular structures are shown in Fig. 7.1. In stark contrast to the adsorbed water monomer, some low

energy structures include dissociated water molecules. Indeed, consistent with previous studies [163, 164], the most stable dimers are "partially dissociated" H_2O-OH-H complexes such as those shown in Fig. 7.1. In these partially dissociated structures the water molecule that is accepting the hydrogen bond has dissociated into an OH and a chemisorbed H. The chemisorbed H has a variety of surface sites at which to adsorb, but those closest to the OH of the dimer are most stable. In particular the chemisorbed H bonds preferentially to either the surface O site between the oxygens of the two adsorbates (Diss2 in Fig. 7.1) or to an O site adjacent to the OH and far from the water (Diss1 in Fig. 7.1). This chemisorbed H forms a bond $\sim$1 Å long to its surface O and a hydrogen bond $\sim$1.6 Å long to the oxygen of the OH. The O-O distance within the dissociated dimer is $\sim$2.5 to $\sim$2.6 Å, which is $\sim$0.2 to $\sim$0.4 Å shorter than the O-O distance in the intact water dimers (for example, Int1 and Int2 in Fig 7.1). Although the dissociated dimers are marginally more stable than the intact ones, the four dimers have similar stabilities with adsorption energies ranging from -0.5 to -0.6 eV/H_2O (Table 7.1). They are, therefore, only slightly more stable than two isolated monomers. A series of hybrid functional calculations with PBE0 supports the conclusions to come from PBE and demonstrates that the dissociated H_2O-OH-H complexes are not sensitive to large self-interaction errors as OH-H radical complexes in the gas phase are [165–167]. Specifically, from Table 7.1 it can be seen that the PBE and the PBE0 adsorption energies of the intact and dissociated dimer structures are all within $\sim$0.1 eV/H_2O. Likewise, the PBE and PBE0 structures are similar with all bond lengths in the various adsorption systems differing by $\lesssim$0.04 Å.

7.4 Proton transfer in the dimer

Ab initio MD simulations were performed on the monomer and dimers at temperatures ranging from 100 to 273 K, the approximate temperature range used to study water films on MgO(001) experimentally [168, 169]. Simulations of the water monomer showed that it readily varies its orientation and adsorption site, but otherwise does not

do anything unexpected [155, 161]. The water dimers on the other hand exhibit a range of interesting behavior, including several distinct types of proton transfer events. I now describe the key observations of these MD simulations.

During the MD simulations water dimers fluctuate between dissociated and intact states. As an example I show in Fig 7.2a results from a simulation at 200 K in which the dimer rapidly flips from a dissociated state (Diss1) to an intact state (Int1). This can be seen by looking at the O-H bond lengths: when both the O^B-H^1 (green) and O^B-H^2 (orange) bonds are short ($\sim$1 Å) the dimer is intact and when one of the bonds is long ($\sim$1.6 Å) the dimer is dissociated. Therefore, during the 25 ps shown the dimer flips between dissociated and intact states about fourteen times. Either one of the two covalent O-H bonds in the acceptor water molecule can break, due to the easy rotation of this molecule in the intact state. The key to whether the covalent bond dissociates is the O-O separation (or equivalently the hydrogen bond length) between the two molecules. Specifically, when the O-O bond is short ($\sim$2.7 Å) the dimer is dissociated and either H^1 or H^2 is on the surface. When the O-O separation increases to $\sim$3 Å or more both water molecules in the dimer are intact. Therefore, the system resembles a molecular switch that is in a dissociated state if the hydrogen bond between the water molecules is short and in an intact state if it is long or broken. The switching between states is, of course, dependant on temperature and at lower temperatures no longer happens rapidly enough to be observed in the MD simulations. For example at 100 K the water dimer simply remains trapped in the more stable dissociated state. Similar transitions between the dissociated and intact states are observed for the Diss2 dissociated dimer. As an example in Fig. 7.2b I show 10 ps from a 273 K MD simulation. Again, exchange between the dissociated and intact structures and a coupling of this to the O-O separation are observed. Analogous switching between an intact and partially dissociated state has also been suggested for water on ZnO [170].

So far it has been seen from MD that through water dissociation and recombination there can be rapid proton transfer between the dimer and the MgO substrate. However

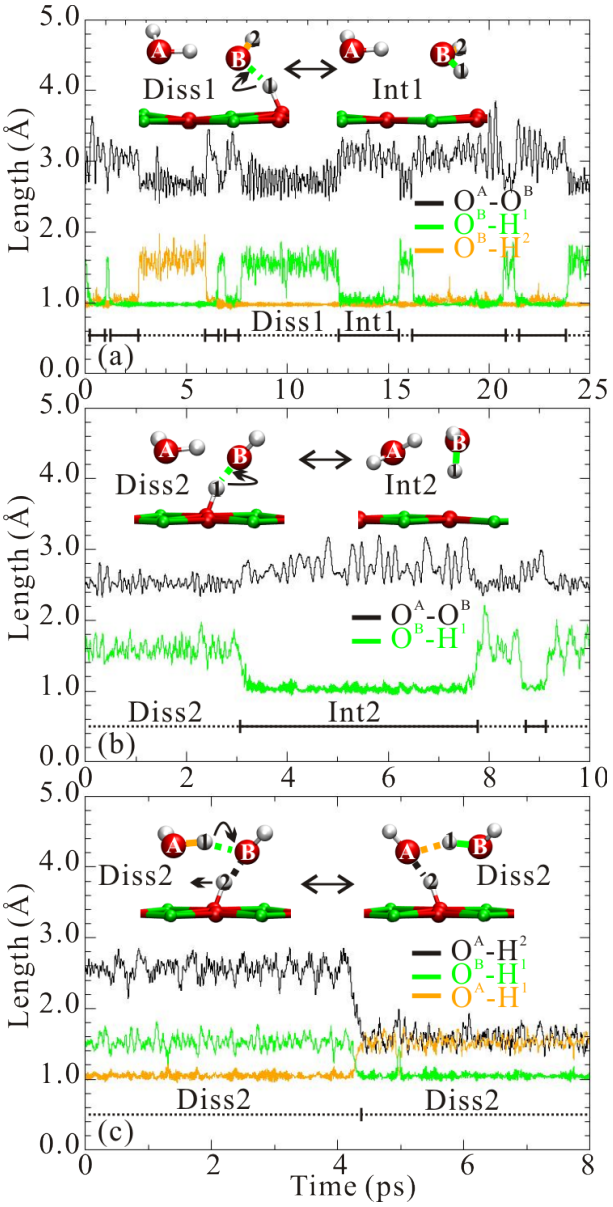

Figure 7.2: Selection of proton transfer events observed in MD simulations of water dimers on MgO(001). (a) Sequence of proton transfers between dissociated (Diss1) and intact (Int1) dimer states at 200 K. Easy rotation of the acceptor in the intact state allows both the O^B-H^1 and O^B-H^2 bonds to break. (b) Sequence of proton transfers between dissociated (Diss2) and intact (Int2) states at 273 K. (c) Surface-mediated proton transfer between two equivalent Diss2 states at 200 K: as the chemisorbed H^2 moves away from O^B toward O^A, H^1 is transferred in the opposite direction from O^A to O^B. Side views of the minimum energy structures of the relevant states in the MD simulations are shown in the insets. Top views are given in Fig. 7.1.

of more interest is a surface-mediated proton transfer mechanism that enables the concerted exchange of protons between the two molecules of the dimer. This exchange is illustrated in Fig. 7.2c, which reports the evolution of certain bond lengths during a 200 K MD simulation that started from Diss2. At the outset H^2 is on the surface forming a hydrogen bond with O^B. After $\sim$4 ps H^2 moves away from O^B toward O^A, forming a new hydrogen bond with O^A in the process. This change in allegiance of the adsorbed hydrogen can be seen in the O^A-H^2 distance which changes from $\sim$2.6 to $\sim$1.6 Å. Simultaneously H^1 transfers from O^A to O^B, as indicated by the changes in the O^B-H^1 (green) and O^A-H^1 (orange) distances. The effect of this concerted exchange of protons is that O^A is transformed from being part of the intact H_2O that donates the hydrogen bond to being part of the OH that accepts the hydrogen bond. In separate total energy calculations it was established with the climbing image nudged elastic band (cNEB) method [171] that the activation energy for this concerted surface-mediated transfer process is 0.11 eV. In the transition state both H^1 and H^2 are equidistant between O^A and O^B.

It has been shown that when two adsorbed monomers make a dimer that one of them can readily switch between an intact and a dissociated state. It has also been shown that through a surface-mediated proton transfer mechanism, the dissociated and non-dissociated molecules can be exchanged. These two types of proton transfer event allow the protons between the water molecules to be "scrambled" so that ultimately it is not appropriate to say that any given proton "belongs" to any particular oxygen. I illustrate schematically in Fig. 7.3 one sequence of events that would allow proton scrambling to happen with just two molecules. At first H^1 and H^2 are bonded to O^A and H^3 and H^4 to O^B. Should these two monomers combine to form a dissociated dimer H^1 can, for example, be transferred to O^B and H^4 to O^A through the surface-mediated proton transfer mechanism. If the dimer breaks apart the result is that one water is now formed from O^A, H^2 and H^4 and the other from O^B, H^1 and H^3. As well as observing each of the individual elementary steps with MD it has been confirmed that the total energy barrier for each step is low through cNEB calculations. As indicated

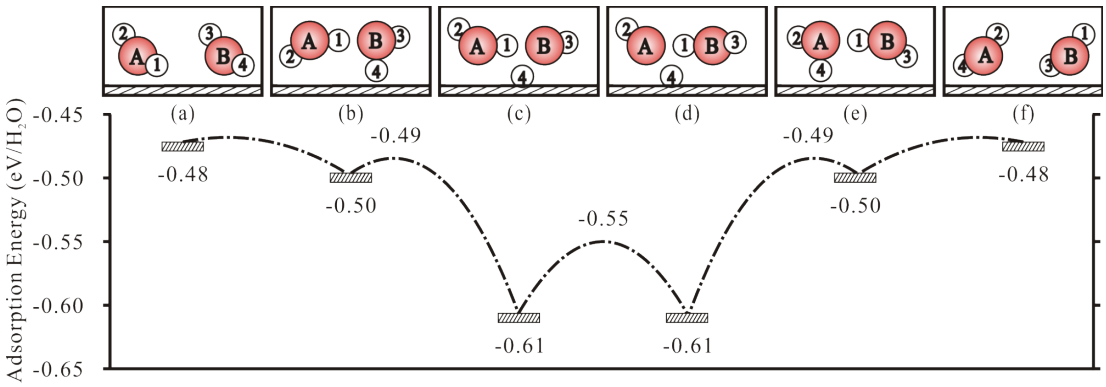

Figure 7.3: Schematic illustration and DFT-PBE energy profile for proton scrambling within water dimers on MgO(001), made possible by facile water dissociation and recombination plus surface-mediated proton transfer. (a) represents two isolated monomers, that in (b) combine to form an intact dimer (Int2 structure, Fig. 7.1d). In (c) the dimer has dissociated to the Diss2 structure (Fig. 7.1c). Surface-mediated proton transfer leads to (d), an equivalent dissociated dimer to the one in (c), that then leads to an intact dimer (e) and to two monomers (f). The energy of each step and transition state is also given.

in Fig. 7.3, all barriers are $\lesssim$0.2 eV. Experimentally, it may be possible to verify the proton scrambling predicted here with measurements on combinations of heavy and light water, possibly even on the molecular-level with STM and STM inelastic electron tunneling spectroscopy.

The results of the present study are now placed in a somewhat broader context. A surface-mediated mechanism for proton transfer has been observed for water on MgO. It involves the concerted exchange of a surface bound proton and a covalently bonded proton between water and hydroxyl. The mechanism is distinct from the most widely studied proton transfer mechanism in solution, namely the Grotthuss mechanism, in that it does not involve an excess proton nor does it proceed through an H_3O^+ intermediate. Of the traditional proton transfer mechanisms in solution, the observations here most resemble the predicted mechanism for hydroxide ion transport in liquid water [17]. This process proceeds through an "OH-H-OH"-like complex similar to the

transition structure predicted here but without the chemisorbed H. Proton transfer has been observed or predicted at a variety of water-solid interfaces before [14, 114, 157–159, 172] particularly when partially dissociated water-hydroxyl structures are involved. Indeed an analogous concerted exchange within a 2D water-hydroxyl overlayer on BaO has recently been predicted [172]. Generally, however, the surface-mediated proton transfer mechanism observed here is distinct from other simpler proton transfer events in that it involves the concerted exchange of a surface bound proton and a covalently bonded proton. It has been shown results for proton transfer in the smallest possible water cluster here. Since dimers are also constituents of larger water clusters on MgO and the full monolayer structure [163, 173–176], this suggests that the observations made here are likely to be of much broader relevance than just water dimers. Indeed together with the recent report on BaO [172] it is likely that surface-mediated proton transfer will provide a facile mechanism for proton transfer at many other interfacial water systems.

7.5 Conclusions

In conclusion, with the help of a series of static and MD simulations several aspects of proton transfer between adsorbed water molecules on MgO(001) have been elucidated. Due to the similar stabilities of isolated monomer, intact and dissociated dimer states, and to the small proton transfer barriers between them, proton transfer is predicted in clusters of just two water molecules. The key process that enables this is the concerted exchange of both a surface bound proton and a covalently bonded proton between water and hydroxyl. It is expected that this surface-mediated proton transfer will facilitate the scrambling of protons in other interfacial water systems whenever the relative energies of intact and dissociated states are similar.

Chapter 8

Summary and Perspectives

Throughout this thesis, calculations and analysis based on DFT (mainly using the PBE exchange-correlation functional) have been performed to understand the interaction of water and ice with oxide surfaces.

To begin, the interaction of water and ice with a layered aluminosilicate clay mineral kaolinite has been investigated. Specifically, an extensive series of geometric and electronic structures of water and ice on kaolinite were considered to understand how exactly water adsorbs and ice nucleates on kaolinite at the molecular level. Summarizing the energetics of the various adsorption systems examined (from water monomers, clusters to 2D overlayers and beyond), several interesting features come from these calculations: First, water monomers bind strongly to the kaolinite hydroxylated surface compared to many other substrates, in particular the well studied close-packed transition metal model systems. In the preferred adsorption structure water accepts two hydrogen bonds from and donates one hydrogen bond to the substrate, revealing that kaolinite, like water, is amphoteric with the ability to accept and donate hydrogen bonds. Second, water clustering is not favoured to any great extent. Dimers, tetramers, and hexamers are equally stable to water monomers on the kaolinite hydroxylated surface at best. This behaviour is unusual for adsorbed water and different from what is observed experimentally and predicted theoretically on other substrates, e.g. metals. Third, a stable 2D ice-like overlayer is predicted to form on the kaolinite hydroxylated

surface. This overlayer has a stability comparable to that of ice Ih, indicating that water can wet the bare perfect kaolinite surface. The stability of this ice-like overlayer is not dependent on the exchange-correlation functionals used, the inclusion of zero point energies, or the proton disorder effects in the adsorption system. Amphoterism and flexibility of the surface hydroxyl groups are considered to be key to the formation of the stable single overlayer and many other interesting properties of kaolinite with regard to water adsorption and ice nucleation. Finally, water covered kaolinite is itself "hydrophobic" compared to the bare "hydrophilic" kaolinite surface, indicating subsequent ice growth is not favoured on a single stable wetting layer. This is down to the saturation of dangling hydrogen bonds in the single water overlayer.

Following the water adsorption studies on kaolinite, the perfect basal surface of kaolinite was investigated and it (and in general the entire class of so-called 1:1 clay surfaces) is shown to be polar and unstable. Of the various mechanisms considered to stabilize the kaolinite surface, the most promising option identified so far involves the adsorption of foreign atoms on the perfect basal surface, since this yields a non-metallic surface with a cleavage energy lower than the unreconstructed polar basal surface.

Based on the studies in this thesis, the role played by kaolinite in ice forming process is shown to be more complex than previously thought. Much more work is needed, and will hopefully be prompted by this thesis, on issues such as: (i) The structure of the kaolinite basal surface (and indeed other layered 1:1 aluminosilicate clay mineral) needs to be characterized, in particular with the help of experiments; (ii) The role in ice nucleation of defective surfaces, adsorbed foreign ions, or other facets of kaolinite needs to be explored; (iii) The formation mechanism of multilayer ice on kaolinite is worth investigating continuously; and (iv) The dynamical process of the ice-water phase transformation on kaolinite, or in general on surfaces of good heterogeneous ice forming agents, should be addressed. Indeed currently I am performing metadynamics simulations on the freezing of a liquid water film on the kaolinite surface.

Extending the water adsorption studies beyond kaolinite, the interaction of water with a range of simple rocksalt (alkaline earth metal) oxide surfaces was investigated. From the calculations of water monomer adsorption on simple model oxide systems, some simple trends of basic importance to the reaction of water at surfaces have been identified. Specifically, the adsorption energy of water increases as one moves down the alkaline earth series of oxides; the tendency of water to dissociate also increases as one moves down the series; and the surface relaxation (in particular, the rumpling of the substrate) and its lattice constant have a surprisingly big impact on the properties of each substrate with regard to water adsorption and dissociation. The stability trends on oxide surfaces and the question of which state (intact or dissociated) water is in are fundamental questions. To better understand them, more common oxide surfaces should be examined, for example, the rutile oxide surfaces, the corundum oxide surfaces, and the wurtzite oxide surfaces. Such studies would help to identify other trends in water adsorption and move towards a true predictive understanding of water at surfaces.

Finally, proton transfer, as another important issue to many water-oxide interface reactions, was investigated on MgO(001). A notable result is that adsorbed water clusters of just two molecules (i.e. dimers) are sufficient to facilitate proton transfer between oxygen atoms. Facile dissociation and recombination of the molecules within the dimers along with a concerted surface-mediated exchange of protons between water and hydroxyl molecules makes this possible. It may be possible to verify this prediction experimentally and it is expected to happen on other surfaces whenever the relative energies of intact and dissociated states are similar. In general, proton transfer in interfacial water systems is poorly understood and further studies on MgO and other surfaces may lead to interesting new results. The fact that water dissociation and proton transfer is possible in the water dimer implies also the role of the water-water interaction to water adsorption and dissociation. In the future, it would be interesting to include water clusters and other extended overlayers in studies aimed at systematically identifying trends in water adsorption.

Appendix A

Tests of pseudopotentials

Here I report some of the tests performed to evaluate the accuracy of the pseudopotentials used in Chapter 4. Vanderbilt ultrasoft pseudopotentials, as generated by the built-in pseudopotential generator in the CASTEP code, were used. For users of the CASTEP code, the following strings generate the specific (PBE) pseudopotentials discussed here: "1|0.8|5|7|15|10(qc=6.4)[]" for H; "2|1.3|5|7|15|20:21(qc=7.5)[ ]" for O; "2|2.0|5|7|15|30:31:32LGG[]" for Al; and "2|1.8|5|7|15|30:31:32LGG[]" for Si. The most important information contained in these obscure strings for each element is the following: The electronic configuration for the H pseudoatom is $1s^1$. The core radius is 0.8 a.u., the angular momentum of local channel is p, and the 1s state is treated as the valence state. The electronic configuration for the O pseudoatom is $2s^2 2p^4$. The core radius is 1.3 a.u., the angular momentum of local channel is d, and the 2s and 2p states are treated as the valence states. The electronic configuration for the Al pseudoatom is $3s^2 3p^1$. The core radius is 2.0 a.u., the angular momentum of local channel is d, and the 3s, 3p and 3d states are treated as the valence states. The electronic configuration for the Si pseudoatom is $3s^2 3p^2$. The core radius is 1.8 a.u., the angular momentum of local channel is d, and the 3s, 3p and 3d states are treated as the valence states.

In order to first establish an appropriate energy cutoff for calculations on our system, test calculations for a single atom in a 10 Å cubic box were performed with Γ point $\boldsymbol{k}$ sampling of the Brillouin zone. The relative energy of each of the four pseudoatoms is

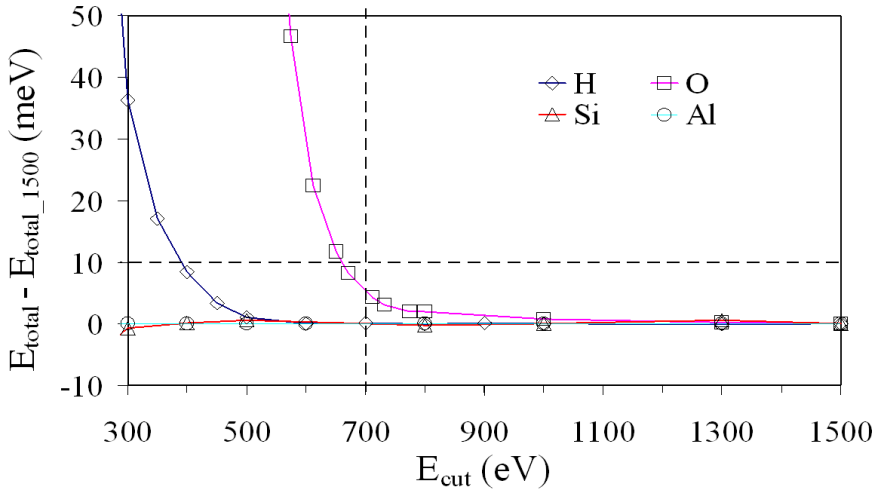

Figure A.1: Convergence of the pseudoatom total energy (E_{total}) with respect to the plane wave cutoff. All elements have been normalized to zero at a cutoff of 1500 eV (E_{total_1500}).

shown in Fig. A.1. Following these tests a plane wave cutoff of 700 eV was selected, which guarantees convergence of the total energies of all elements to within 10 meV of the total energy of each element obtained with a cutoff of 1500 eV. It is noted that of the four pseudopotentials oxygen is the hardest. A further test calculation for oxygen with a cutoff of 3000 eV revealed that the energy difference between the total energy at 700 eV and 3000 eV was still within the very tight 10 meV convergence criteria selected here.

The quality of the pseudopotentials was tested by comparing their performance at computing the atomization energies of small molecules to the results obtained from all electron calculations. The reference all electron results are taken from Ref. [177], which were performed with large basis sets of Gaussian-type orbitals. Specifically an aug-ccpVQZ basis set was used, which, for present purposes, is large enough not to suffer from significant basis set incompleteness errors. As can be seen from Table A.1, the differences between the all electron and pseudopotential results are generally small. For all non-oxygen containing molecules the pseudopotentail and all electron results agree extremely well, the differences are never more than 0.02 eV/molecule. For the

Table A.1: Comparison between pseudopotential (PS) and all electron (AE) results for the PBE electronic atomization energy of some small molecules along with the experimental values. All values are given in eV.

Molecule	This work[a]	AE[b]	Δ(AE-PS)	Exp.[b]
H_2	4.54	4.54[c]	0.00	4.47[d]
Si_2	3.53	3.53	0.00	3.21
Si_2H_6	22.58	22.57	-0.01	23.11
SiH_2 ($^1A_1$)	6.43	6.42	-0.01	6.68
SiH_2 ($^3B_1$)	5.72	5.72	0.00	5.68
SiH_3	9.66	9.65	-0.01	9.80
SiH_4	13.62	13.60	-0.02	14.05
H_2O_2	11.86	12.26	0.40	11.62
H_2O	9.96	10.17	0.21	10.10
O_2	5.91	6.24	0.33	5.12
OH	4.63	4.77	0.14	4.64
SiO	8.44	8.53	0.09	8.28

[a] This work (plane wave basis set with a cutoff energy of 700 eV).

[b] Ref. [177] (all electron with an aug-cc-pVQZ basis set).

[c] Computed in this study with the same set-up as in Ref. [177].

[d] Experimental value from Ref. [146].

Table A.2: Comparison between pseudopotential, all-electron, and experimental results for the lattice constant (a), bulk modulus (B_0) and cohesive energy (E_{coh}) of bulk aluminium and silicon.

	a(Å)	B_0(Mbar)	E_{coh}(eV/atom)
Aluminium			
This work	4.03	0.77	3.45
AE[a]	4.04	0.78	3.60
Exp.[b]	4.05	0.722	3.39
Silicon			
This work	5.46	0.89	4.57
AE[c]	5.47	0.88	4.59
Exp.[b]	5.430	0.988	4.63

[a] Ref. [178] (all electron full-potential linearized augmented plane wave calculations).

[b] Ref. [63].

[c] Ref. [179] (all electron full-potential augmented plane-wave plus local orbital calculations).

oxygen containing molecules larger differences are observed, $\leqslant$0.2 eV/oxygen. This is common for oxygen pseudopotentials and for present purposes of a tolerable absolute error [52].

The performance of the pseudopotentials was also tested on the properties of bulk aluminium and silicon, as listed in Table A.2. All the all electron and pseudopotental values are calculated using the PBE functional and again the agreement between the all electron and pseudopotential results is good.

Bibliography

[1] M. J. Gillan, D. Alfè, J. Brodholt, L. Vočadlo, and G. D. Price, Rep. Prog. Phys. **69**, 2365 (2006).

[2] J. K. Nørskov, T. Bligaard, B. Hvolbæk, F. Abild-Pedersen, I. Chorkendorff, and C. H. Christensen, Chem. Soc. Rev. **37**, 2163 (2008).

[3] J. K. Nørskov, T. Bligaard, J. Rossmeisl, and C. H. Christensen, Nature Chem. **1**, 37 (2009).

[4] P. Hohenberg and W. Kohn, Phys. Rev. **136**, B864 (1964).

[5] W. Kohn and L. J. Sham, Phys. Rev. **140**, A1133 (1965).

[6] P. A. Thiel and T. E. Madey, Surf. Sci. Rep. **7**, 211 (1987).

[7] M. A. Henderson, Surf. Sci. Rep. **46**, 1 (2002).

[8] H. R. Pruppacher and J. D. Klett, *Microphysics of Clouds and Precipitation - Second Revised and Enlarged Edition with an Introduction to Cloud Chemistry and Cloud Electricity* (Kluwer Academic Publishers, Dordrecht, 1997).

[9] C. Clay and A. Hodgson, Curr. Opin. Solid State Mater. Sci. **9**, 11 (2005).

[10] A. Michaelides, Appl. Phys. A **85**, 415 (2006).

[11] A. Hodgson and S. Haq, Surf. Sci. Rep. **64**, 381 (2009).

[12] J. Carrasco, A. Michaelides, M. Forster, S. Haq, R. Raval, and A. Hodgson, Nature Mater. **8**, 427 (2009).

[13] V. Coustet and J. Jupille, Surf. Sci. **307-309**, 1161 (1994).

[14] K. C. Hass, W. F. Schneider, A. Curioni, and W. Andreoni, Science **282**, 265 (1998).

[15] Y. Maréchal, *The Hydrogen Bond and the Water Molecule* (Elsevier, 2007).

[16] C. J. T. de Grotthuss, Ann. Chim. **LVIII**, 54 (1806).

[17] D. Marx, ChemPhysChem **7**, 1848 (2006).

[18] G. E. Brown Jr., V. E. Henrich, W. H. Casey, D. L. Clark, C. Eggleston, A. Felmy, D. W. Goodman, M. Grätzel, G. Maciel, M. I. McCarthy, et al., Chem. Rev. **99**, 77 (1999).

[19] G. E. Brown Jr., Science **294**, 67 (2001).

[20] P. Fenter and N. C. Sturchio, Prog. Surf. Sci. **77**, 171 (2004).

[21] G. E. Ewing, Chem. Rev. **106**, 1511 (2006).

[22] A. Verdaguer, G. M. Sacha, H. Bluhm, and M. Salmeron, Chem. Rev. **106**, 1478 (2006).

[23] V. E. Henrich and P. A. Cox, *The Surface Science of Metal Oxides* (Cambridge University Press, 1994).

[24] P. J. Feibelman, Phys. Today **63**, 34 (2010).

[25] M. Head-Gordon and E. Artacho, Phys. Today **61**, 58 (2008).

[26] E. K. H. Salje, E. Artacho, K. F. Austen, R. P. Bruin, M. Calleja, H. F. Chappell, G. T. Chiang, M. T. Dove, I. Frame, A. L. Goodwin, et al., Phil. Trans. R. Soc. A **367**, 967 (2009).

[27] N. H. de Leeuw, J. A. Purton, S. C. Parker, G. W. Watson, and G. Kresse, Surf. Sci. **452**, 9 (2000).

[28] N. H. de Leeuw and J. A. Purton, Phys. Rev. B **63**, 195417 (2001).

[29] N. T. Skipper, G. Sposito, and F.-R. Chang, Clays Clay Miner. **43**, 285 (1995).

[30] N. T. Skipper, F.-R. Chang, and G. Sposito, Clays Clay Miner. **43**, 294 (1995).

[31] D. Spagnoli, D. J. Cooke, S. Kerisit, and S. C. Parker, J. Mater. Chem. **16**, 1997 (2006).

[32] S. Kerisit, D. J. Cooke, D. Spagnoli, and S. C. Parker, J. Mater. Chem. **15**, 1454 (2005).

[33] N. H. de Leeuw, S. C. Parker, C. R. A. Catlow, and G. D. Price, Phys. Chem. Minerals **27**, 332 (2000).

[34] M. C. Payne, M. P. Teter, D. C. Allan, T. A. Arias, and J. D. Joannopoulos, Rev. Mod. Phys. **64**, 1045 (1992).

[35] M. D. Segall, P. J. D. Lindan, M. J. Probert, C. J. Pickard, P. J. Hasnip, S. J. Clark, and M. C. Payne, J. Phys.: Cond. Matt. **14**, 2717 (2002).

[36] S. J. Clark, M. D. Segall, C. J. Pickard, P. J. Hasnip, M. I. J. Probert, K. Refson, and M. C. Payne, Z. Kristallogr. **220**, 567 (2005).

[37] G. Kresse and J. Hafner, Phys. Rev. B **47**, 558 (1993).

[38] G. Kresse and J. Furthmüller, Phys. Rev. B **54**, 11169 (1996).

[39] R. G. Parr and W. Yang, *Density-Functional Theory of Atoms and Molecules* (Oxford University Press, New York, 1989).

[40] R. M. Martin, *Electronic Structure - Basic Theory and Practical Methods* (Cambridge University Press, UK, 2005).

[41] F. Jensen, *Introduction to Computational Chemistry, 2nd ed.* (John Wiley & Sons, England, 2007).

[42] M. Born and J. R. Oppenheimer, Ann. Physik **84**, 457 (1927).

[43] L. H. Thomas, Proc. Cambridge. Phil. Roy. Soc. **23**, 542 (1927).

[44] E. Fermi, Rend. Accad. Lincei **6**, 602 (1927).

[45] M. Gell-Mann and K. A. Brueckner, Phys. Rev. **106**, 364 (1957).

[46] D. M. Ceperley and B. J. Alder, Phys. Rev. Lett. **45**, 566 (1980).

[47] J. P. Perdew and A. Zunger, Phys. Rev. B **23**, 5048 (1981).

[48] J. P. Perdew and Y. Wang, Phys. Rev. B **45**, 13244 (1992).

[49] S. J. Vosko, L. Wilk, and M. Nusair, Can. J. Phys. **58**, 1200 (1980).

[50] J. P. Perdew, K. Burke, and M. Ernzerhof, Phys. Rev. Lett. **77**, 3865 (1996).

[51] J. P. Perdew, K. Burke, and M. Ernzerhof, Phys. Rev. Lett. **78**, 1396 (1997).

[52] B. Hammer, L. B. Hansen, and J. K. Nørskov, Phys. Rev. B. **59**, 7413 (1999).

[53] Z. Wu and R. E. Cohen, Phys. Rev. B. **73**, 235116 (2006).

[54] J. P. Perdew, J. A. Chevary, S. H. Vosko, K. A. Jackson, M. R. Pederson, D. J. Singh, and C. Fiolhais, Phys. Rev. B. **46**, 6671 (1992).

[55] O. Gunnarson and B. I. Lundqvist, Phys. Rev. B **13**, 4274 (1976).

[56] C. Adamo and V. Barone, J Chem. Phys. **110**, 6158 (1999).

[57] C. Lee, W. Yang, and R. G. Parr, Phys. Rev. B **37**, 785 (1988).

[58] A. D. Becke, J. Chem. Phys. **98**, 5648 (1993).

[59] M. Ernzerhof and G. E. Scuseria, J. Chem. Phys. **110**, 5029 (1999).

[60] J. P. Perdew and M. Ernzerhof, J. Chem. Phys. **105**, 9982 (1996).

[61] M. Dion, H. Rydberg, E. Schröder, D. C. Langreth, and B. I. Lundqvist, Phys. Rev. Lett. **92**, 246401 (2004).

[62] J. Klimeš, D. R. Bowler, and A. Michaelides, J. Phys.: Condens. Matter **22**, 022201 (2010).

[63] C. Kittel, *Introduction to Solid State Physics, 8th ed.* (John Wiley & Sons, New York, 2005).

[64] N. W. Ashcroft and N. D. Mermin, *Solid State Physics* (Thomson Learning, USA, 1976).

[65] E. Kaxiras, *Atomic and Electronic Strucuture of Solid* (Cambridge University Press, UK, 2003).

[66] H. J. Monkhorst and J. D. Pack, Phys. Rev. B **13**, 5188 (1976).

[67] D. Vanderbilt, Phys. Rev. B **41**, 7892 (1990).

[68] P. E. Blöchl, Phys. Rev. B **50**, 17953 (1994).

[69] G. Kresse and D. Joubert, Phys. Rev. B **59**, 1758 (1999).

[70] M. P. Allen and D. J. Tildesley, *Computer Simulation of Liquids* (Oxford University Press, New York, 1987).

[71] D. Frenkel and B. Smit, *Understanding Molecular Simulation - From Algorithms to Applications, 2nd ed.* (Academic Press, USA, 2002).

[72] D. Marx and J. Hutter, *Ab Initio Molecular Dynamics - Basic Theory and Advanced Methods* (Cambridge University Press, Cambridge, 2009).

[73] G. J. Martyna, M. L. Klein, and M. Tuckerman, J. Chem. Phys. **97**, 2635 (1992).

[74] G. Ketteler, S. Yamamoto, H. Bluhm, K. Andersson, D. E. S. amd D. F. Ogletree, H. Ogasawara, A. Nilsson, and M. Salmeron, J. Phys. Chem. C **111**, 8278 (2007).

[75] M. Odelius, M. Bernasconi, and M. Parrinello, Phys. Rev. Lett. **78**, 2855 (1997).

[76] P. B. Miranda, L. Xu, Y. R. Shen, and M. Salmeron, Phys. Rev. Lett. **81**, 5876 (1998).

[77] S.-H. Park and G. Sposito, Phy. Rev. Lett. **89**, 85501 (2002).

[78] J. M. Adams, Clays Clay Miner. **31**, 352 (1983).

[79] R. A. Young and A. W. Hewat, Clays Clay Miner. **36**, 225 (1988).

[80] D. L. Bish and R. B. V. Dreele, Clays Clay Miner. **37**, 289 (1989).

[81] D. L. Bish, Clays Clay Miner. **41**, 738 (1993).

[82] R. B. Neder, M. Burghammer, T. Grasl, H. Schulz, A. Bram, and S. Fiedler, Clays Clay Miner. **47**, 487 (1999).

[83] D. Tunega, M. H. Gerzabek, and H. Lischka, J. Phys. Chem. B **108**, 5930 (2004).

[84] M. R. Warne, N. L. Allan, and T. Cosgrove, Phys. Chem. Chem. Phys. **2**, 3663 (2000).

[85] L. Benco, D. Tunega, J. Hafner, and H. Lischka, J. Phys. Chem. B **105**, 10812 (2001).

[86] E. Balan, A. M. Saitta, F. Mauri, and G. Calas, Am. Mineral. **86**, 1321 (2001).

[87] D. Tunega, L. Benco, G. Haberhauer, M. H. Gerzabek, and H. Lischka, J. Phys. Chem. B **106**, 11515 (2002).

[88] J. Ireta, J. Neugebauer, and M. Scheffler, J. Phys. Chem. A **108**, 5692 (2004).

[89] B. Santra, A. Michaelides, and M. Scheffler, J. Chem. Phys. **127**, 184104 (2007).

[90] D. R. Hamann, Phys. Rev. B **55**, R10157 (1997).

[91] P. J. Feibelman, Science **295**, 99 (2002).

[92] V. F. Petrenko and R. W. Whitworth, *Physics of Ice* (Oxford University Press, Oxford, 1999).

[93] H. Sato, K. Ono, C. T. Johnston, and A. Yamagishi, Am. Mineral. **89**, 1581 (2004).

[94] S. Tosoni, K. Doll, and P. Ugliengo, Chem. Mater. **18**, 2135 (2006).

[95] M. Zbik and R. S. C. Smart, Miner. Eng. **15**, 277 (2002).

[96] J. Kameda, A. Yamagishi, and T. Kogure, Am. Mineral. **90**, 1462 (2005).

[97] W. D. Nesse, *Introduction to Mineralogy* (Oxford University Press, New York, 1999).

[98] A. Michaelides, Faraday Discuss. **136**, 287 (2007).

[99] J. Yang, S. Meng, L. Xu, and E. G. Wang, Phys. Rev. B **71**, 35413 (2005).

[100] J. M. Park, J.-H. Cho, and K. S. Kim, Phys. Rev. B **69**, 233403 (2004).

[101] Y. Yang, S. Meng, and E. G. Wang, Phys. Rev. B **74**, 245409 (2006).

[102] S. Meng, E. G. Wang, and S. Gao, Phys. Rev. B **69**, 195404 (2004).

[103] T. Mitsui, M. K. Rose, E. Fomin, D. F. Ogletree, and M. Salmeron, Science **297**, 1850 (2002).

[104] V. A. Ranea, A. Michaelides, R. Ramírez, P. L. de Andres, J. A. Vergés, and D. A. King, Phys. Rev. Lett. **92**, 136104 (2004).

[105] K. Morgenstern and K. H. Rieder, J. Chem. Phys. **116**, 5476 (2002).

[106] K. Morgenstern and J. Nieminen, Phys. Rev. Lett. **88**, 066102 (2002).

[107] A. Michaelides and K. Morgenstern, Nature Mater. **6**, 597 (2007).

[108] J. Cerdá, A. Michaelides, M. L. Bocquet, P. J. Feibelman, T. Mitsui, M. Rose, E. Fomin, and M. Salmeron, Phys. Rev. Lett. **93**, 116101 (2004).

[109] S. Haq, C. Clay, G. R. Darling, G. Zimbitas, and A. Hodgson, Phys. Rev. B **73**, 115414 (2006).

[110] M. Morgenstern, T. Michely, and G. Comsa, Phys. Rev. Lett. **77**, 703 (1996).

[111] M. Morgenstern, J. Mueller, T. Michely, and G. Comsa, Z. Phys. Chem. (Munich) **198**, 43 (1997).

[112] H. Ogasawara, B. Brena, D. Nordlund, M. Nyberg, A. Pelmenschikov, L. G. M. Pettersson, and A. Nilsson, Phys. Rev. Lett. **89**, 276102 (2002).

[113] A. Michaelides and P. Hu, J. Chem. Phys. **114**, 513 (2001).

[114] A. Michaelides and P. Hu, J. Am. Chem. Soc. **123**, 4235 (2001).

[115] A. Nilsson, H. Ogasawara, M. Cavalleri, D. Nordlund, M. Nyberg, P. Wernet, and L. G. M. Pettersson, J. Chem. Phys. **122**, 154505 (2005).

[116] A. Michaelides, A. Alavi, and D. A. King, Phys. Rev. B. **69**, 113404 (2004).

[117] A. Michaelides, V. A. Ranea, P. L. de Andres, and D. A. King, Phys. Rev. B **69**, 75409 (2004).

[118] V. A. Ranea, A. Michaelides, R. Ramírez, J. A. Vergés, P. L. de Andres, and D. A. King, Phys. Rev. B **69**, 205411 (2004).

[119] C. J. Zhang and P. J. D. Lindan, J. Chem. Phys. **118**, 4620 (2003).

[120] P. J. D. Lindan and C. J. Zhang, Phys. Rev. B **72**, 075439 (2005).

[121] S. Wendt, R. Schaub, J. Matthiesen, E. K. Vestergaard, E. Wahlström, M. D. Rasmussen, P. Thostrup, L. M. Molina, E. Lægsgaard, I. Stensgaard, et al., Surf. Sci. **598**, 226 (2005).

[122] J. Yang and E. G. Wang, Phys. Rev. B **73**, 035406 (2006).

[123] D. Sebastiani and L. D. Site, J. Chem. Theory Comput. **1**, 78 (2005).

[124] G. A. Kimmel, N. G. Petrik, Z. Dohnálek, and B. D. Kay, Phys. Rev. Lett. **95**, 166102 (2005).

[125] G. Zimbitas, M. E. Gallagher, G. R. Darling, and A. Hodgson, J. Chem. Phys. **128**, 074701 (2008).

[126] X. L. Hu and A. Michaelides, Surf. Sci. **601**, 5378 (2007).

[127] X. L. Hu and A. Michaelides, Surf. Sci. **602**, 960 (2008).

[128] I. F. Vasconcelos, B. A. Bunker, and R. T. Cygan, J. Phys. Chem. C **111**, 6753 (2007).

[129] A. Kremleva, S. Krüger, and N. Rösch, Langmuir **24**, 9515 (2008).

[130] T. Croteau, A. K. Bertram, and G. N. Patey, J. Phys. Chem. A **112**, 10708 (2008).

[131] G. Kresse, W. Bergermayer, R. Podloucky, E. Lundgren, R. Koller, M. Schmid, and P. Varga, Appl. Phys. A **76**, 701 (2003).

[132] O. Dulub, U. Diebold, and G. Kresse, Phys. Rev. Lett. **90**, 016102 (2003).

[133] M. M. Islam, B. Diawara, V. Maurice, and P. Marcus, Surf. Sci. **603**, 2087 (2009).

[134] J. Neugebauer and M. Scheffler, Phys. Rev. B **46**, 16067 (1992).

[135] G. Makov and M. C. Payne, Phys. Rev. B **51**, 4014 (1995).

[136] D. Pan, L. M. Liu, G. A. Tribello, B. Slater, A. Michaelides, and E. G. Wang, Phys. Rev. Lett. **101**, 155703 (2008).

[137] P. W. Tasker, J. Phys. C: Solid State Phys. **12**, 4977 (1979).

[138] A. Wander, F. Schedin, P. Steadman, A. Norris, R. McGrath, T. S. Turner, G. Thornton, and N. M. Harrison, Phys. Rev. Lett. **86**, 3811 (2001).

[139] C. Noguera, J. Phys.: Condens. Matter. **12**, R367 (2000).

[140] J. Goniakowski, C. Noguera, and L. Giordano, Phys. Rev. Lett. **98**, 205701 (2007).

[141] J. Goniakowski, F. Finocchi, and C. Noguera, Rep. Prog. Phys. **71**, 016501 (2008).

[142] B. Meyer and D. Marx, Phys. Rev. B **67**, 035403 (2003).

[143] G. Kresse, O. Dulub, and U. Diebold, Phys. Rev. B **68**, 245409 (2003).

[144] E. Joussein, S. Petit, J. Churchman, B. Theng, D. Righi, and B. Delvaux, Clay Miner. **40**, 383 (2005).

[145] C. Ma and R. A. Eggleton, Clays Clay Miner. **47**, 181 (1999).

[146] *CRC Handbook of Chemistry and Physics, 88th ed.* (CRC, Boca Raton, FL, 2007-2008).

[147] J.-H. Lee and S. Guggenheim, Am. Mineral. **66**, 350 (1981).

[148] G. Henkelman, A. Arnaldsson, and H. Jónsson, Comput. Mater. Sci. **36**, 254 (2006).

[149] O. Bikondoa, C. L. Pang, R. Ithnin, C. A. Muryn, H. Onishi, and G. Bikondoa, Nature Mater. **5**, 189 (2006).

[150] A. Michaelides, A. Alavi, and D. A. King, J. Am. Chem. Soc. **125**, 2746 (2003).

[151] K. Andersson, G. ketteler, H. Bluhm, S. Yamamoto, H. Ogasawara, L. Pettersson, M. Salmeron, and A. Nilsson, J. Am. Chem. Soc. **130**, 2793 (2008).

[152] C. Noguera, *Physics and Chemistry at Oxide Surfaces* (Cambridge University Press, 1996).

[153] P. Broqvist, H. Grönbeck, and I. Panas, Surf. Sci. **554**, 262 (2004).

[154] N. V. Skorodumova, K. Hermansson, and B. Johansson, Phys. Rev. B. **72**, 125414 (2005).

[155] J. Carrasco, F. Illas, and N. Lopez, Phys. Rev. Lett. **100**, 016101 (2008).

[156] R. Hoffmann, Rev. Mod. Phys. **60**, 601 (1988).

[157] M. Nagasaka, H. Kondoh, K. Amemiya, T. Ohta, and Y. Iwasawa, Phys. Rev. Lett. **100**, 106101 (2008).

[158] G. Cicero, A. Catellani, and G. Galli, Phys. Rev. Lett. **93**, 016102 (2004).

[159] G. Cicero, A. Catellani, and G. Galli, J. Phys. Chem. **108**, 16518 (2004).

[160] J.-H. Cho, J. M. Park, and K. S. Kim, Phys Rev. B **62**, 9981 (2000).

[161] D. Alfè and M. J. Gillan, J. Chem. Phys. **127**, 114709 (2007).

[162] W. Langel and M. Parrinello, J. Chem. Phys. **103**, 3240 (1995).

[163] M. Odelius, Phys. Rev. Lett. **82**, 3919 (1999).

[164] Y. Wang and T. N. Truong, J. Phys. Chem. B **108**, 3289 (2004).

[165] J. VandeVondele and M. Sprik, Phys. Chem. Chem. Phys. **7**, 1363 (2005).

[166] J. Baker, J. Andzelm, M. Muir, and P. R. Taylor, Chem. Phys. Lett. **237**, 53 (1995).

[167] Y. Zhao, B. J. Lynch, and D. G. Truhlar, J. Phys. Chem. A **108**, 2715 (2004).

[168] M. J. Stirniman, C. Huang, R. S. Smith, S. A. Joyce, and B. D. Kay, J. Chem. Phys. **105**, 1295 (1996).

[169] M. A. Johnson, E. V. Stefanovich, T. N. Truong, J. Günster, and D. W. Goodman, J. Phys. Chem. B **103**, 3391 (1999).

[170] O. Dulub, B. Meyer, and U. Diebold, Phys. Rev. Lett. **95**, 136101 (2005).

[171] G. Henkelman, B. P. Uberuaga, and H. Jónsson, J. Chem. Phys. **113**, 9901 (2000).

[172] H. Grönbeck and I. Panas, Phys. Rev. B **77**, 245419 (2008).

[173] L. Giordano, J. Goniakowski, and J. Suzanne, Phys. Rev. Lett. **81**, 1271 (1998).

[174] L. Giordano, J. Goniakowski, and J. Suzanne, Phys. Rev. B **62**, 15406 (2000).

[175] L. Delle Site, A. Alavi, and R. M. Lynden-Bell, J. Chem. Phys. **113**, 3344 (2000).

[176] R. M. Lynden-Bell, L. Delle Site, and A. Alavi, Surf. Sci. **496**, L1 (2002).

[177] J. Paier, R. Hirschl, M. Marsman, and G. Kresse, J. Chem. Phys. **122**, 234102 (2005).

[178] J. L. F. Da Silva, C. Stampfl, and M. Scheffler, Surf. Sci. **600**, 703 (2006).

[179] M. Hortamani, PhD thesis, theory of adsorption, diffusion and spin-polarization of Mn on Si(001) and Si(111) substrates, FU Berlin (2006).

Acknowledgements

Here I would like to thank all the people who have helped and supported me during my PhD study and thesis-writing period. Without them it would be impossible to finish this thesis at all. Specifically, in the first place I would like to thank Prof. Angelos Michaelides, my principle supervisor, for kindly offering me the opportunity to learn and study in an excellent environment of his group in UCL, for patiently teaching me the way science really works, and for continuously supporting me to attend scientific conferences and contacting with other outstanding scientists in the relevant field. I would also like to thank Prof. Neal Skipper, my subsidiary supervisor, for his discussion and help.

In addition, special thanks will be given to the ICE group of Prof. Angelos Michaelides in UCL and Berlin, which include Dr. Javier Carrasco, Dr. Anna Kimmel, Dr. Xinzheng Li, Dr. Limin Liu, Dr. Brent Walker, Dr. Changjun Zhang, Erlend Davidson, Jiří Klimeš, Biswajit Santra, Jie Ma, Ding Pan, Dr. Bo Li, and Dr. Sami Amira. Their fruitful discussion and great help are important and essential to me and make my life much easier.

Finally, I would like to give my sincerest thanks to my parents for their endless and unmatched support.

Publications

Most of the work reported in this thesis is reprinted in the following publications:

1. Ice formation on kaolinite: Lattice match or amphoterism?, **X. L. Hu** and A. Michaelides, Surf. Sci. 601, 5378 (2007).

2. Water on the hydroxylated (001) surface of kaolinite: From monomer adsorption to a flat 2D wetting layer, **X. L. Hu** and A. Michaelides, Surf. Sci. 602, 960 (2008).

3. The kaolinite (001) polar basal plane, **X. L. Hu** and A. Michaelides, Surf. Sci. 604, 111 (2010).

4. Proton transfer in adsorbed water dimers, **X. L. Hu**, J. Klimeš, and A. Michaelides, Phys. Chem. Chem. Phys., accepted.

During my studies I also contributed to:

5. Experimental and theoretical study of oxygen adsorption structures on Ag(111), J. Schnadt, J. Knudsen, **X. L. Hu**, A. Michaelides, R. T. Vang, K. Reuter, Z. Li, E. Lægsgaard, M. Scheffler, and F. Besenbacher, Phys. Rev. B 80, 075424 (2009).